INVESTIGATION OF BLOOD FLOW PATTERNS AND HEMODYNAMICS IN THE HUMAN ASCENDING AORTA AND MAJOR TRUNKS OF RIGHT AND LEFT CORONARY ARTERIES USING MAGNETIC RESONANCE IMAGING AND COMPUTATIONAL FLUID DYNAMICS

A Dissertation
Presented to
The Academic Faculty

by

Jin Suo

In Partial Fulfillment
Of the Requirements for the Degree
Doctor of Philosophy in Bioengineering

Georgia Institute of Technology
January 2005

INVESTIGATION OF BLOOD FLOW PATTERNS AND HEMODYNAMICS IN THE HUMAN ASCENDING AORTA AND MAJOR TRUNKS OF RIGHT AND LEFT CORONARY ARTERIES USING MAGNETIC RESONANCE IMAGING AND COMPUTATIONAL FLUID DYNAMICS

Approved by:

Don P. Giddens, Ph.D., Chairman
College of Engineering
Georgia Institute of Technology

John Oshinski, Ph.D.
School of Biomedical Engineering
Georgia Institute of Technology / Emory University

Raymond P. Vito, Ph.D.
College of Engineering
Georgia Institute of Technology

Gang Bao, Ph.D.
School of Biomedical Engineering
Georgia Institute of Technology / Emory University

W. Robert Taylor, Ph.D., M.D.
Department of Medicine / Division of Cardiology
Emory University

Date Approved: January 2005

This work is dedicated to my father and mother,

Guodong Suo

and

Binglan Wang

ACKNOWLEDGMENTS

I would like to express my most sincere gratitude to Dr. Don P. Giddens, the supporter and advisor throughout my career at Tech, for his foresight, erudite and patient in my research works because the major ideas of the research have been discussing results with him over long period of times, and finally he updated all the words of the thesis.

I would like to acknowledge the fruitful support and advice of Dr. John Oshinski for providing all the MRI measurements that were the fundamental materials for the research.

I am grateful to Dr. W. Robert Taylor for offering me the chance to attend the NIH project that ensured the completion of this research.

In addition, I thank Dr. Ramond P. Vito for all his help and advice in my study and works.

Last, I must say thanks to all the members of Dr. Giddens group for promotion and friendship.

TABLE OF CONTENTS

LIST OF FIGURES

LIST OF ABBREVIATIONS

BH_FL	Breath-Hold Segmented FLASH
BH_SP	Breath-Hold Interleaved Spiral
C	Celiac
CFD	Computational Fluid Dynamics
CT	Computer Tomography
CVD	Cardiovascular Disease
ECG	Electrocardiogram
ECs	Endothelial Cells
FB_FL	Free-Breathing FLASH
FB_SP	Free-Breathing Interleaved Spiral
IVUS	Intravascular Ultrasound
LAD	Left Anterior Descending Coronary Artery
LCX	Left Circumflex Coronary Artery
LR	Left Renal
MRI	Magnetic Resonance Imaging
NURBS	Non-Uniform Rational B-Spline
PC-MRI	Phase Contrast MRI
RCA	Right Coronary Artery
RR	Right Renal
SM	Superior Mesenteric
WSS	Wall Shear Stress

SUMMARY

Hemodynamic factors play a role in atherogenesis and the localization of atherosclerotic plaques. The human aorta and coronary arteries are susceptible to arterial disease, and there have been many studies of flows in models of these vessels. However, previous work has been limited in that investigations have not modeled both the geometry and flow conditions in specific individuals.

In the first aim, a methodology that combines magnetic resonance imaging (MRI) and computational fluid dynamics (CFD) was developed for investigating hemodynamics in the human ascending aorta and proximal segments of the coronary arteries. The methodology includes image processing that utilizes geometrical information from MRI slices and boundary velocity data from phase contrast (PC)-MRI to develop aorta/coronary artery models. These models are then used to compute flow fields for specific individuals, and the results are validated against PC-MRI data obtained *in vivo*. The CFD simulations successfully reproduce an unusual right-hand helical flow pattern that has been reported in the ascending aorta, giving confidence in the accuracy of the methodology.

The second aim was to investigate the causes of the right-hand helical flow. Velocity patterns among the simulation results were compared in three models: (i) a model that incorporated expansion and contraction of the lumen (compliance effects) and overall motion of the ascending aorta that results from its attachment to the beating heart; (ii) a model that allowed motion only due to compliance effects; and (iii) a completely rigid model with no motion. It was found that the correct flow dynamics could only be

produced by including the motion caused by the beating heart; and it is concluded that this is a significant factor in producing the observed *in vivo* helical flow patterns.

The entrance flows of coronary arteries are expected to be affected by flow in the aortic root, and the third aim was to explore these effects using models that include both aorta and coronary arteries. The simulation results demonstrate that a pair of axial vortexes with different rotating directions exists in the entrance segments of the right and left coronary arteries during systole and early diastole, producing asymmetrical wall shear stress (WSS) distributions.

The last aim was to explore possible relationships between hemodynamic factors and favored sites of atherosclerosis in human coronary arteries. A direct comparison of plaque distribution with computed flow fields was not possible, due to limitations in human subject availability, so comparisons relied on data obtained from the literature. In the CFD modeling, the entrance flow patterns of the right coronary artery show that the myocardial side experiences low and oscillating WSS. This site coincides with a high frequency region of atherosclerosis observed in autopsies. On the other hand, high WSS might suggest low probability of atherosclerosis. Computations showed that the middle segment of the left main coronary artery (LM) experiences higher WSS than the orifice and main bifurcation regions during the entire cardiac cycle. This region coincides with observations of a "natural resistance" to atherosclerosis exhibited distal to the first centimeter from the orifice of the left coronary artery.

The tools developed in this study provide a promising avenue for future research in the study of cardiovascular disease because of the ability to investigate phenomena in individual human subjects.

CHAPTER 1

INTRODUCTION

1.1 Atherosclerosis

Cardiovascular disease (CVD) is the leading killer among all racial and ethnic groups (Centers for Disease Control and Prevention, 1999). CVD includes dysfunctional conditions of the arteries that supply oxygenated blood to vital life-sustaining areas of the body such as the heart, brain and other organs. Atherosclerosis is the most common manifestation of arterial disease and is characterized by deposits of yellowish plaques containing cholesterol, lipoid material, and lipophages formed within the intima and inner media of arteries. Atherosclerosis begins with the accumulation of low-density lipoprotein under the endothelial layer and the contribution of neutrophils and smooth muscle cells. As the lesion progresses, these cells become filled with lipids, a raised area of intima appears, and a thick, fibrous plaque is gradually formed. Over time, these plaques may narrow the arterial lumen and obstruct the blood flow. Often, a plaque will rupture suddenly, creating an acute obstruction to blood flow. Ischemic heart disease, the most fatal form of CVD, results from obstruction of blood flow to the heart and is usually caused by atherosclerotic plaques in the coronary arteries.

Although atherosclerosis is one of the leading causes of death, the pathogenesis has been unclear until lately because of two characteristics:

- Atherosclerosis develops inside the walls of vessels so that the genesis is difficult to observe and test directly *in vivo*.

- The evolution of atherosclerosis is very slow; disease progression may span decades, which makes experiments to reproduce and study its pathogenesis very difficult.

Because of these characteristics, most information about the disease has come from clinical observations and autopsies that indicated the high frequency localizations of the lesions in the vascular system, the categorization of the lesions and the relative importance of various risk factors.

Many clinical data have been published over recent decades (e.g., DeBakey et al., 1985; PDAY Research Group, 1993; Fox and Seed, 1981; Fox et al., 1982; Svindland, 1983; Crottum et al., 1983; Velican, C. and Velican, D., 1984; Stary, 1987; Cornhill et al., 1990; Ojha et al., 2001). Using clinical records from 13,827 patients, DeBakey et al. (1985) classified atherosclerosis into five major categories, according to vascular regions: (I) the coronary arterial bed, (II) the major branches of the aortic arch, (III) the visceral arterial branches of the abdominal aorta, (IV) the terminal abdominal aorta and its major branches, and (V) a combination of two of these categories occurring simultaneously (Figure 1.1). This classification is characterized by the anatomical locations of the disease, however the investigators have described the pathological features of the atheromas among these categories.

The localization data of atherosclerosis, as Figure 1.1 shows, imply that the distribution of lesions in the vascular system is not random, but rather may be influenced by biomechanical factors: atherosclerotic lesions tend to be in the proximal section of arteries, that is, the entrance of a branch or the bifurcation of two branches (see Figure 1.1). At these locations, blood flow patterns are more complex than in straight vessel

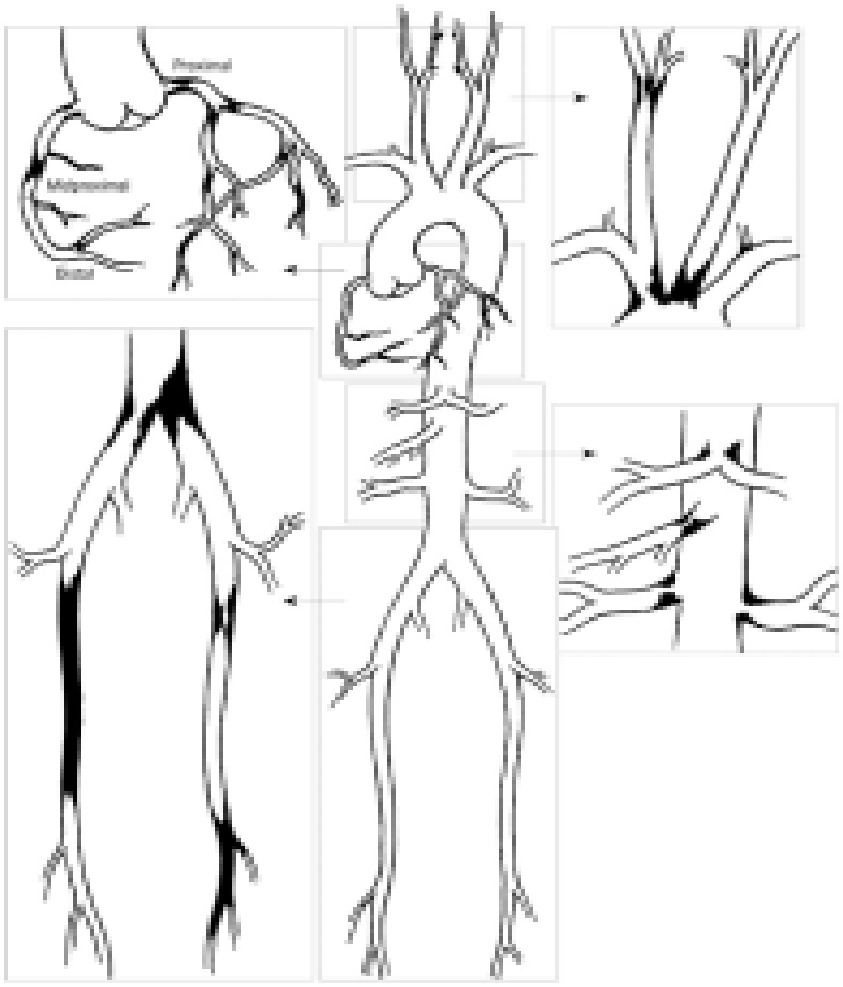

Figure 1.1: Diagram showing the predominant anatomic sites and distribution of atherosclerotic occlusive disease in the four major arterial beds of the body (Copy from Michael E. D. et al., Annals of Surgery, 201:116, 1985).

segments, and these complex patterns have been referred to as regions of "disturbed" flow.

Figure 1.2 shows another convincing clinical example (Cornhill, et al., 1990) of plaque localization. The figure presents the probability contours of atherosclerosis occurring in the human thoracic aorta based on autopsy material from 109 male subjects. It can be seen that there is a much higher probability of lesions occurring near vessel branches, such as the intercostal vessels of the thoracic aorta and the major arterial branches in the abdominal aorta. It is known that the velocity field becomes highly variable and complex in these regions.

These clinical observations have naturally led to the widespread view that hemodynamic factors play an important role in the localization of atherosclerosis (e.g. Fung, 1997; Kjaernes et al., 1981; Fox and Seed, 1981; Giddens et al., 1983).

1.2 Hemodynamics

Hemodynamic factors that have been suggested to be important in atherogenesis are derived from the velocity field and involve several different forms, such as flow separation and vortex formation, shear stresses, and spatial and temporal shear stress gradients. Between the blood flow and vessel wall there is a monolayer of cells called endothelial cells (ECs). Any interactions enhanced by hemodynamic factors seem to interplay on the ECs first, and then these actions induce unfavorable cell responses that contribute to atherogenesis and its progression. The injury hypothesis, which suggests that ECs may be injured or become dysfunctional as a result of hemodynamic factors, is widely accepted as the pathogenesis of atherosclerosis (Bierman, 1994). Local

(I)

(II)

(III)

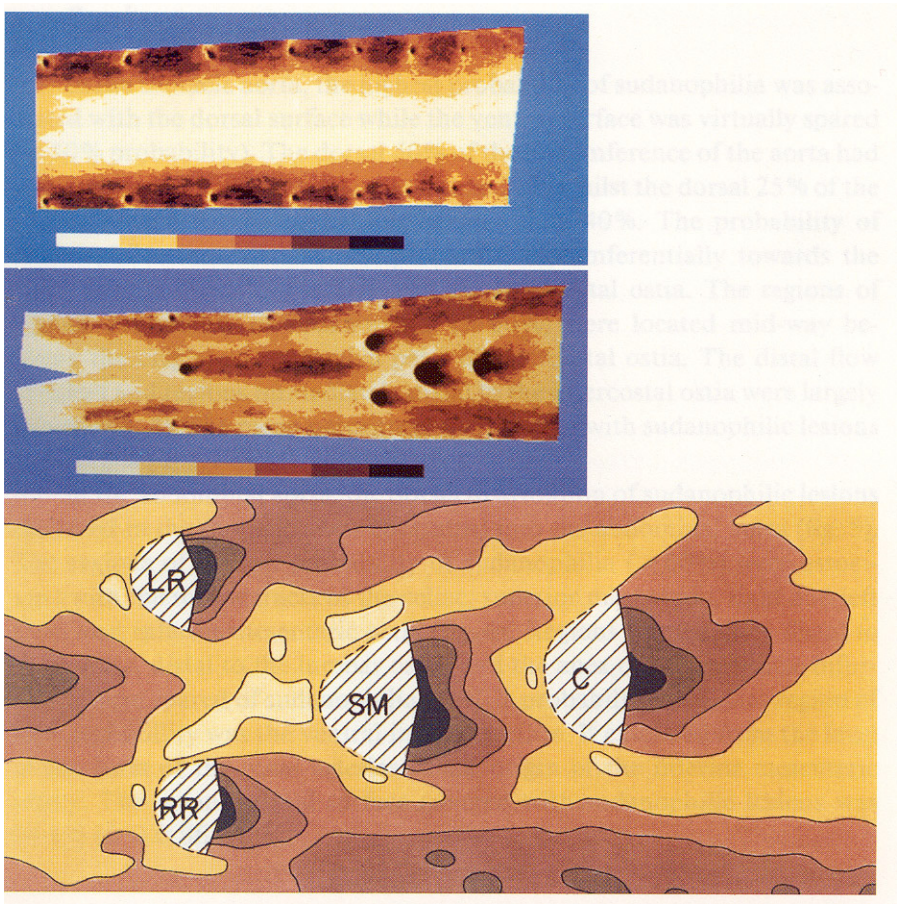

Figure 1.2: Probability-of-occurrence map of sudanophilia in the human arteries.

(I): Probability-of-occurrence map of sudanophilia in the human thoracic aorta. The map is displayed in banded incidence isopleths (white-yellow: 0-10%; yellow: 10-20%; orange: 20-30%; red-brown: 30-40%; brown: 40-50%; black: 50-60%).

(II): Probability-of-occurrence map of sudanophilia in the abdominal aorta. The banded incidence isopleths are same as in (I).

(III): A magnified smooth contour map of the region the celiac (C), superior mesenteric (SM), right renal (RR), and left renal (LR) ostia.

(From Cornhill, et al., Monogr Atheroscler, 15:17, 1990)

inflammation of the vessel wall is commonly observed (Lind, 2003), which further strengthens the injury hypothesis.

Much attention has been given to the fluid dynamic wall shear stresses (WSS) which induce a micro environment of interaction between blood and endothelial layer. WSS is a vector whose magnitude is proportional to the blood viscosity and flow velocity gradient normal to the surface, and which acts in a direction parallel to the local velocity at the wall. WSS is difficult to measure directly *in vivo* or *in vitro* so that it is generally computed from the local velocity distribution near the wall. Therefore, investigation of WSS effects requires knowledge of the local velocity field.

1.3 Computational Fluid Dynamics

Experimental methods and computational methods, the greatly successful research tools in fluid dynamics, are also available in hemodynamics research (Fung, 1997). Computational fluid dynamics (CFD) has been proven to be a reliable technique for studying time-varying, 3-D flow patterns in a complex geometrical model. In contrast to experimental flow studies, CFD is more convenient for altering model parameters such as inlet velocity, wall conditions, etc. CFD can present results with very high resolution if the boundary condition information is correct; therefore, the geometrical data and boundary velocity data that come from *in vivo* measurements are necessary for realistic modeling of blood flow in the artery. Medical imaging techniques can supply these data. From CFD solutions, it is straightforward to present velocity distributions for blood flows and to extract WSS and other important hemodynamic factors. These make CFD a unique and attractive tool for hemodynamics research.

1.4 Clinical Imaging

Since atherosclerosis occurs inside the vessel wall, various clinical imaging methods are essential tools to observe atherosclerotic plaques *in vivo*. Magnetic resonance imaging (MRI), as a relative new comer among clinical imaging methods, presents distinctive advantages. MRI has been the best clinical imaging method for distinguishing soft tissues until now. MRI not only presents geometrical images of large arteries but also contributes velocity distributions of blood flow on sections of the arteries. The non-invasive nature of MRI makes it convenient to be used in patients and normal volunteers, which may help investigators explore the pathogenesis of atherosclerosis by comparing images of lesions with those of the normal vessel wall and distinguishing factors that lead to differences (Fayad et al., 2001). A deficiency of MRI is that its spatial resolution is limited. Computerized tomography (CT) presently has better spatial resolution, but it cannot provide velocity information needed for CFD.

1.5 Research Objectives

Atherosclerotic plaques frequently develop in entrance regions and bifurcations of coronary arteries (Figure 1.1). These are locations where the blood flow patterns are influenced by pulsatile flow in the aortic root and by the complex geometry of the vessels. Despite the fact that a few decades have passed since hemodynamic hypotheses of atherosclerosis were postulated (e.g. Caro et al., 1971; Fry, 1968), quantitative descriptions of *in vivo* blood flow patterns in the human ascending aorta and coronary arteries remain unclear (e.g. Bao et al., 1999; Hyun et al., 2000; Ku et al., 1985), nor have

there been definitive causative links established between hemodynamics variables and disease mechanisms.

Given current limitations in knowledge, the overall objectives of this study are:

- To reproduce blood flow patterns in the ascending aorta and in the major segments of coronary arteries using a methodology that combines CFD and MRI; and
- To test hypothesized relationships between hemodynamic factors and the distribution of atherosclerosis reported in clinical literature.

The study will validate the CFD results using blood velocity data measured *in vivo* and will compare the computed flow patterns and WSS results with clinical observations of flow patterns and autopsy reports of plaque localization. The overall objectives will be addressed through four specific aims.

1.5.1 Specific Aim 1: To Develop and Validate a Combined CFD and MRI Methodology for Determining Blood Flow Patterns in the Human Ascending Aorta

Achieving this aim requires developing methods for applying image processing to MRI – derived images to set up the geometrical model of the healthy human aorta *in vivo*, including the aortic root, ascending and partial descending aorta, for CFD simulation (see Figure 1.3). Computing the flow field in the model requires obtaining *in vivo* velocity boundary conditions from phase contrast (PC) MRI scanning in the same subject. It is important to validate the flow patterns of the modeling using data measured *in vivo*. If the CFD results can be validated by the measured data, the methodology will be reliable for achieving overall objectives.

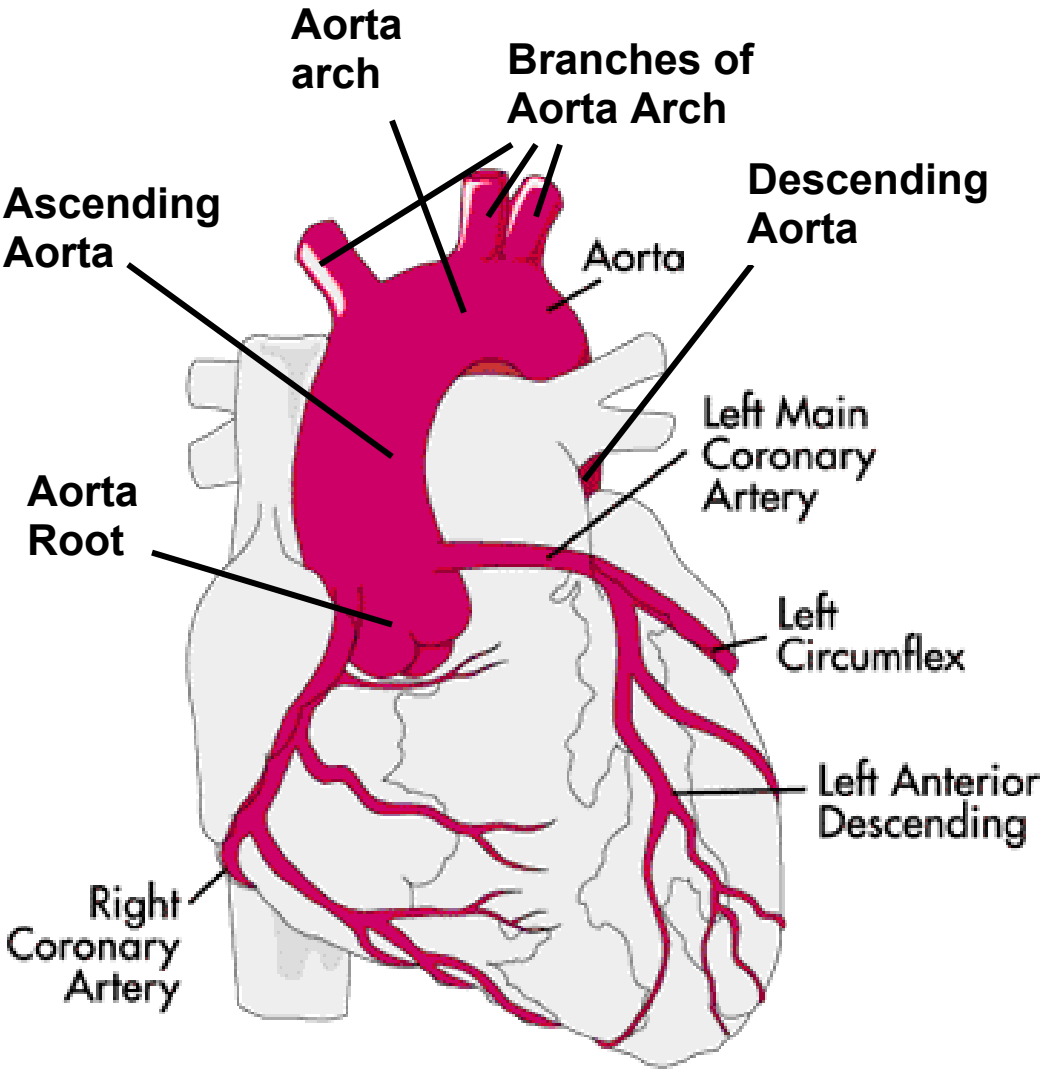

Figure 1.3: The structure of human heart, aorta and coronary arteries.

Thus, a crucial challenge for CFD is how to validate the CFD results using data measured *in vivo*. The traditional validation method in fluid dynamics research has been to compare the CFD results with the experimental results that come from physical models, such as up-scaled *in vitro* models, or with measured data *in vivo*. However, PC-MRI scanning provides *in vivo* blood velocities. The PC-MRI data can be used as boundary conditions for the CFD simulation and can also be used for validation, depending on the locations of the measured or scanned sections. In this specific aim, a transverse section located within the flow domain, midway in the ascending aorta, is selected to be the validation section where the flow velocity distribution measured by PC-MRI will be compared with the CFD results.

1.5.2 Specific Aim 2: To Reproduce Helical Flow Patterns Observed in the Human Aorta and Explore Its Causes Using the Methodology Developed in Specific Aim 1.

The aorta is arguably the "parent" artery in the cardiovascular system because all blood goes through it. The coronary arteries branch directly from the ascending aorta, from which they receive their blood supply. Blood flow patterns in the ascending aorta are pulsatile, three-dimensional and asymmetrical. Many clinical investigators have observed helical flow patterns in the human ascending aorta using medical imaging methods (e.g. Stein et al., 1979; Klipstein et al., 1987; Segadal and Matre, 1987; Frazin et al., 1990; Kilner et al., 1993; Bogren and Buonocore, 1999), but a quantitative description of the flow patterns has not been available because of resolution limitations of present clinical imaging methods *in vivo*.

This specific aim will investigate the causes of helical blood flow patterns in the ascending aorta. The CFD and MRI methodology can provide detailed descriptions of the flow patterns in the model of the ascending aorta, and the modeling is sufficiently flexible to explore various assumptions imposed on the modeling. Each assumption, which is dominated by specific factors that can affect the flow patterns, will be modeled individually. These assumptions may produces slight difference in results that can be evaluated using *in vivo* observations and measurements. The best result will show the factor or factors that are the causes of the helical blood flow patterns in the ascending aorta.

In addition to the tortuous geometrical structure of the aorta and the complex, pulsatile 3D inlet velocity patterns, the compliance of the aortic wall and the oscillatory movement of the vessel due to its attachment to the beating heart are two potentially significant factors in modeling the aorta. To simulate wall compliance and vessel motion in the CFD modeling is an essential step in conducting this study.

1.5.3 Specific Aim 3: To Determine Blood Flow Patterns in the Major Segments of the Coronary Arteries

Coronary arteries are among the most vital vessels in the cardiovascular system, since they are the blood supply for the heart (see Figure 1.3), and atherosclerosis in these arteries is the major source of myocardial infarction through plaque rupture and/or occlusive disease. Investigation of flow patterns of blood in the coronary arteries has been a challenge to ischemic heart disease researchers for many years. A major problem is the small size of the coronary arteries, which limits the spatial resolution in clinical imaging.

Many autopsy investigations have found that the distribution of atherosclerosis around the circumference of the lumen is eccentric in the proximal sections of the coronary arteries, and the distribution along the longitudinal direction in the entrance sections is also asymmetrical (e.g. Fox and Seed, 1981; Fox et al., 1982; Svindland, 1983; Crottum et al., 1983; Velican, C. and Velican, D., 1984; Ojha et al., 2001). These observations have led to an interest in the major segments of the coronary arteries that have relatively larger sizes. However, the entrance flow in coronary arteries is expected to be strongly affected by the flow pattern in the aortic root (Bogren and Buonocore, 1983), as well as by the specific geometry.

Entrance flow patterns in the coronary arteries will be determined by CFD modeling that includes the aorta and its coronary arteries. This requires an addition of velocity boundary conditions for the time-varying flow in the coronary arteries (Suo et al., 2002). As the spatial resolution of the PC-MRI technique is limited in the small sized arteries *in vivo*, we can only obtain the average velocities in the major branches of the coronary arteries. The waveforms of the velocities will be used in the distal sections of the right coronary artery (RCA), the left anterior descending coronary artery (LAD) and the left circumflex coronary artery (LCX) as the outlet conditions in the CFD modeling. If the lengths of the coronary arteries are sufficient (Fox and McDonald, 1978: $L/D \geqslant 0.06 \times Re$, where L is the length of the vessel, D is the diameter and Re is the maximum Reynolds number), the assumed velocity conditions on the outlet sections will not affect the flow patterns in the entrance sections.

In this study, the model of the left coronary artery includes the left main coronary artery (LM) and its bifurcation into the LAD and LCX, while the model of RCA does not include any branches.

1.5.4 Specific Aim 4: To Test Correlations between Entrance Flow Patterns and Atherosclerotic Plaque Distributions in the Proximal Sections of Human Coronary Arteries

It has long been observed that orifice regions or entrance sections of both the right and left coronary arteries are favorite sites for atherosclerotic plaques, and hemodynamic factors have been hypothesized as contributing to this localization (e.g. Fung, 1997; Fox, et al., 1982; Fung, 1996; Asakura and Karino, 1990) (see Figure 2.5). Many investigators (e.g. Fox and Seed, 1981; Svindland, 1983; Crottum et al., 1983; Stary, 1987; Ojha et al., 2001) reported that plaques are more concentrated on the myocardial side in the proximal segment of the right coronary artery, but the eccentric concentration of plaques is not notable in the orifice region of the left coronary artery. Another clinical autopsy investigation (Velican, C. and Velican, D., 1984) found there to be a region between the orifice and the main bifurcation of the left coronary arteries which has "natural resistance" to atherosclerosis by comparison to atherosclerotic involvement distal and proximal of the left main coronary artery. On the one hand, atherogenesis is favored in the vicinity of the aortic origin of coronary arteries and the main bifurcation of the left coronary artery as indicated by many investigators; on the other hand, between the both regions there is only a few millimeters and less atheroma. Given these observations, we hypothesize that there may be some special behavior in the hemodynamic environment

in the entrance regions of the coronary arteries that accounts for these specific plaque distributions (Suo et al., 2003).

The fourth specific aim will investigate possible correlations between hemodynamic factors and the distribution of atherosclerosis in these reported clinical observations. The hemodynamic factors are derived from the computed flow patterns, so the entrance flow patterns reproduced by the CFD modeling in previous specific aims are the basis for achieving the fourth aim, and our interests focus on the proximal sections of the right and left coronary arteries.

CHAPTER 2

CLINICAL BACKGROUND AND SIGNIFICANCE

2.1 Helical Blood Flow Patterns in the Aorta

Blood flow patterns passing through the heart and large arteries have been investigated for decades. Dean (1928) made the first prediction of helical flow in a curved tube. Rotation of the blood flow *in vivo* was detected early by Doby and Lowman (1961) who used a radiopaque streamer technique. Their studies demonstrated circular motion that persisted in the same direction throughout both systole and diastole in the ventricle. Irisawa et al. (1960) injected 5% saline into the left ventricle and observed that mixing was incomplete even after successive cardiac cycles, which suggested that streams of blood with different concentrations of saline swirl, but do not mix, within the ventricle throughout systole and diastole. Lynch and Bove (1969) used water-soluble radiopaque droplets and cineradiography to observe the blood flow in the canine heart and aorta. They found that radiopaque droplets trailed a helical path in the aortic arch during systole. Caro et al. (1994) studied blood flow patterns in patients using magnetic resonance angiography, and reported that anti-clockwise rotational flow patterns occupy the right common iliac artery while there was clockwise rotation in the left. Using Color Doppler ultrasound, Stonebridge et al. (1996) investigated the blood flow patterns in eleven healthy male volunteers in three sites: the right common and distal superficial femoral artery and the left common femoral artery with the hip straight and flexed to 15-20^0. All their subjects demonstrated a rotational element to forward flow during the pulse cycle, although the direction of rotation was not uniform.

Reports that the flow patterns of blood in the ascending aorta and the aortic arch may be skewed and twisted appeared in the 1970s (e.g., Seed and Wood, 1971; Clark and Schultz, 1973; Farthing and Peronneau, 1979). As techniques of clinical imaging developed, more investigators observed spiral flow patterns in the ascending aorta (e.g. Stein et al., 1979; Klipstein et al., 1987; Segadal and Matre, 1987; Frazin et al., 1990; Kilner et al., 1993; Bogren and Buonocore, 1999); however, the observations were limited to visualizations of the flow.

Studies by Segadal and Matre (1987) observed bi-directional flow in the ascending aorta from late systole to middle diastole, and blood appeared to rotate in a clockwise direction when observed from a left anterior position. Frazin's (1990) detection of rotational blood flow by using color-flow Doppler in the transverse aorta and proximal aorta in 53 patients was important. Using a transesophageal color-flow Doppler, he demonstrated diastolic counterclockwise rotation and systolic clockwise helical flow in a high percentage of patients. These results suggest that rotational flow begins in the proximal aorta and is carried through the descending aorta where flow is asymmetric with systolic clockwise and diastolic counterclockwise elements.

There were researchers who offered an alternative interpretation of the rotational blood flow in human arteries. Since the resolution of Doppler imaging was limited at this time, Thomas (1990) thought that the observed aortic clockwise and counterclockwise flow might be artifacts of the imaging technique. With the rapid improvements of clinical imaging techniques, particularly MR measurements of blood velocity, the generality of the spiral blood flow patterns has been accepted.

PC-MRI techniques made *in vivo* blood flow 3D visualization in large vessels a reality. Klipstein et al. (1987) investigated blood flow patterns in the human aorta using this technique. By this non-invasive method, they illustrated a dynamic, skewed flow pattern in the ascending aorta, such that the skew was symmetrical about the plane of the aortic arch in systole but reversed along the posterior left wall, while during diastole it continued forwards at the anterior right wall. Kilner et al. (1993) observed that a right-hand helical flow pattern predominated in the upper aortic arch in late systole, and retrograde flow originated from a region of blood with low momentum in end-systole, usually along the inner curved wall of aorta. They used three schematic drawings to illustrate the evolution of the flow patterns in the ascending aorta in one cardiac cycle (see Figure 2.1). They proposed that asymmetries in blood flow conserve energy and help flow smooth its passage to the next destination.

These numerous clinical investigations illustrated that spiral blood flow patterns with different directions of rotation commonly exist in the human ascending aorta and aortic arch. Though these studies did not present a quantitative description of the specific flow patterns, thus preventing an exploration of the causes, there are several factors among common knowledge in fluid dynamics that could account for helical blood flow in the aorta. These include: (i) the torsional motion of contraction of the left ventricle might impart rotation to blood ejected into the aorta; (ii) the opening and closing dynamics of the aortic valve leaflets and their asymmetric configuration could contribute to swirling flow; and (iii) the curvature and the twisted shape of the ascending, transverse and descending aorta may play a role (Suo et al., 2001).

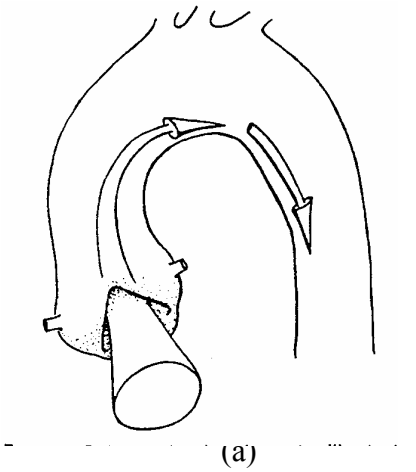

(a)

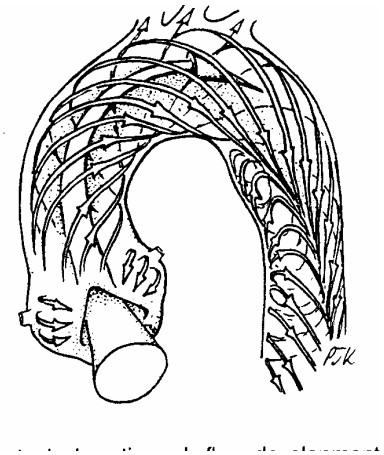

(b)

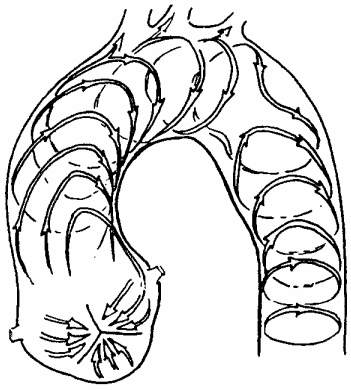

(c)

Figure 2.1: The blood flow patterns in ascending aorta, aorta arch and proximal descending aorta at flow acceleration phase (a), at flow deceleration phase (b) and at diastolic phase (c). (Copy from Kilner, P., et al. Circulation, 88 (5), 1993)

Experimental studies *in vitro* were used to test the cause of the rotational flow patterns (e.g. Agrawal et al., 1978). In a model of a human aorta, Yearwood and Chandran (1982) reported that helical flow was greatest near the inner wall and dissipated during diastole, and the maximum rotational velocities were 10-20% of the peak axial velocity. Many ideal curved tubes have been used as arterial models in steady or pulsatile experimental flow systems, and velocity profiles have been measured in curved sections (e.g. Murata et al., 1976; Inaba and Murata, 1978; Rushmore and Taulbee, 1978; Berger et al., 1983). Side-by-side double spiral flow patterns, or symmetrical secondary flow patterns, in the curved sections of the tube can be seen always, and consequently the curvature has been considered the cause of the spiral flow patterns, after the phenomena reported by Dean (1928). Although all these experimental results supported the concept that the spiral flows result from vessel curvature, usually investigators did not explore possible contributions from other sources.

CFD has also been used to investigate the causes of spiral flow patterns in the aorta. Chang and Tarbell (1985) simulated flow in the aortic arch in a numerical model of an ideal curved tube with periodical sinusoidal inlet waveform using CFD. Their results revealed a wide variety of flow phenomena including detailed descriptions of the velocity distribution of the rotating flow patterns and the WSS distribution produced by the spiral flow, data that are difficult to obtain by experimental methods. Komai and Tanishita (1997) investigated the flow in a similar numerical model that had a fully developed inlet flow with a waveform consisting of a pulsatile systolic flow period followed by a stationary diastolic period. Although the inlet velocity waveform of their modeling was different from that of Chang and Tarbell, both results were similar. A numerical model

with geometrical structure of an infinite helically coiled pipe was tested using CFD by Zabielski, L. and Mestel, J. A. (1998). The model had strong geometrical curvature and torsion, so that the secondary flow was amplified and flow separation occurred. However, the ascending aorta and the aorta arch are not ideally coiled tubes, and other computational simulations which more closely mimicked the curvature of the aorta did not fully reproduce flow patterns observed *in vivo* (Liu, 2000), leading to suspicions that other reasons, such as rotational secondary flows originating from the heart, may be significant factors.

2.2 Blood Flow Patterns in Coronary Arteries

The measurement of blood flow velocity in human coronary arteries has been a challenge for research into coronary heart disease because the vessels have a relatively small size and hide deeply within the body. Ultrasound Doppler catheter and PC-MRI are the most accurate and widely used methods to get the blood flow velocity information in the coronary arteries *in vivo* at the present time, though they have distinct deficiencies. Doppler-derived measurements using catheter- based systems are subject to errors due to the presence of the catheter, since it may interfere with flow. The disruption of blood flow would also tend to flatten the velocity profile, leading to reduced peak velocity measurements (Segadal and Matre, 1987). A significant drawback is that the method is invasive and can only be used in patients. PC-MRI is a convenient and noninvasive method, but its limited spatial resolution is a deficiency in measurements in coronary arteries (Sakuma et al., 1999).

Individual blood flow waveforms in the RCA, LAD and LCX of patients or volunteers have been investigated using these methods (e.g., Figure 2.2; Keegan et al., 2004), and some waveforms measured by one method were validated by another method simultaneously (Hundley et al., 1996; Nagel et al., 1999). These waveforms give velocity information in individual human coronaries, although they only detect the velocity in a sample volume that is too large to yield a velocity profile. Thus, the complex flow patterns that possibly happen in the entrance and bifurcation sections of the coronary arteries have not yet been illustrated *in vivo*.

Experimental and computational methods *in vitro* are used to make up the deficiency of the *in vivo* methods. Asakura T. and Karino T. (1990) performed an experimental study to observe steady flow through an excised the human coronary artery. In the experiment, the vessel was made transparent through soaking it in a fluid, and the aorta and the cannulated left and right coronary arterial branches were connected via plastic tube with a reservoir. Steady flow was obtained using a constant head tank. A microscope and camera recorded the traces of small particles (50-165 μm) that were suspended in the fluid. The streamlines in the entrance sections of the right and left coronary artery, and the streamlines in the main bifurcation of the left coronary artery were visualized (see Figure 2.3). The particle velocity data can be employed to estimate velocity profiles and wall shear stresses. The experimental method, however, is difficult to employ for pulsatile studies due to the large number of particles that must be tracked over time to provide full information.

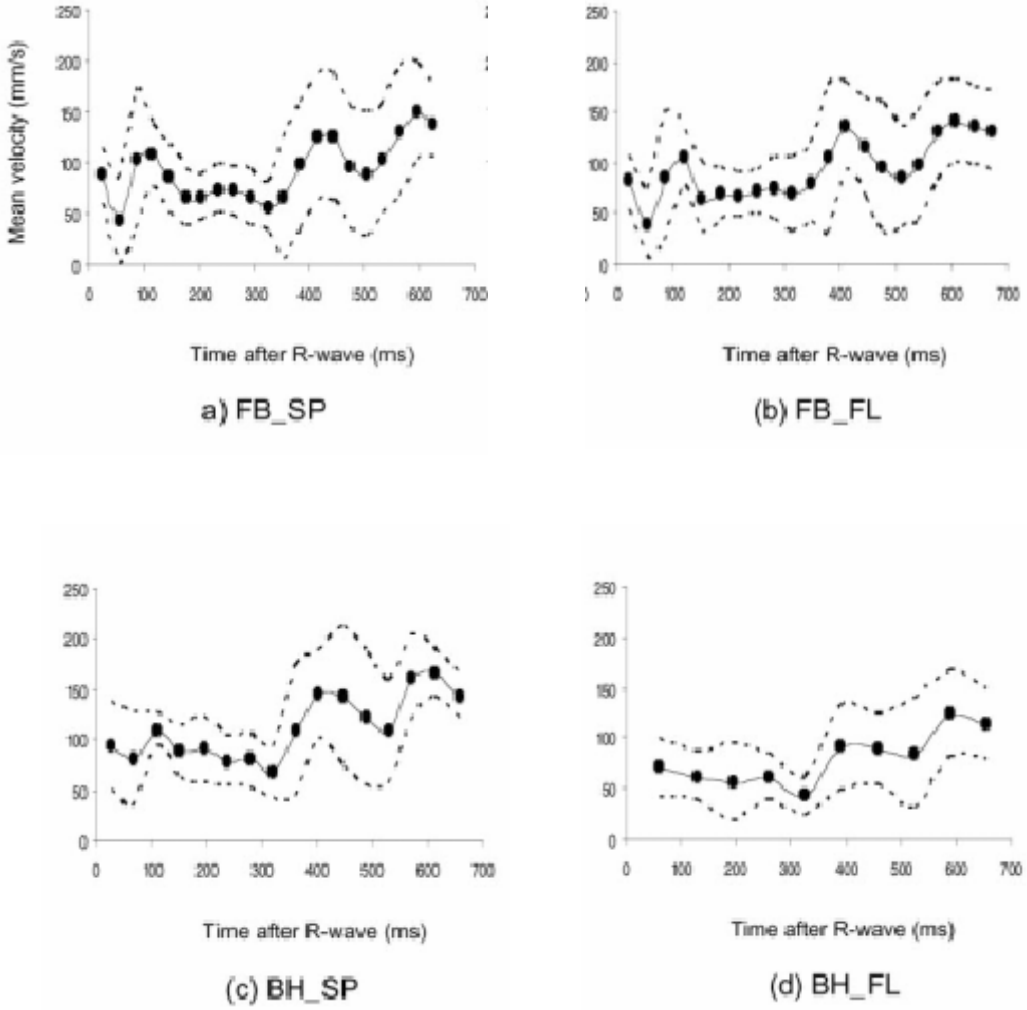

Figure 2.2 (a): Mean (±SD) velocities as measured by the FB_SP (**a**), FB_FL (**b**), BH_SP (**c**), and BH_FL (**d**) sequences in the left coronary arteries ($N = 8$). (Copy from Keegan, J., et al. J. Magn. Reson. Imaging, 19: 45, 2004)

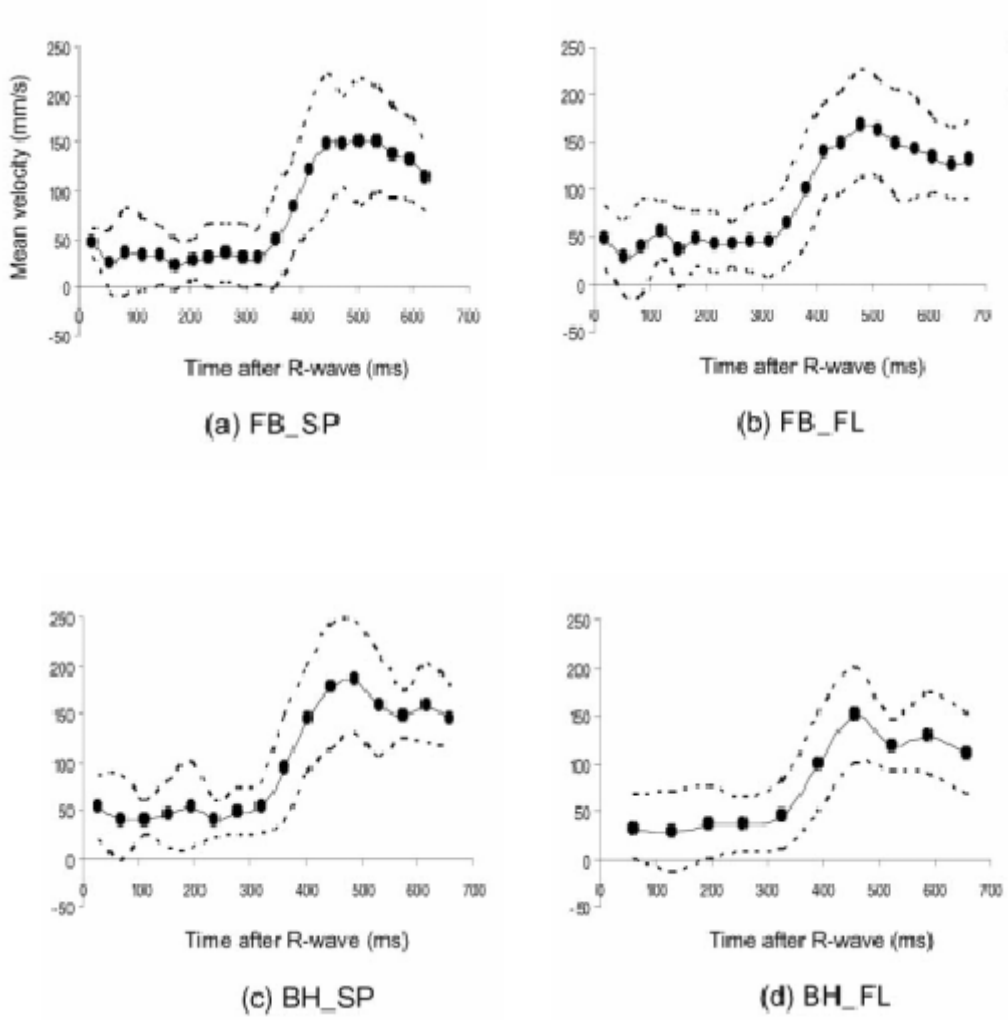

Figure 2.2 (b): Mean (±SD) velocities as measured by the FB_SP (**a**), FB_FL (**b**), BH_SP (**c**), and BH_FL (**d**) sequences in the left coronary arteries ($N = 8$) after correction for the through-plane motion of the vessel. (Copy from Keegan, J., et al. J. Magn. Reson. Imaging, 19: 45, 2004)

Langenhove, et al. (2000) simulated the blood flow in the right coronary artery of a patient using intracoronary ultrasound combined with CFD methods. Their modeling first demonstrated a helical flow patterns located on the stent region of the patient.

However, the entrance flows of coronary arteries are expected to be strongly affected by the flow in the aorta root, as may be inferred from the particle path lines of Figure 2.3. After investigating blood flow patterns in the root of the ascending aorta using magnetic resonance velocity mapping *in vivo*, Bogren et al. (1999) predicted that the blood flow into the coronary arteries may vary among individuals, according to flow patterns in the ascending aorta. Ignoring the effects of the specific flow patterns in the aortic root upon entrance flow in the coronary arteries may be expected to result in less than realistic velocity and wall shear stress predictions.

2.3 Atherosclerosis in Proximal Segments of Coronary Arteries

Clinical autopsies have found that the proximal sections of both right and left coronary arteries are favorite sites for localization of atherosclerotic lesions, and for decades hemodynamic factors have been hypothesized as contributing to this localization (Figure 2.4; Debakey et al., 1985).

Chopra, P. et al (1983) studied the coronary arterial stenoses from 131 autopsies of 5-80 year old subjects. They found that more than 60% of the lesions were eccentric on the arterial section, and the largest lesions were located in the proximal segments of all the main arteries. The LAD has the greatest lesion involvement followed by the LCX and RCA. Fox and Seed (1981) correlated atheroma distribution with vessel geometry in coronary arteries from more than 50 subjects dying of non-cardiovascular causes under

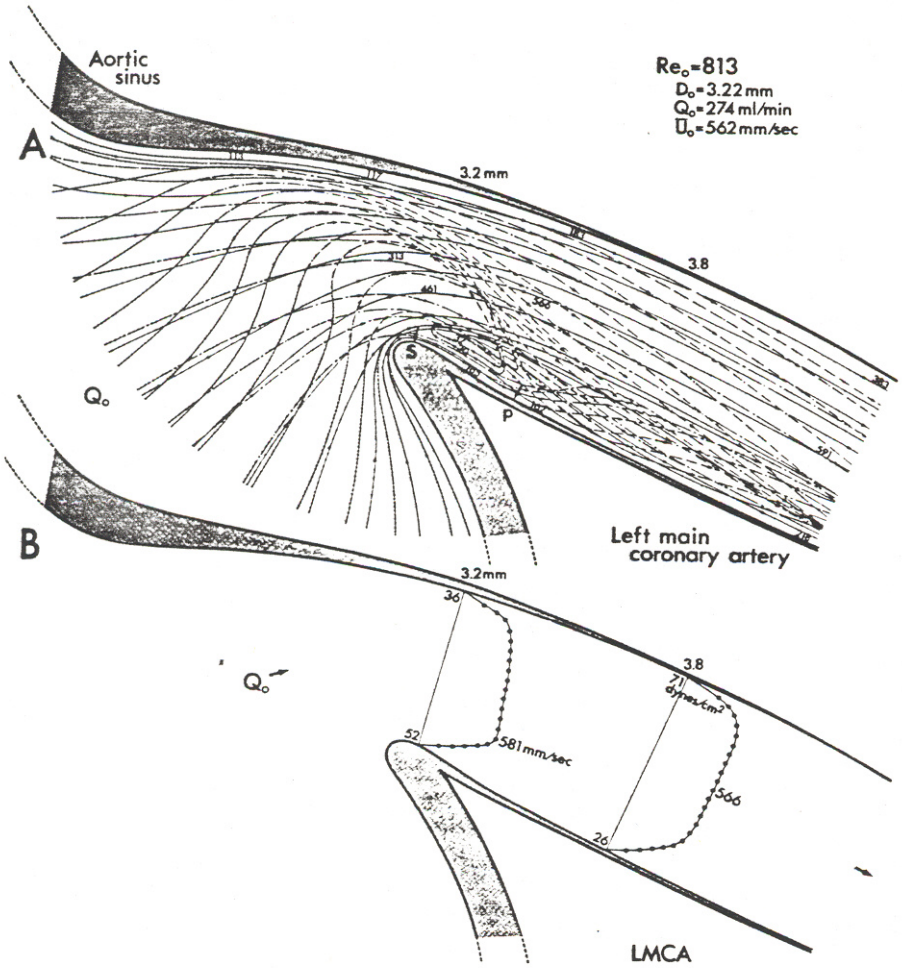

Figure 2.3: Visualization of streamlines and flow patterns (steady flow) in the entrance region of the left coronary artery obtained from an autopsy subject whose death was not caused by cardiovascular disease. (Copy from Asakura and Karino, Circulation Research, 66 (4), 1990)

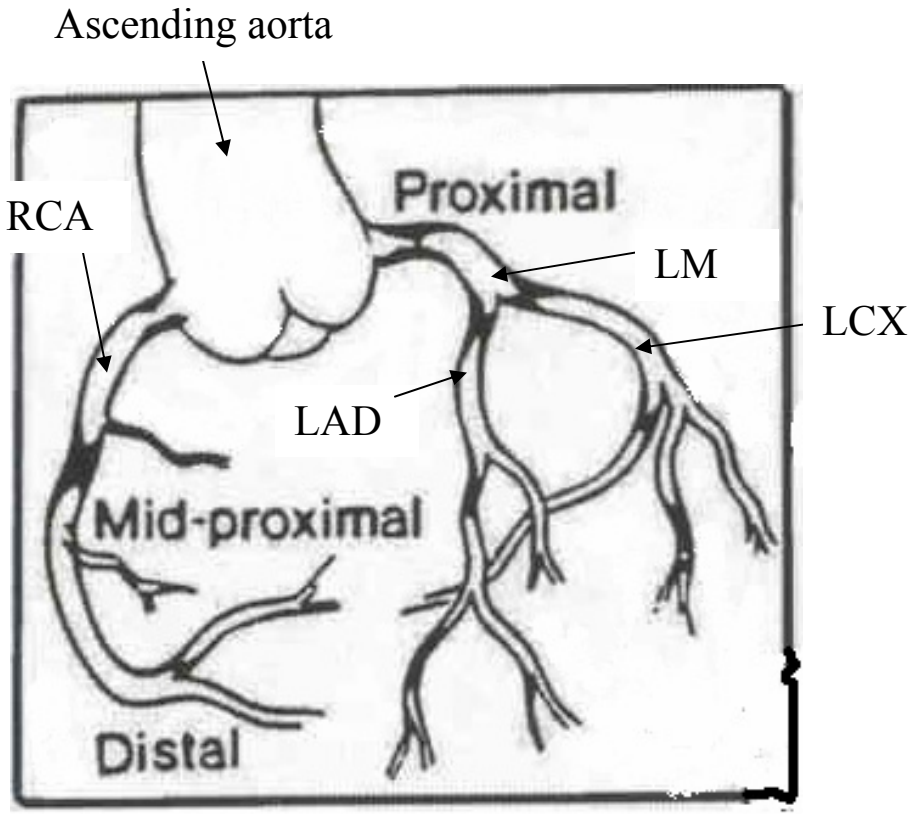

Figure 2.4: Distribution of atherosclerotic occlusive disease in human coronary arteries. (Copy from Dr. Michael E. DeBakey, Annals of Surgery 201:116, 1985)

40 years of age. Upon measuring the circumferential and longitudinal position of each atherosclerotic plaque in the major coronary arteries in every subject, they found:

- In the right coronary artery, severity of disease decreases downstream from the orifice and there is a tendency for plaques to be concentrated in the myocardial side of the lumen (Figure 2.5).
- The asymmetrical concentration of disease (in circumference) was not evident in the orifice region of the left main coronary artery, although the phenomenon has been found in the LAD and LCX.

Ojha, et al. (2001) investigated the distribution of intimal and medial thickening in the proximal RCA in 17 autopsies from non-cardiac deaths and found similar eccentric distributions of the thickening (Figure 2.6) as in the investigation of Fox. Stary (1987) surveyed the location of macrophages and foam cells in the coronary artery intima of 63 children that died at age less than 5 years old. He found the eccentric distribution of intimal thickening in the main bifurcation of the left coronary artery, but not in the proximal segments of left main coronary artery.

Velican, C. and Velican, D. (1984) examined 270 subjects who died of accidental causes, and investigated the distribution of atherosclerosis in the coronary arteries in these subjects. They observed that in subjects of similar age, sex and branching anatomical pattern and in the presence of similar risk factors for coronary heart disease, the first centimeter distal to the aortic origin of both left and right coronary arteries behaves differently than the second and third centimeters (Figure 2.7). These investigators concluded that the middle segment of the left main coronary artery that is

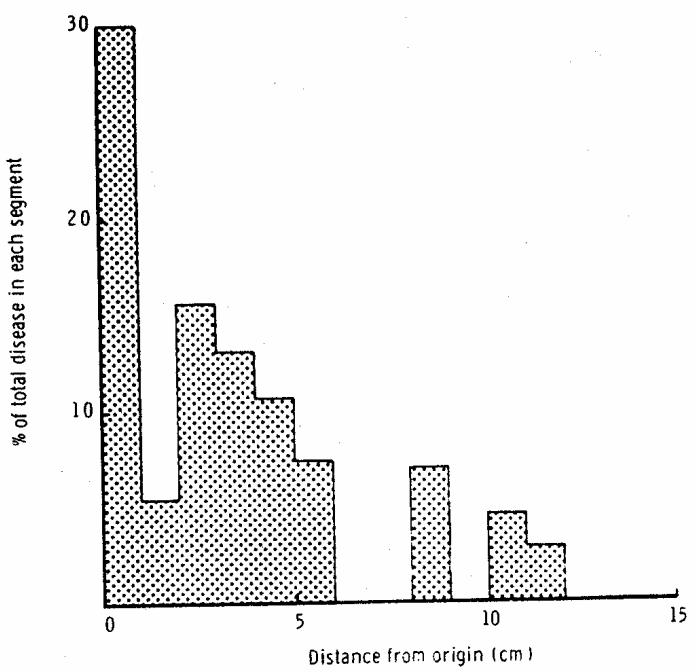

Fig. 3(a) Longitudinal distribution of early disease in l-cm steps from origin of RCA. Data pooled from l4 vessels.

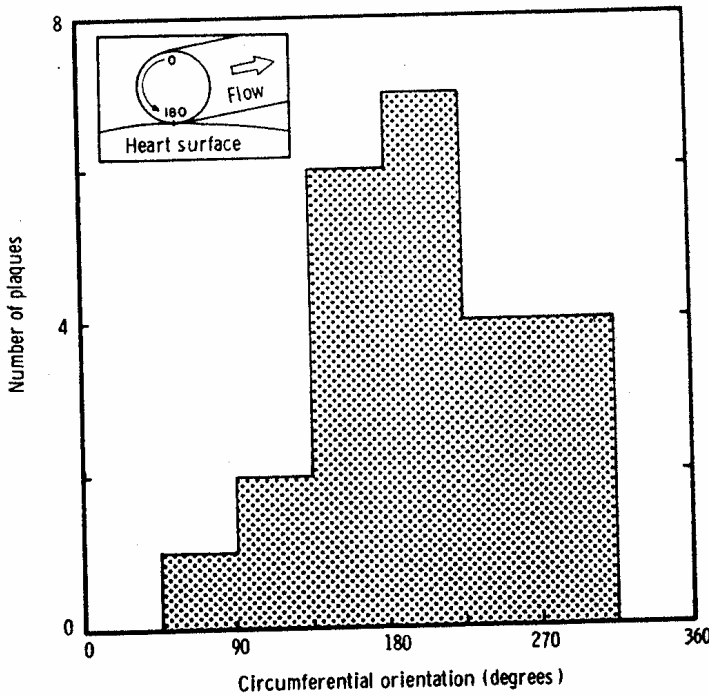

Fig. 3(b) Histogram of plaque location, pooled in 45-deg steps, around circumference of RCA. Circumferential orientation inset.

Figure 2.5: Histogram of plaque location, pooled in 45-deg steps, around circumference of RCA. (Copy from Fox and Seed, Atherosclerosis, 41:341-342, 1982)

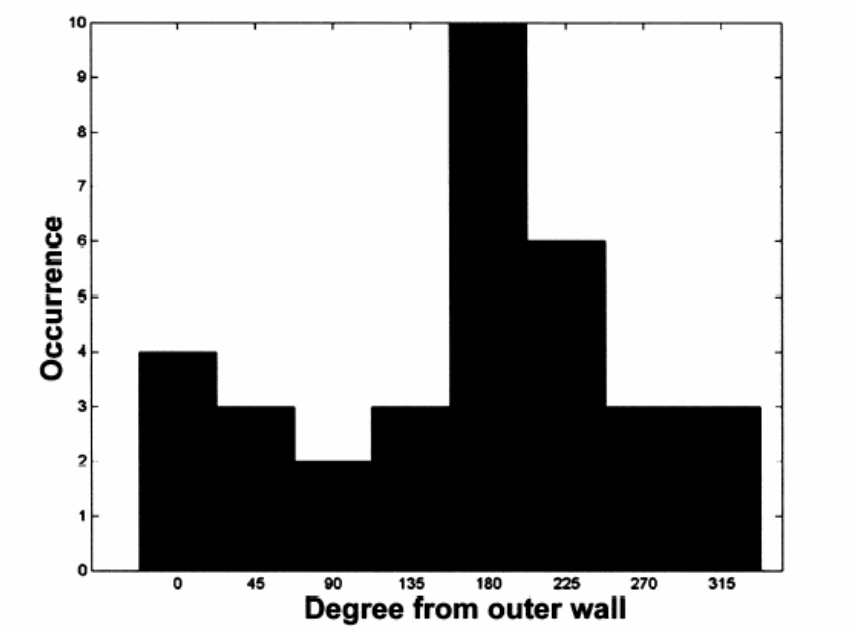

Figure 2.6: Frequency distribution of the peak intimal thickness among the eight segments of the proximal RCA. (Copy from Ojha, et al. Atherosclerosis, 158:150)

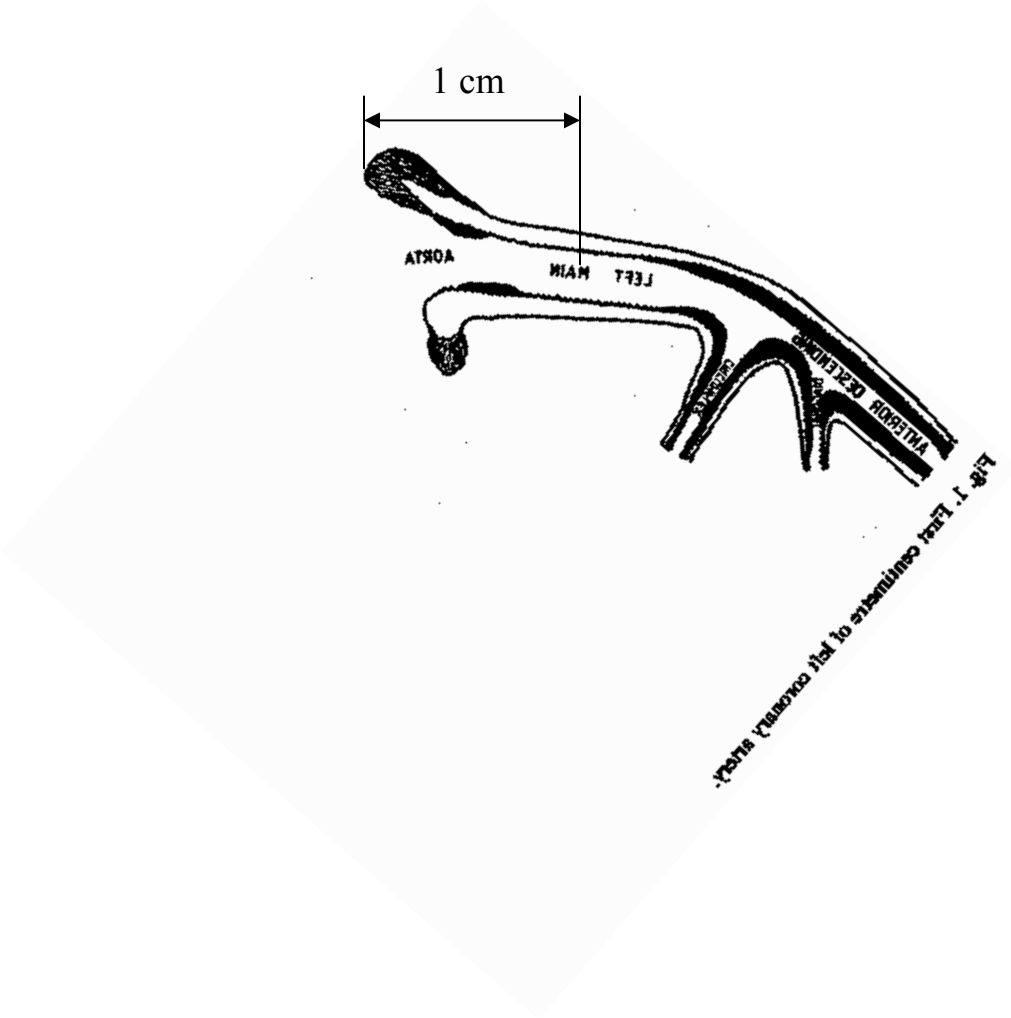

Figure 2.7: A region with resistant to plaque development is at one centimeter distal to the ostium in left coronary artery. (Copy from Velican, C. and Velican, D. Atherosclerosis, 50:176, 1984)

beyond about one centimeter distal to the ostium is more resistant to intimal thickening and plaque development than the orifice region and the main bifurcation region.

Svindland (1983) studied the localization of early sudanophilic and fibrous plaques in the main stem and proximal branches of opened and stained left coronary arteries from autopsies of subjects who died from trauma. He illustrated the distribution of sudanophilic and fibrous plaques in 41 arteries by contour lines connecting points with equal frequency of lesions (Figure 2.8). From the shape of the contours it can be seen that a lower frequency of lesion localization occurs between the aortic orifice region and the main bifurcation. Another clinical observation may also support the specific distribution of the lesion in the left coronary artery: Lewis et al. (2001) noted that a short main left coronary artery was present in a greater proportion of patients with complete left bundle-branch block. The work of Gazetopoulos et al (1987) also supports this observation, and they suggested that a shorter length of the main left coronary artery is one of the factors that may contribute to the development of atherosclerosis in its branches. In this study, we suggest that the clinical observations noted by others may be explained by the hypothesis that a shorter left main coronary artery eliminates the anti-atherogenic flow environment that was proposed by Velican, C. and Velican, D (1984). In such cases, the entrance flow of the left coronary artery will connect with the flow in the main bifurcation so that both flow environments that favor atherogenesis may enhance each other.

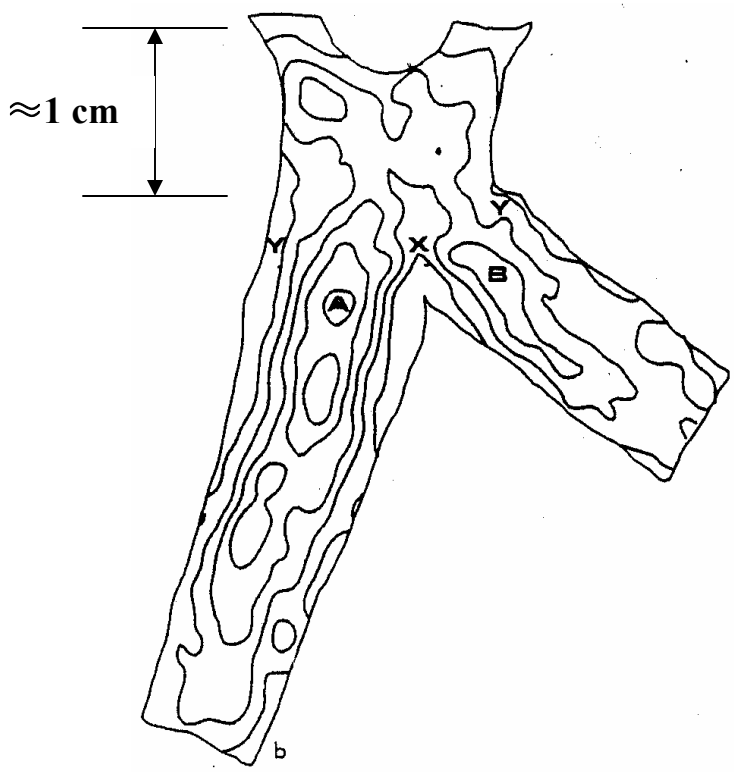

Figure 2.8: Frequency distribution of lesions in 41 opened left coronary arteries. (Copy from Svindland, A., Atherosclerosis. 48:141)

2.4 Relationship between Atherosclerosis and Blood Flow Patterns

After observation of one 115 patients with suspected carotid disease by color Doppler ultrasound and MRI recently, Houston et al. (2002) concluded that spiral blood flow is seen in the aortic arch and carotid arteries of patients with no carotid disease, while carotid atheromatous disease is associated with a significant reduction in the prevalence of spiral flow. However, it should be pointed out that the study proposed no specific causative mechanisms to explain these observations. The presence and the clinical importance of rotational blood flow may require more extensive investigation.

In the aorta, many investigators predicted pathogenicity for helical flow patterns. Frazin et al. (1990) suggested that rotational flow might be important physiologically because the centripetal spin of blood may account for a significant amount of normal organ perfusion by branch vessels. Pathologically, there may be a relation of the shear forces caused by rotational flow to the development of atherosclerotic plaques and the direction and extent of aortic dissection. However, clinical issues such as the replacement of artificial heart valves, the selection of the localization of the origin of coronary bypass grafts in the ascending aorta, and the rejection of transplanted hearts offer invitations to the study of flow patterns in the arteries around the heart, areas of investigation which have not yet been fully explored.

CHAPTER 3

METHODOLOGY

3.1 Medical Imaging and CFD Modeling

X-ray angiography has been employed in 3D model reconstruction of arteries in CFD studies (Gibson et al. 1993). In order to capture the spatial structure and motion of the coronary arterial tree, reconstruction of a coronary CFD model requires at least two x-ray projections. Advanced x-ray imaging technology can provide rapid acquisition of multiple projection images (Fahrig et al. 1997), from which the 3D vessel geometry can be reconstructed at higher resolution than from other medical imaging methods. This is the unique advantage of x-ray angiography in comparison to other medical imaging. However, angiography requires injection of a contrast medium directly into the coronary arteries via an inserted catheter. The great disadvantage of x-ray angiography is its invasive nature, so it is inappropriate for use in carrying out hemodynamic investigations in healthy subjects.

CT is also based on x-rays, but it does not require actual invasion of the body with catheters. CT is used increasingly to detect calcified plaques in the coronary arteries (Schmermund and Erbel, 2001). Although CT can produce higher resolution geometry images of arteries than can MRI, it cannot supply any blood velocity information in the arteries. Also, CT uses ionizing radiation, so there are limits on the frequency and intensity of its use.

Another vascular imaging technique, ultrasound, is often the most convenient and least expensive of all medical imaging methods. Ultrasound imaging is formed by

transmitting a high frequency sound beam into body, then collecting echoes to produce an image whose intensity is related to the echoes from the tissue. Generally, the quality of ultrasound images is inferior to x-ray images and MRI. Ultrasound imaging of vascular anatomy, though commonly used in the clinic, has not yet played a significant role in image-based CFD analysis as the scanning probe is usually manually operated, from which the reconstruction of 3D arterial models is difficult. An advantage of ultrasound is that Doppler ultrasound can provide blood velocity information *in vivo* in real time, though it does suffer from lack of good spatial resolution in most clinical applications.

Intravascular ultrasound (IVUS) has been developed and used in image-based CFD modeling studies recently because it presents high quality images of an arterial lumen from inside of the vessel (e.g. Chandran et al., 1996; Ilegbusi et al., 1999; Krams et al., 1997). In this case, X-ray angiography helps to guide the coordination of the transducer for the 3-D reconstruction of the inner boundaries of the vessel. Since these are invasive procedures, IVUS-based CFD modeling studies have been limited to animals and special patients.

The great advantage of MRI is its non-invasive nature. MRI can distinguish different soft tissues and is very sensitive to moving objects like blood, so that MRI is particularly attractive in observing the vascular system. The negligible risk associated with the use of MRI scanning also makes it easier to study differences between patients and normal volunteers. These advantages make MRI an important companion for image-based CFD studies in hemodynamic research (e.g. Tasciyan et al., 1993; Long et al., 1998; Wang et al., 1999; Zhao et al., 2000).

Although MRI is suitable for distinguishing the boundary between blood and vessel wall, it is difficult to distinguish the outer boundary of the vessel wall when the vessel is surrounded by similar tissues. This degrades the reliability of wall thickness measurements (Ladak et al., 2001), although recent work suggests that the dynamics of wall boundary motion might also provide important information about pathology of the vascular wall (Aoki et al., 1999).

PC-MRI, in which blood velocity information is encoded into the phase of the MRI signal, can provide the velocity distribution on an arterial section in real time. This is so important that it allows MRI to overtake other methods that combine with CFD in modeling *in vivo* blood flows in arteries, because MRI supplies both geometrical and velocity for use as boundary conditions in CFD simulations (Milner et al., 1998).

3.2 CFD and Hemodynamics

CFD has become an essential tool in almost every branch of fluids engineering, including hemodynamics (Meairs et al., 1995). CFD is commonly accepted as referring to the broad topic encompassing the numerical solution, by computational methods, of the set of Navier-Stokes equations, continuity and any additional conservation equations. There are many available commercial CFD software packages that can solve the equations, which rescue us from tedious programming. Therefore, our task of CFD becomes the selection and use of a software package among several commercial products, such as CFD-RC, FIDAP, STAR-CD, CFX and FLUENT.

Two numerical methods for solving the Navier-Stokes equations are the foundations of these software packages: finite element method and finite volume method:

- The finite element method uses simple piecewise polynomial functions on local elements to describe the variations of the unknown flow variables. When these approximate functions are substituted into the governing equation, it will not hold exactly, and the concept of a residual is introduced to measure the errors. These residuals are then minimized by multiplying by a set of weighting functions and then integrating. This yields a set of algebraic equations for the unknown terms of the approximating functions, and hence the flow solution can be found.
- The finite volume method employs an integral form of the conservation laws directly in each finite cell volume. Finite difference type approximations are then substituted for the terms of the integrated equations, forming algebraic equations that are solved by an iterative method. The finite volume method has some advantageous characteristics, like being suitable for deforming meshes and local reproduction of boundary conditions, which makes it more widely used in current commercial CFD codes.

CFD-RC is one of the most popular software packages because it is based on the finite volume method and has user-friendly pre- and post-processing functions (CFD Research Corporation, 2001).

With the great advances in computer technology, CFD has developed very quickly in hemodynamics research. These developments are complementary to experimental fluid dynamics, an other important research method of fluid mechanics, and also provide much greater flexibility to study different geometries and flow conditions. For example, computer aided design software makes the numerical description of a 3D arterial lumen

with complex surfaces much easier than manufacturing the physical model of the vessel and placing this in a laboratory flow system. The numerical description can be conveniently transformed to a CFD model. In addition, because PC-MRI can provide inflow and outflow boundary conditions from *in vivo* measurements, the combination of CFD with MRI allows a more thorough exploration of the details of blood flow in human arteries than has previously been possible.

An important step in using CFD simulations is validation of the results. The traditional validation is by comparison with experimentally measured data, typically laboratory models. In the CFD/MRI method, PC-MRI scanning substitutes for laboratory model experiments, so its results can be used both as the boundary condition data for CFD calculation and, in the interior of the solved region, for validation of the CFD results.

3.3 Image Processing of MRI Slices

All MRI slices used in the thesis came from healthy subjects who were studied at the Emory University Hospital, and the procedures followed protocols that were approved by Emory University's Human Subjects Committee of the Institutional Review Board. These MRI slices were the foundation of this research, as all data on the geometries and flow velocities *in vivo* were abstracted from these slices. Therefore, image processing of MRI slices becomes the first step in the hemodynamic research. Instead of using commercial software in the image processing, all the necessary programs were written in Matlab, thus providing flexibility in linking image results and CFD model reconstruction.

Four aorta models were reconstructed from four healthy volunteers and employed in the research. The principal methodologies in these reconstructions, for example, MRI image processing, surface smoothing and motion information abstracted from PC-MRI slices, were the same except for some local improvements of the programs. Only one of these models will be used to describe the methodology developments in subsequent sections.

3.3.1 Interface Operation

Figure 3.1 shows a group of MRI slices from a transverse thorax MRI scan of a healthy volunteer using a 1.5T scanner (Philips Medical System), in which ET:27, TR:2000, TE:80, and each image has 256×256 pixels in a view of 350×350 mm with a thickness of 3 mm. The slices included 44 sequential images that are across the ascending aorta, the aortic arch and the proximal descending aorta. Before performing any image processing from the slices, we need an interface platform to assemble and operate on the individual 2D slices in 3D space.

The interface programs can read in the images, form a 3D space of MRI data and contribute an interface environment for the operator to perform various operations, for example, viewing the artery globally in different angles and arbitrarily re-slicing the locally interesting parts. To do these, a 3D coordinate system was first created in the data space based on the image coordinates. The origin of this 3D system was located in the upper left of the first image, the X axis was from the left to the right on the image plane, the Y axis was from the top to the bottom, and the Z axis was from the first image to the 44th image.

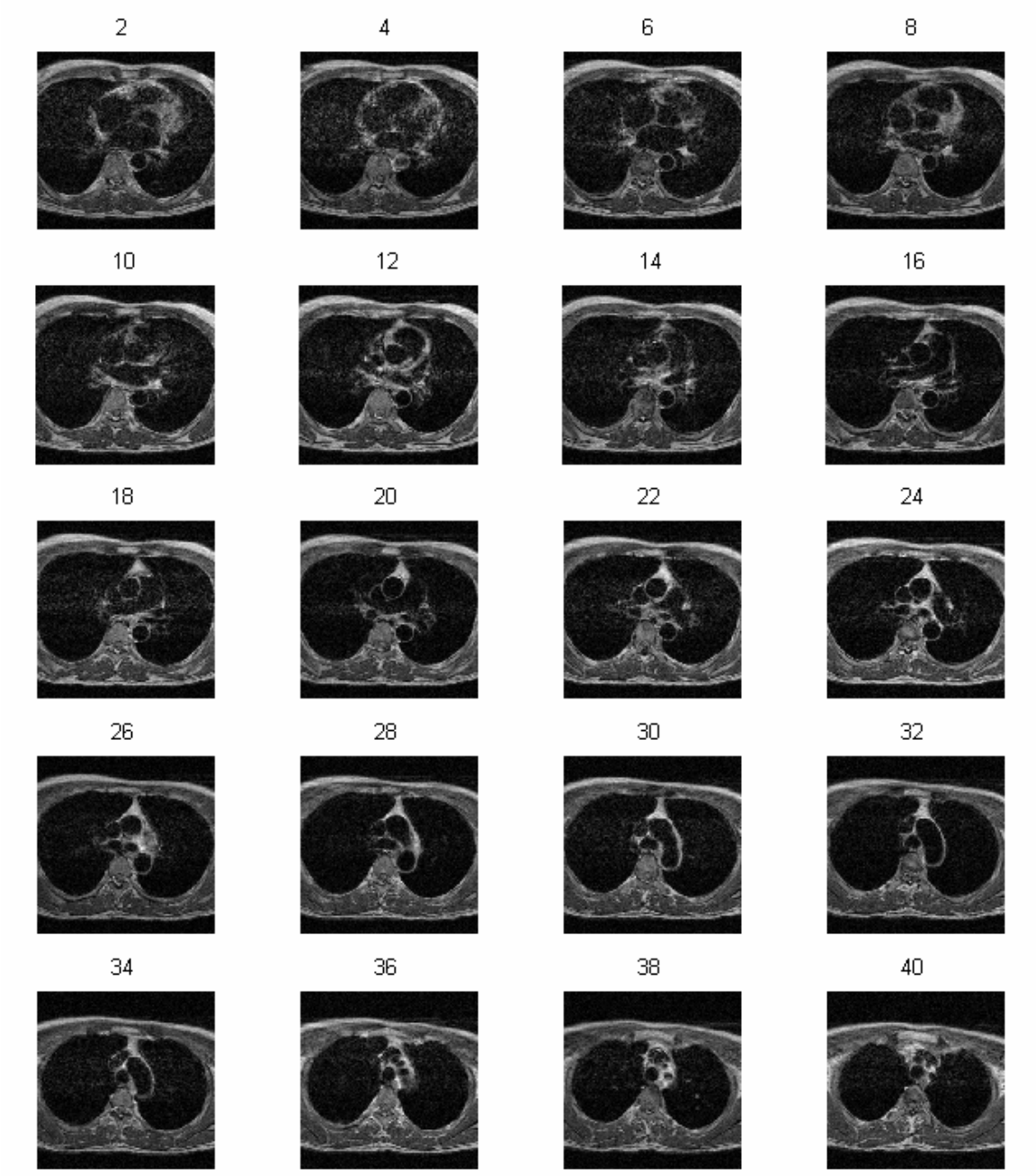

Figure 3.1: Transverse thorax MR slices of a healthy volunteer - 1.5T scanner (Phlips Medical System); ET:27, TR:2000, TE:80; 256×256 pixels in a view of 350×350 mm; 3 mm thickness.

An arbitrary plane that went across the coordinate system was created according to some specific conditions, so that the plane formed a new slice in the data space and showed different viewing from that of the original image. For example, this plane may be formed by three spatial points of the arterial lumen that were located on different images, in which case the plane would go across interesting parts of the lumen that was restricted by the points. Several examples are presented next for illustration.

A sagittal re-slicing in the data space is shown in Figure 3.2 (a) where the slice was across the lumens of ascending aorta, aortic arch and descending aorta. Three points were selected individually on different images: the first point was in the anterior boundary of the lumen of the ascending aorta on the 16th image (see Figure 3.1); the second point was in the posterior boundary of the lumen of the descending aorta on the same image; the third point was in the middle of the lumen of the aortic arch on the 34th image. The three points determined a plane that was across the sagittal lumens of the ascending aorta, aortic arch and descending aorta. The re-sliced images present a global view of the aorta that could not be seen from the original slices directly (as Figure 3.1 shows). Note the two branch arteries (right subclavian and left carotid) of the three aortic arch branches can be seen in the re-slicing.

Another 3 points were individually selected in the right boundary, in the left boundary and in the middle of the lumen of the ascending aorta on the 16^{th} and 24^{th} images so that a coronal re-slicing showed the lumens of the ascending aorta and aorta root (see Figure 3.2 (b)). The coronal curvature of the ascending aorta and the aortic sinus can be seen in the slice.

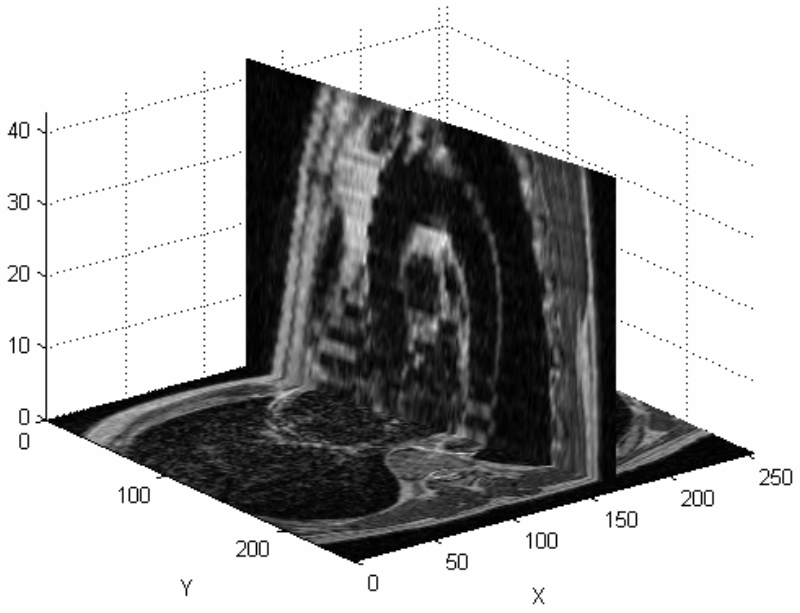

Figure 3.2 (a): The sagittal re-slicing of the MRI data space shows the lumen of the ascending aorta, aortic arch and descending aorta.

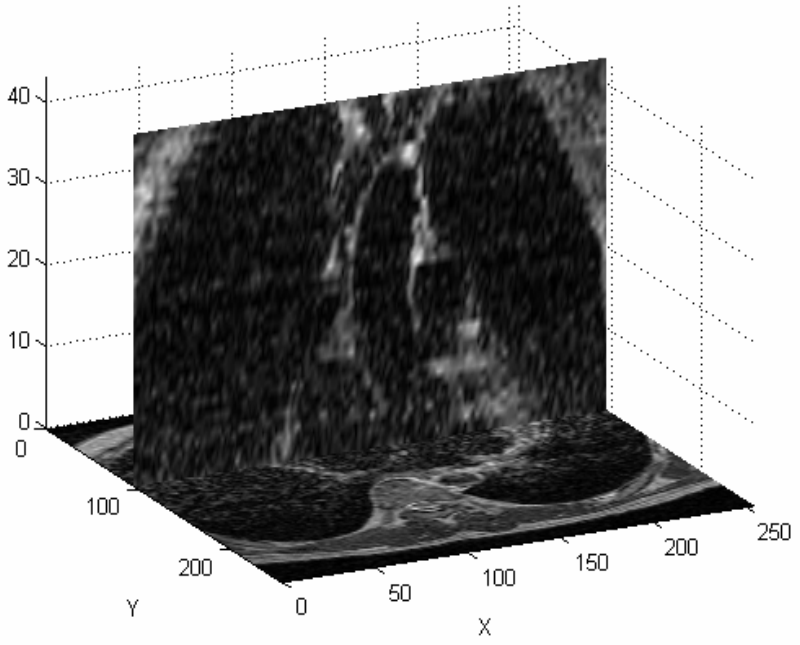

Figure 3.2 (b): The coronal re-slice shows the tortuous lumen of the ascending aorta.

An oblique transverse re-slicing that goes across the sharp bending region in the ascending aorta is shown in Figure 3.3 (a). The re-slicing was determined by one point that was in the inner curvature boundary of the lumen of the ascending aorta on the 26th image, and a vector that was normal to the plane, which controlled the plane to be parallel with the X axis but could be rotated in the Y-Z plane. The re-sliced image not only helps understand the lumen's geometry near the aorta arch in detail, but also aids in selecting the best re-slicing position for local lumen segmentation where the lumen is sharply bent. The re-sliced section is always selected to be perpendicular to the longitudinal direction of the local lumen.

Sometimes, the details of structures and orientations of the arteries can not be clearly seen from the original transverse slices so that parallel re-slicing or image interpolation is needed. In this study, the locations and orientations of the coronary arteries related to the aorta root were difficult to determine from the original slices, as shown in Figure 3.1. Two transverse slices could be created by going across the aorta orifice and parallel to the major trunks of the coronary arteries. Image interpolations then enhanced the resolution of the images. One image of such a re-slicing is shown in Figure 3.3 (b), where the locations of the orifices and the orientations of the major vessels of the right coronary artery (see the left image in Figure 3.3 (b)) and the left coronary artery (see the right image in Figure 3.3 (b)) related to the aorta root can now be distinguished.

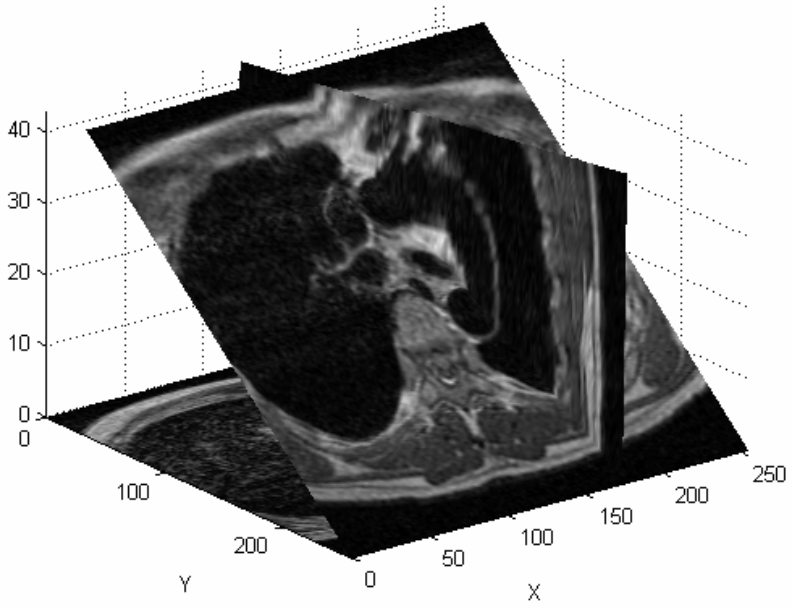

Figure 3.3 (a): The oblique transverse re-slice shows the lumen of the aortic arch, which appears nearly a circular.

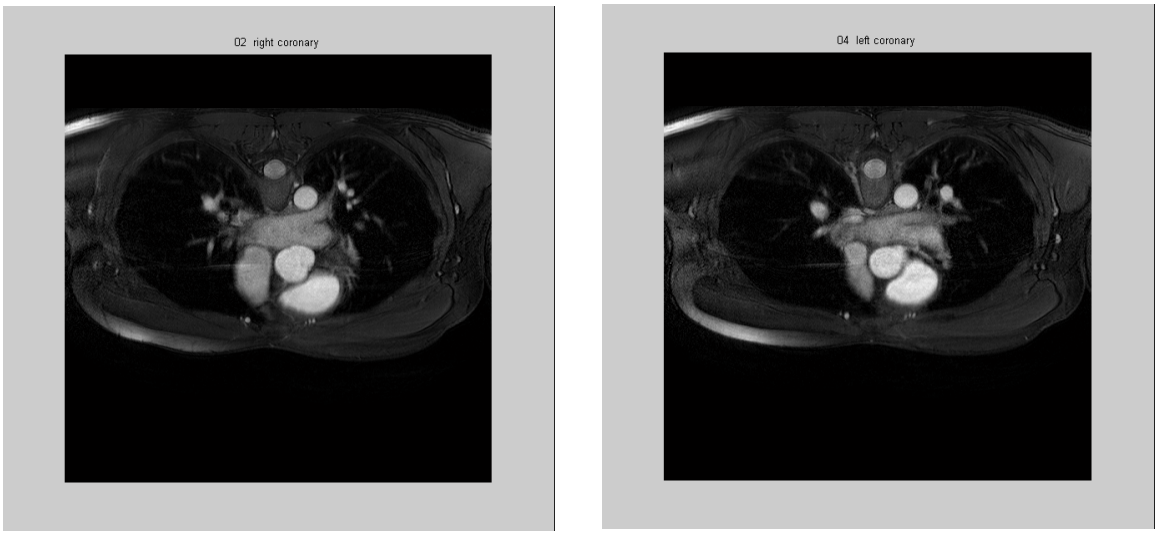

Figure 3.3 (b): The left image shows the alignment of the trunk of the right coronary artery; and the right image shows the trunk of the left coronary artery after parallelly re-slicing between two slices.

3.3.2 Snakes Segmentation Method

Image segmentation is necessary to find the boundary of an arterial lumen on the slice of the artery. There are many candidates for segmentation methods in image processing, depending on the object. An important geometric characteristic of arteries is that the transverse lumen approach to a circular because of the blood pressure inside the vessel and the elasticity of the wall. This characteristic makes the Snakes method (Hohnhauser, B. and Hommel, G. 2003) one of the most attractive for segmenting vascular lumens in medical images.

Snakes segmentation imitates the energy minimizing process in nature, in which the contour characteristics of an active curve can be described through an energy equation. As an active curve, the contour moves like a snake under the control of image intensity forces and the curve properties. The image forces, usually related to the gradient-based image potential, push the points of the contour toward the edge boundaries in the image. The curve properties of the contour also influence the shape of the contour and the goal is usually to keep a smooth contour. Since the Snakes model was introduced by Kass in 1987, many studies have been done to improve the performance of this model.

Below is the classical formula of the energy function of a gray image (Kass et al, 1988). Here, the integral is taken along the curve *c*, and the energy terms are functions of *c* or the derivatives of *c*. The constants α and β control the relative weight of the corresponding energy.

$$E = \int_0^1 (E_{image} + \alpha E_{smooth} + \beta E_{rig}) ds$$

Smoothing term: This term makes the contour act like a smooth curve. It corresponds with the bending force of the smoothness of the curve or contour. The continuous form of this term is given by:

$$E_{smooth} = \left\| \frac{dc}{ds} \right\|^2$$

where: s is the arc length of the curve.

As the image is composed of pixels, or discrete points, the term is approximated by discrete forms. In the transformation, we must consider the balance between resolution of the discrete forms and the limited numbers of pixels in the interesting region. Expanding the equation gives

$$\left\| \frac{dc}{ds} \right\|^2 = \left(\frac{dx}{ds} \right)^2 + \left(\frac{dy}{ds} \right)^2 = \frac{(x_{i+1} - x_i)^2 + (y_{i+1} - y_i)^2}{(\Delta s)^2}$$

Rigid term: This term aims to avoid oscillations of the active contour. Penalizing high contour curvatures is a good way of achieving this goal. The curvature is estimated by the second derivative of the contour. Hence, the rigid energy can be formulated as follows:

$$E_{rig} = \left\| \frac{d^2 c}{ds^2} \right\|^2 = \left(\frac{d^2 x}{ds^2} \right)^2 + \left(\frac{d^2 y}{ds^2} \right)^2 = \left(\frac{x_{i+1} - 2x_i + x_{i-1}}{(\Delta s)^2} \right)^2 + \left(\frac{y_{i+1} - 2y_i + y_{i-1}}{(\Delta s)^2} \right)^2$$

Image term: This term aims to attract the dynamic contours toward the desired object's boundaries on the image. The features that attract the contour can be the edges,

lines, corners or any other point of interest. Below is an edge attraction term where the gradient of the intensity image I is computed at each contour point. Because of the negative sign, the energy is minimized near the edges of the image.

$$E_{image} = -\|\nabla I\|$$

Finally, we need to find the minimal energy state that is equivalent to solve the function: $\frac{\partial E}{\partial c} = 0$. The solution incorporates a mathematical iteration process to approach the minimal state:

$$c_{new} = c_{old} + \Delta t \frac{\partial E}{\partial c}$$

The corresponding discrete form is:

$$\begin{bmatrix} x_i \\ y_i \end{bmatrix}_{new} = \begin{bmatrix} x_i \\ y_i \end{bmatrix}_{old} + \Delta t \{ \begin{bmatrix} \frac{\partial \|\nabla I\|}{\partial x} \\ \frac{\partial \|\nabla I\|}{\partial y} \end{bmatrix} + \frac{2\alpha}{(\Delta s)^2} \begin{bmatrix} x_{i+1} - 2x_i + x_{i-1} \\ y_{i+1} - 2y_i + y_{i-1} \end{bmatrix} + \frac{2\beta}{(\Delta s)^4} \begin{bmatrix} x_{i-2} - 4x_{i-1} + 6x_i - 4x_{i+1} + x_{i+2} \\ y_{i-2} - 4y_{i-1} + 6y_i - 4y_{i+1} + y_{i+2} \end{bmatrix} \}$$

where Δt is the iteration step length.

3.3.3 Segmentation Operations

As the Snakes method needs an original contour from which to grow, an initial manual operation is needed, in which the operator should know the locations of interesting arterial lumens on the MR or re-sliced images. In the procedure, the operator

uses the left mouse button to pick points around the lumen and the right mouse button to pick the last point, and then a spline curve is used to connect these points automatically. The closer these initial points approximate the real boundary, the better the Snakes result will be. There is no particular limitation on the number of points – the choice depends on the complexity of the lumen. The original contour then begins to grow according to the Snakes algorithm. Finally, the contour approaches to the boundary of the lumen and the segmentation process is stopped.

Figure 3.4 shows an example that was used to illustrate and verify the reliability of the Snake program, where the boundary of the object (area with white color) is clear. Starting from any point that was near the boundary, the plus (+) symbol shows the points picked initially. The last point was picked near the first point using the right mouse button. Lines (green) automatically connected all the points to form the original contour for growing. The red points represent the traces of points of the contour as it grew, where they started from the original contour and went to the edge, finally approaching the desired boundary as the blue contour shows.

As emphasized previously, the ideal transverse section of an artery is the section that is perpendicular to the local axial direction of the artery. In such sections, the aortic lumen is always nearly circular. In a clinical scanning operation, the MRI slices are generally a group of parallel images and each slice has a certain thickness that will produce unavoidable confusion when the thickness is across a sharp bend in the lumen. Consider the image in Figure 3.5 (a). Here, a blurred boundary of the ascending aorta is presented by the original 28th MRI slice (see Figure 3.1) where the sharply curved wall just penetrates the 3 mm thickness of the slice. As the MRI scan is a projection image

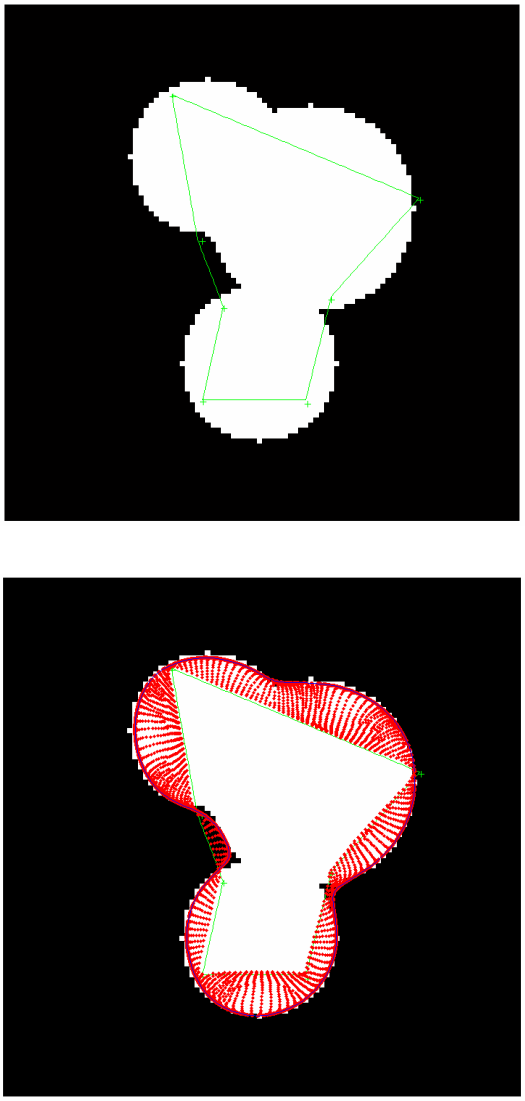

Figure 3.4: An example of processing using the Snakes segmentation for checking the reliability of the program.

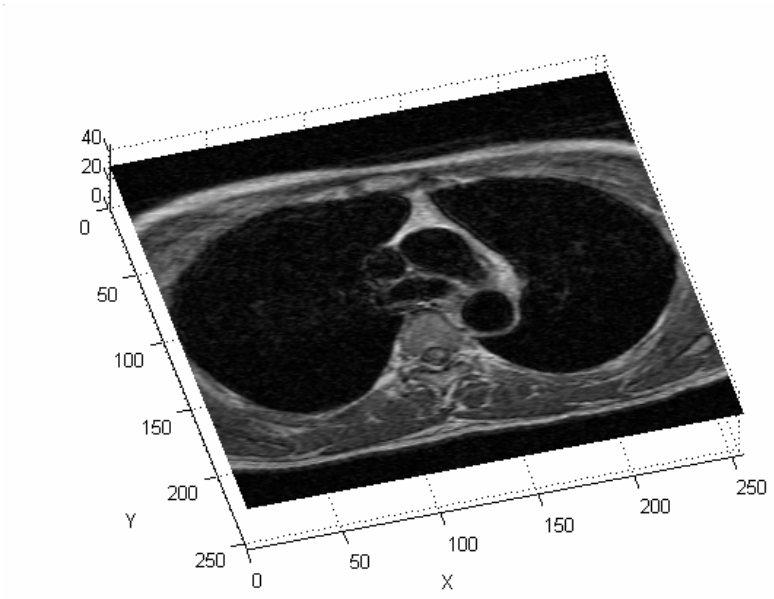

Figure 3.5 (a): Blurred boundary of the ascending aorta was presented by the 28th image in Figure 3.1 due to the thickness of the image that went across the curvature of the lumen.

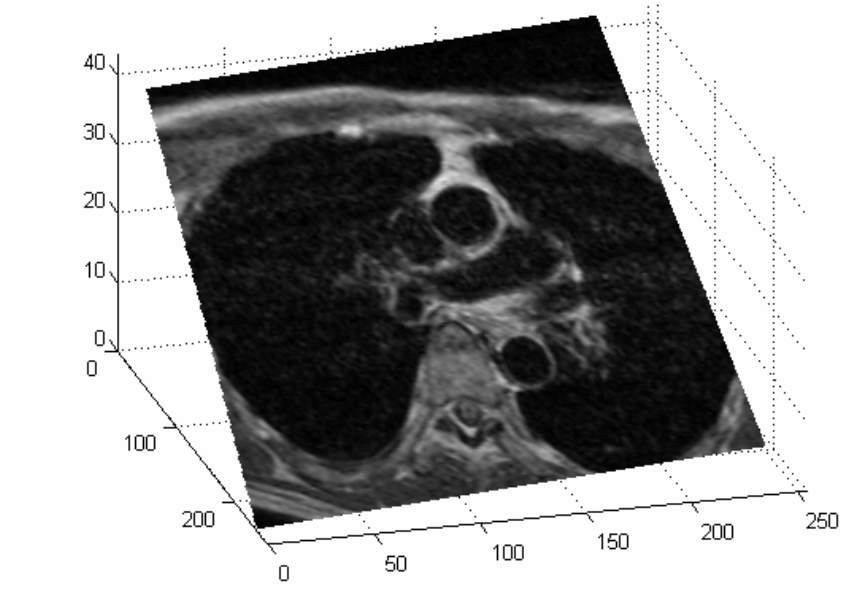

Figure 3.5 (b): A re-slice that was perpendicular to the local axial direction of the ascending aorta avoided the blurred boundary of the lumen as shown in Figure 3.5 (a).

across the slice thickness, any image intensity changes within the thickness will produce a blurred image. If a re-slicing is performed to be perpendicular across the same segment of the ascending aorta (See Figure 3.5 (b)), the blurred boundary can be avoided and a nearly circular lumen is represented, which is more suitable for the Snakes segmentation procedure.

Figure 3.6 (a) shows the Snakes result where the segmentation was performed on the re-sliced image (Figure 3.5 (b)), and the result was returned to the 3D data space simultaneously (see Figure 3.6 (b)), which was also the CFD model reconstruction space. Figure 3.7 shows more segmentation on re-sliced images from the original slicing space. How many re-sliced images are needed to represent an arterial lumen? This depends on the complexity of the artery and what hemodynamic factors are desired from the CFD simulations. For example, the number of re-slices required to reproduce flow patterns is less than that required to calculate wall shear stress accurately in the same model, because the latter needs a more precise representation of local wall surfaces.

After segmentation, all the results or contours were represented in the original 3D data space (see Figure 3.8). However, as seen by the highlighted red curves, neighboring contours may present an irregular oscillation of areas and centers in the space, especially in the root of the ascending aorta (see the lower image of Figure 3.8). The irregular contours made up a ragged arterial surface that would be inaccurate. The source of the spatial errors made by the contours was because the segmentations were only 2D individual operations and that was insufficient for an anatomically representative 3D model reconstruction.

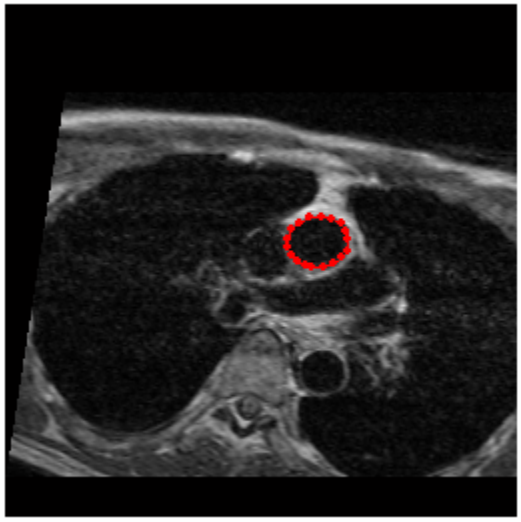

Figure 3.6 (a): Snakes segmentation of the lumen of the ascending aorta was performed on the re-sliced image, as shown in Figure 3.5 (b).

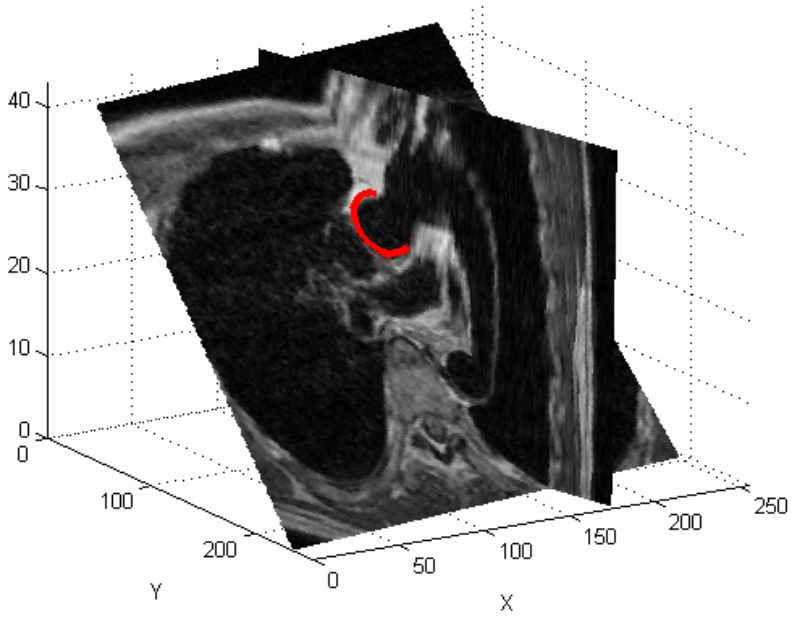

Figure 3.6 (b): The segmentation result, as shown in Figure 3.6 (a), was returned to the 3D data space.

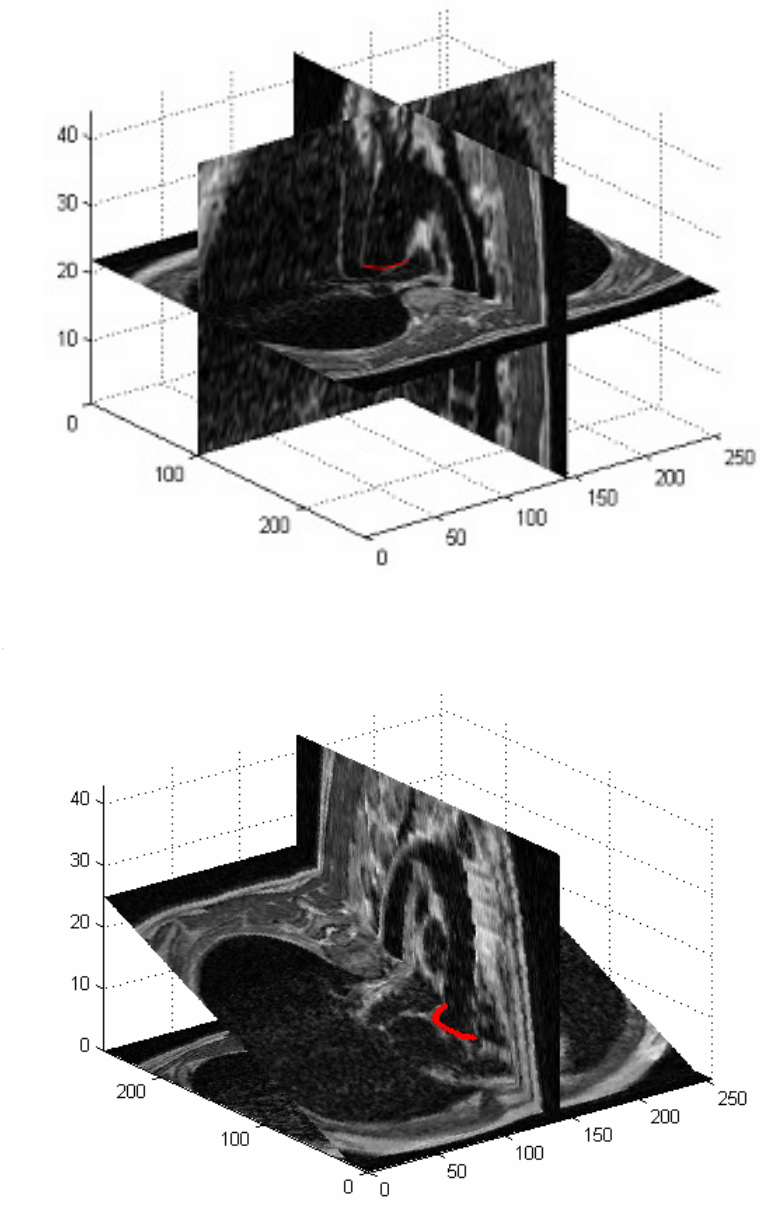

Figure 3.7: Additional segmentation results on the re-sliced images that were perpendicular to the local longitudinal directions of the lumen and represented nearly circular boundaries.

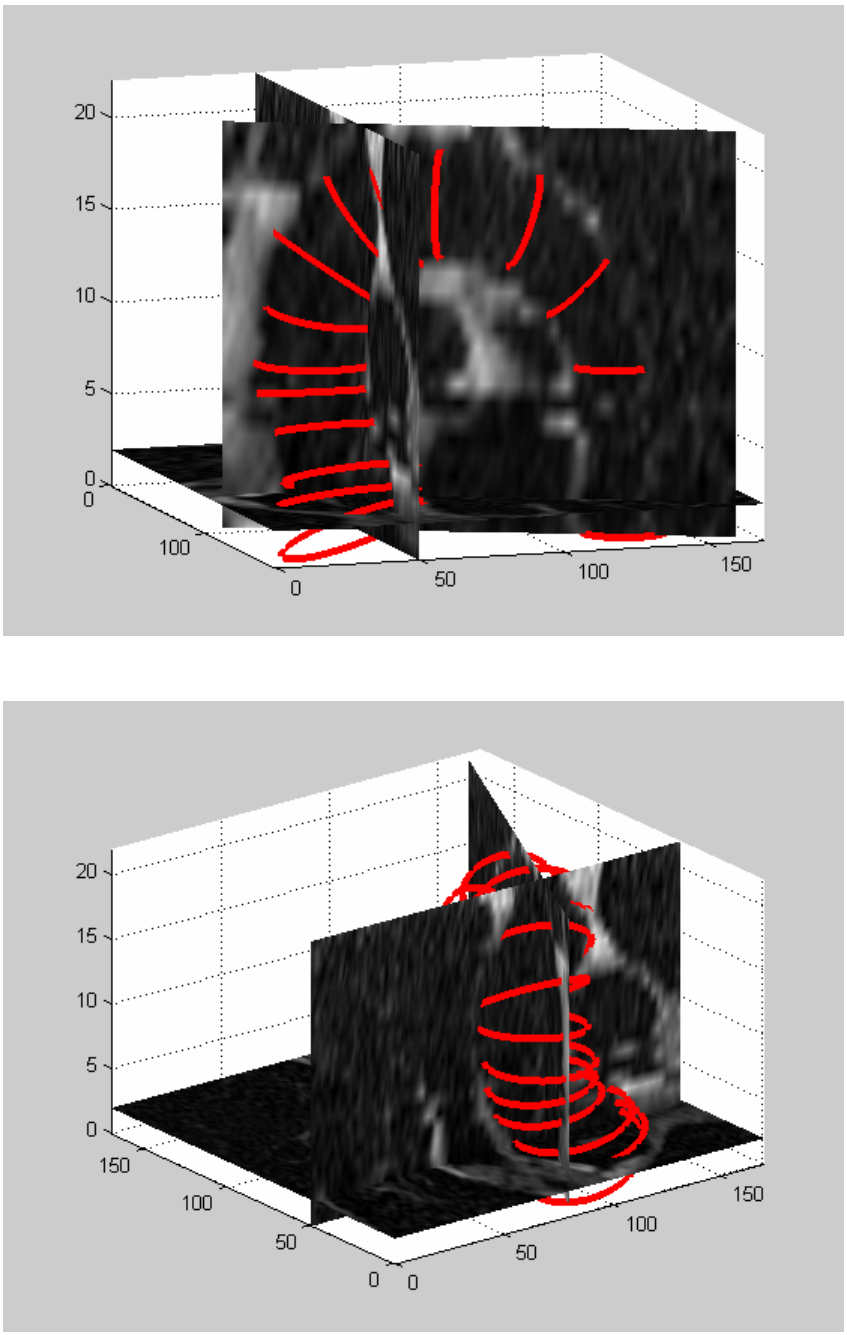

Figure 3.8: All the segmentation results, boundaries of the lumen, were returned to the original 3D data space. The local curvature of the lumen determines where and how many of the transverse re-slices are needed.

3.4 Reconstruction of the CFD Geometrical Model

A 3D geometrical model is composed of curves and surfaces. The contours that came from the MRI image segmentation could have too many errors to be directly used in the 3D model reconstruction as discussed in the previous chapter. Smoothing methods can help us to overcome these errors.

3.4.1. Smoothing

For 3D geometrical modeling, smoothing of the 3D imaging data produced by MRI slices is necessary because image processing on each isolated 2D image independently is inadequate for good continuity of the reconstructed 3D surface. As we did not involve any 3D information in the segmentation of 2D images, there were usually some discontinuities among the neighboring segmented contours when these contours returned to the original 3D space. These discontinuities would cause the surfaces that connect the contours to be jagged. Thus, these jags need to be filtered, and several smoothing methods of spatial surfaces can do this.

Woltring (1986) first introduced an available spline algorithm GCVSPL for space smoothing of contours. Moore (1998) considered this three-phase smoothing procedure to be very suitable for vascular modeling from MRI slices. The method is divided into three steps:

- The first step is to smooth the contours individually on each 2D image plane using quintic splines. After the smoothing, the geometrical center point and the area of each contour are calculated. These centers form a sequence of points in space, and the associated areas form a series of numbers.

- In the second step, a space cubic spline is used to smooth the 3D broken line that penetrates the sequential center points. The smoothing process updates the position of each point, and at the same time, the position of the corresponding contour is also updated.
- Finally, a cubic spline is used to smooth the serial values of the areas. The smoothing process updates the values of the areas, and the corresponding contours are expanded or contracted according to the updated areas. The processing keeps the shape of the contour unchanged while its area is updated.

The three steps can be used repeatedly depending on whether a smooth surface is formed by the final sequential contours.

In this study, the three-phase smoothing procedure was repeated twice in the 3D model reconstruction. Figure 3.9 (b) shows the contours after the smoothing procedure. Comparing with the original results of segmentation in Figure 3.9 (a), the smoothed contours are more nearly circular. Some irregular contours were deleted manually if they interfered with the smoothness of the total surface. A justification for deleting these contours is that they create local effects of bulges or concavities in the final surface. The judgment used in deleting irregular contours was based on the complexity of the local surfaces.

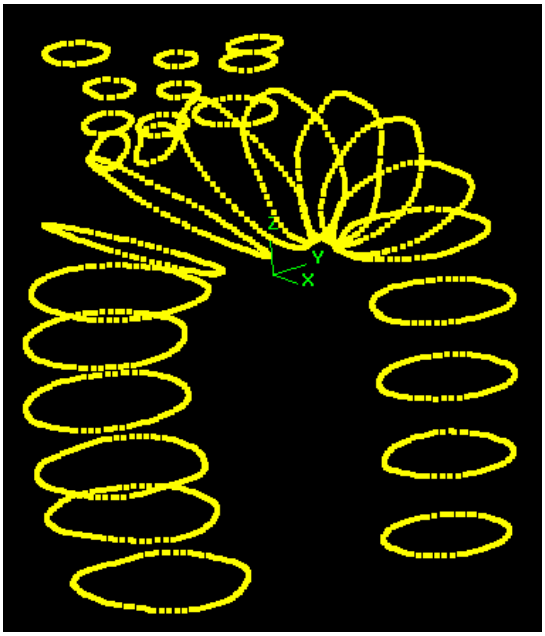

Figure 3.9 (a): The sequential contours before the smoothing process.

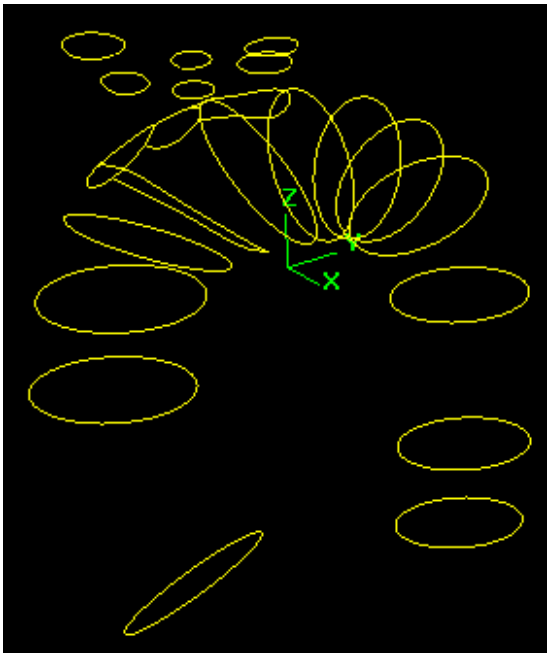

Figure 3.9 (b): The sequential contours after the smoothing process.

3.4.2. NURBS Curves and Surfaces

The Non-uniform rational B-Spline (NURBS) curve and surface is a classical parametric smooth curve and surface that is commonly used in 3D geometrical model reconstruction (Piegel and Tiller, 1997). NURBS is the generalization of non-rational B-splines which are based on rational Bézier curves.

A Bézier curve of degree *n* is defined by

$$C(s) = \sum_{i=0}^{n} R_{i,p}(s) P_i \qquad 0 < s < 1$$

where $R_{i,p}$ are rational basis functions of degree p and P_i are the n+1 nodes of the associated control polygon.

The rational basis functions are generalized from B-spline curve functions and are defined as

$$R_{i,p}(s) = \frac{N_{i,p}(s) w_i}{\sum_{j=0}^{n} N_{j,p}(s) w_j}$$

where w_i are the weights; $N_{i,p}$, i = 0, …, n, are the B-spline basis functions of order p; and s is the breakpoint of the B-spline.

The B-spline basis function is defined as

$$N_{i,0}(s) = \begin{cases} 1 & \text{if } s_i \le s \le s_{i+1} \\ 0 & \text{otherwise} \end{cases}$$

$$N_{i,p} = \frac{s - s_i}{s_{i+p} - s_i} N_{i,p-1}(s) + \frac{s_{i+p+1} - s}{s_{i+p+1} - s_{i+1}} N_{i+1,p-1}(s)$$

where s_i are the sequence of breakpoints.

In the present study, the production of NURBS curves or surfaces was accomplished by CFD-GEOM software automatically. However, control points in the space must be designed for the production of NURBS curves, and curves must be selected for the production of NURBS surfaces. NURBS surfaces have two important properties that led to selecting them for CFD geometrical modeling:

- Continuity: a NURBS curve can be many times continuously differentiable on the breakpoints. This is necessary for keeping C^2 continuity among the contact faces that cover over the 3D model for CFD mesh generation.
- Local support: NURBS can limit the surface deformation locally, which means that by moving a point that makes up the surface mesh, the shape of the smooth surface is changed only within a bounded region around the point. For other curves and surfaces that do not have this property, for example, moving a point from sequential points that are connected by a polynomial curve will change the total shape of the curve. That was also why some irregular contours could be deleted without greatly changing the shape of the surface in the smoothing procedure described previously.

The second property of a NURBS surface is very useful in the model reconstruction using the CFD/MRI method. Figure 3.10 shows an example, in which sequential contours of an aorta resulting from a processed image are shown in the left of Figure 3.10 (a), and

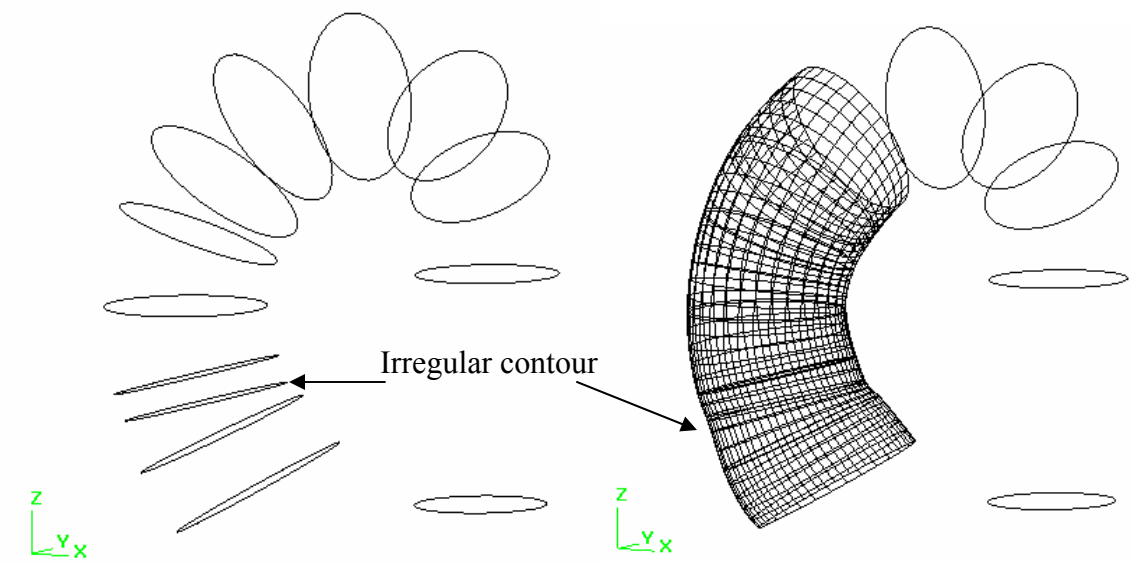

Figure 3.10 (a): An irregular contour caused the NURBS surface to undulate in local region.

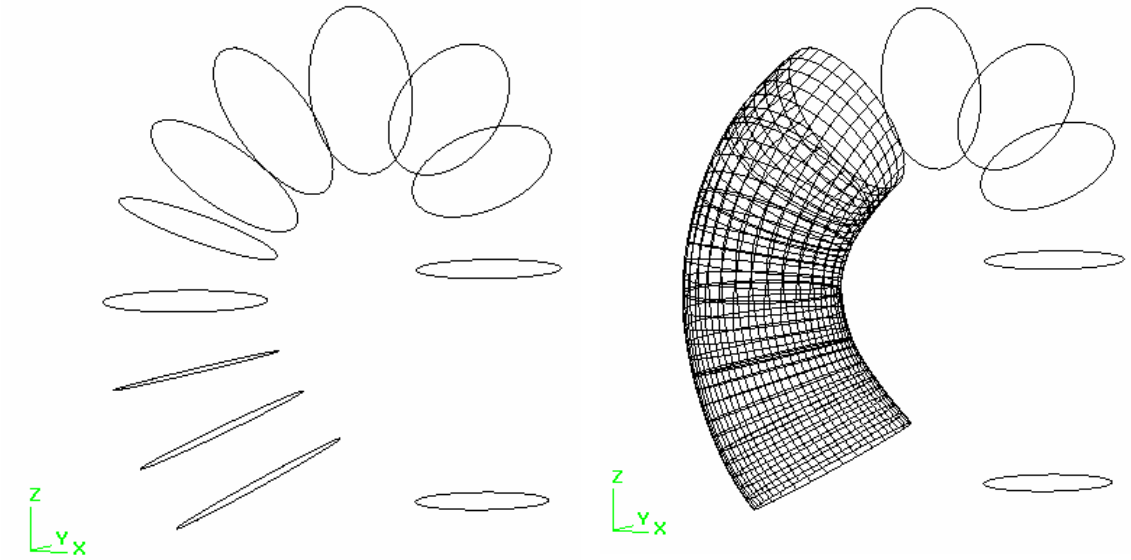

Figure 3.10 (b): After the irregular contour was deleted, the local surface became smooth but the whole surface did not change significantly.

an irregular contour located in the ascending aorta can be found. A NURBS surface was set up through the sequential contours, and the right picture of Figure 3.10 (a) shows the surface mesh where the irregular contour caused the surface to undulate locally. If the irregular contour is deleted, as the left picture of Figure 3.10 (b) shows, the local surface becomes smoother (see the right picture of Figure 3.10 (b)), but the entire surface is changed very little (compare with the original surface in the right picture of Figure 3.10 (a)).

Figure 3.11 (a) shows an entire transitional NURBS mesh over the sequential contours during the process of repeated smoothing. The mesh was set up based on the contours that were shown in Figure 3.9 (b), and the contours can then be updated according to the surface mesh results. Repeated processing continues until a satisfactory surface appears. Figure 3.11 (b) shows the final NURBS surface that makes up the geometrical model of the aorta, from which a CFD grid mesh will be created on the surface.

3.4.3 Model Reconstruction of the Aorta

The geometrical models of the three vessels branching from the aorta arch were constructed and smoothed using the three-step smoothing method described previously. Figure 3.12 (a) shows the surfaces of the arch vessels. The smaller sizes of these arteries in the images, which were obtained with same absolute resolution as the image of the aorta, resulted in branch surfaces that have lower resolution than the aorta itself. Fortunately, in this study we only care about the total flow in the branches but not the velocity distributions, so that the relatively lower resolution was not a problem for the simulation of flow in the ascending aorta. The assembled geometries of the branches and

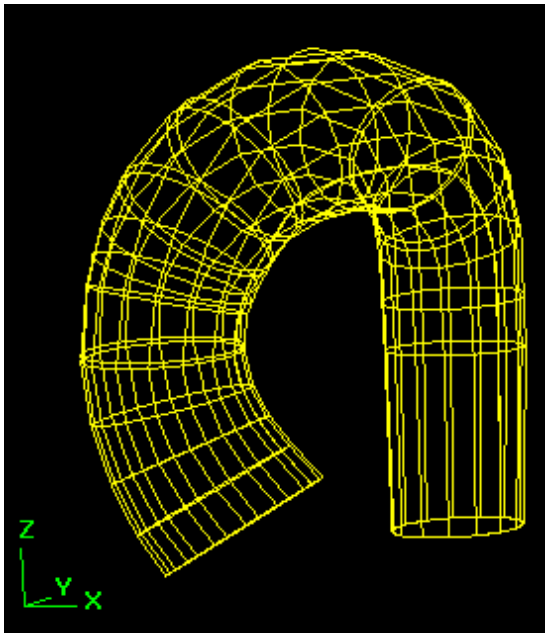

Figure 3.11 (a): A transitional NURBS mesh that goes through sequential contours

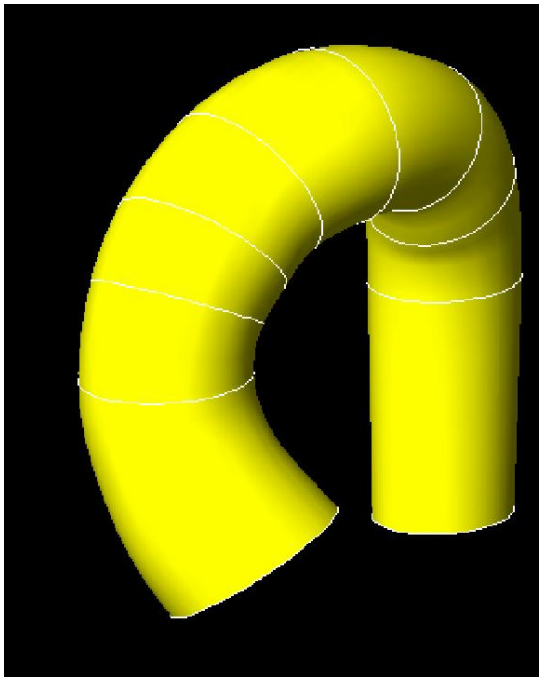

Figure 3.11 (b): The final NURBS surface that forms the surface of the aorta model.

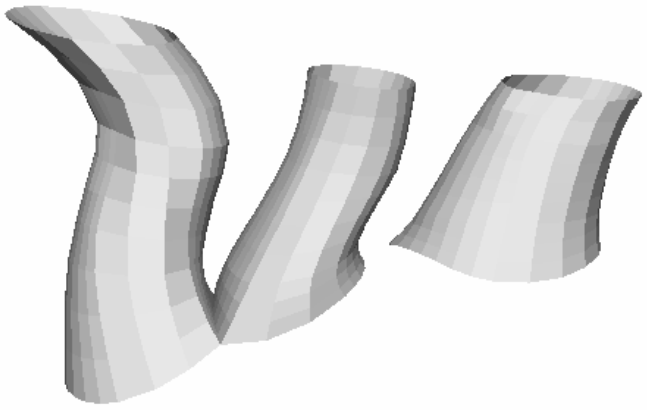

Figure 3.12 (a): The surfaces of the branches in the aortic arch.

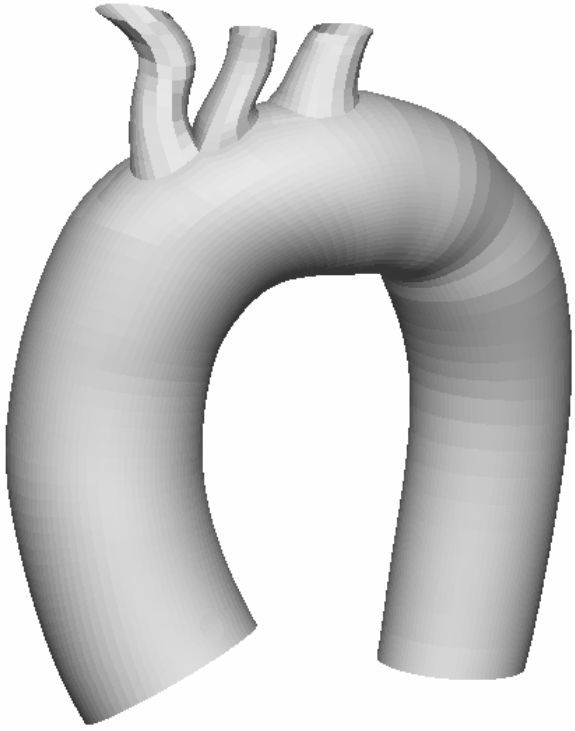

Figure 3.12 (b): The total surfaces of the aorta model.

aorta were completed using CFD-GEOM software. Figure 3.12 (b) shows the final surfaces of the computational model.

Mesh generation for a given face of a computational element is an interpolation process among the curves that comprise it, and mesh generation for a given volume is also an interpolation among known boundary faces that form a domain. The mesh generation was performed using CFD-GEOM software; however, the numbers and distributions of the grids of the mesh in every curve and face must be determined before using the software. These depend on the local geometrical characteristics of the CFD model and the convergence of the numerical solution of the Navier-Stokes equations. Experience gained in the computational studies guides choices for the mesh generation. Figure 3.13 shows the CFD model of the aorta that was employed in this study.

Four models of the aorta were constructed in the investigation. All of them were developed from healthy volunteers *in vivo* using the same anatomical positions and MRI scanning parameters. All models were constructed using the same image processing, smoothing methods and kinds of curves and surfaces as described previously. Because a unique methodology was employed in the construction of the four computational models, only one was selected as an example to illustrate the construction process. The other three CFD models are shown in Figure 3.14 but are not discussed here.

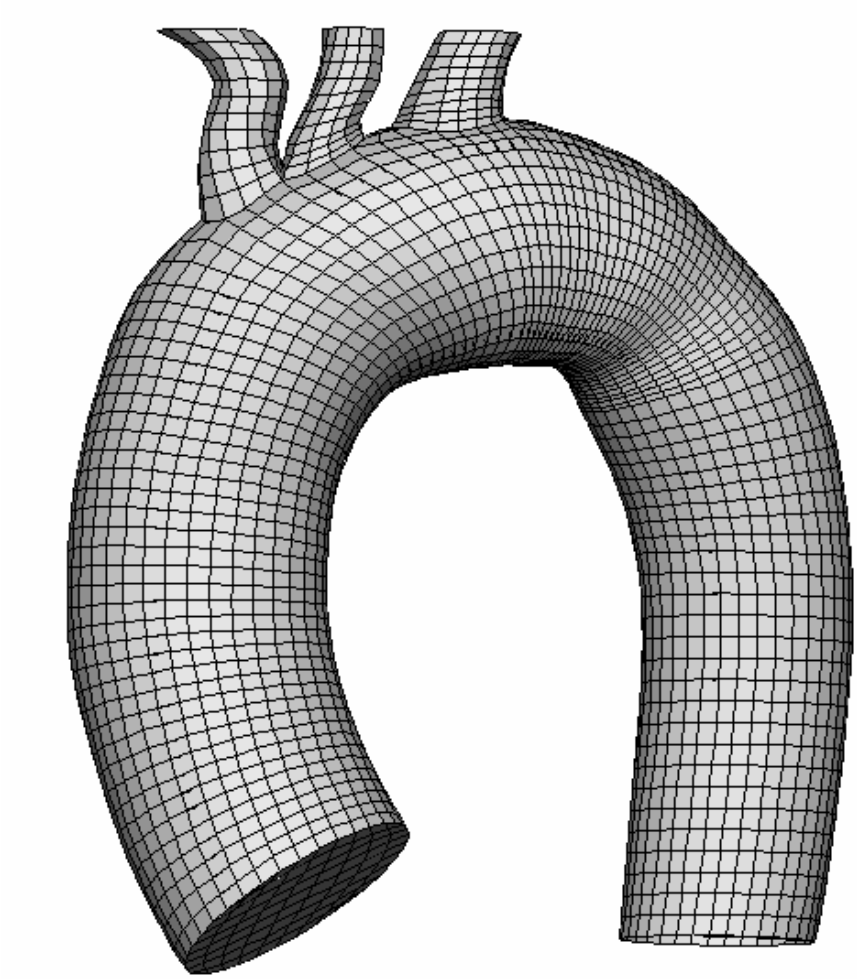

Figure 3.13: The mesh and CFD model of the aorta.

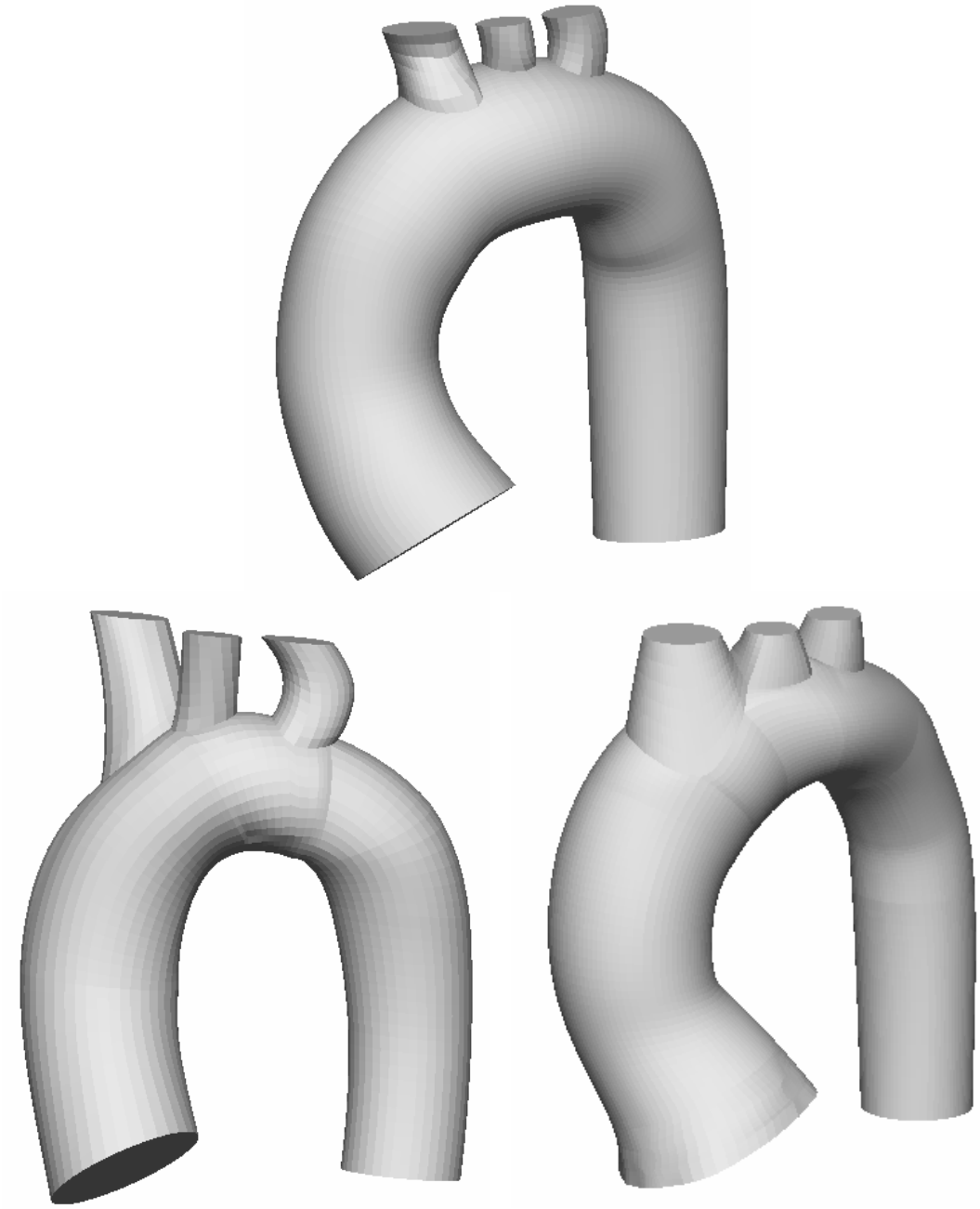

Figure 3.14: Three aorta models that were reconstructed from three healthy volunteers using the same methodology.

3.4.4 Model Reconstruction of the Coronary Arteries

The model reconstruction of the coronary arteries is different from that of the aorta, as the size of the coronary arteries is too small to obtain highly resolved MRI images. The top image of Figure 3.15 shows the frontal section of the right coronary artery where a transverse MRI slice has been scanned (the yellow line). The middle image of Figure 3.15 shows the slice where the field of view is 200 × 200 mm; image resolution is 512 × 512 pixels and the slice thickness is 8 mm. Although the lumen of the right coronary artery spans a few pixels on the image, as the zoom in image shows (see the lowest image of Figure 3.15), the ratio of the signal to noise at this level was too small to show a clear boundary of the lumen.

To address this problem we assumed that the boundary of the lumen of the coronary arteries is circular if the MRI slice is perpendicular to the local longitudinal direction of the artery. This is a reasonable assumption, since the arteries are under an intramural pressure. With this constraint, a deformable circle can be used to approximately match the arterial lumen on the image (see the red circle in the lowest image of Figure 3.15), even though the thickness of the slice produced a blurred boundary of the lumen. After an MRI scan was performed over the proximal segments of the coronary arteries, the idealized lumens on the slices were ellipses because the slices were not exactly perpendicular to the local longitudinal directions. In this case, the circles that were used to match the lumens were controlled to have the same diameters as the major axis of the ellipses. Sequential circles and their centers were obtained from the slices. The spatial coordinates of the centers were determined, and then the centers were connected by a smooth spatial curve (see the two curves in upper image of Figure 3.15) in 3D space.

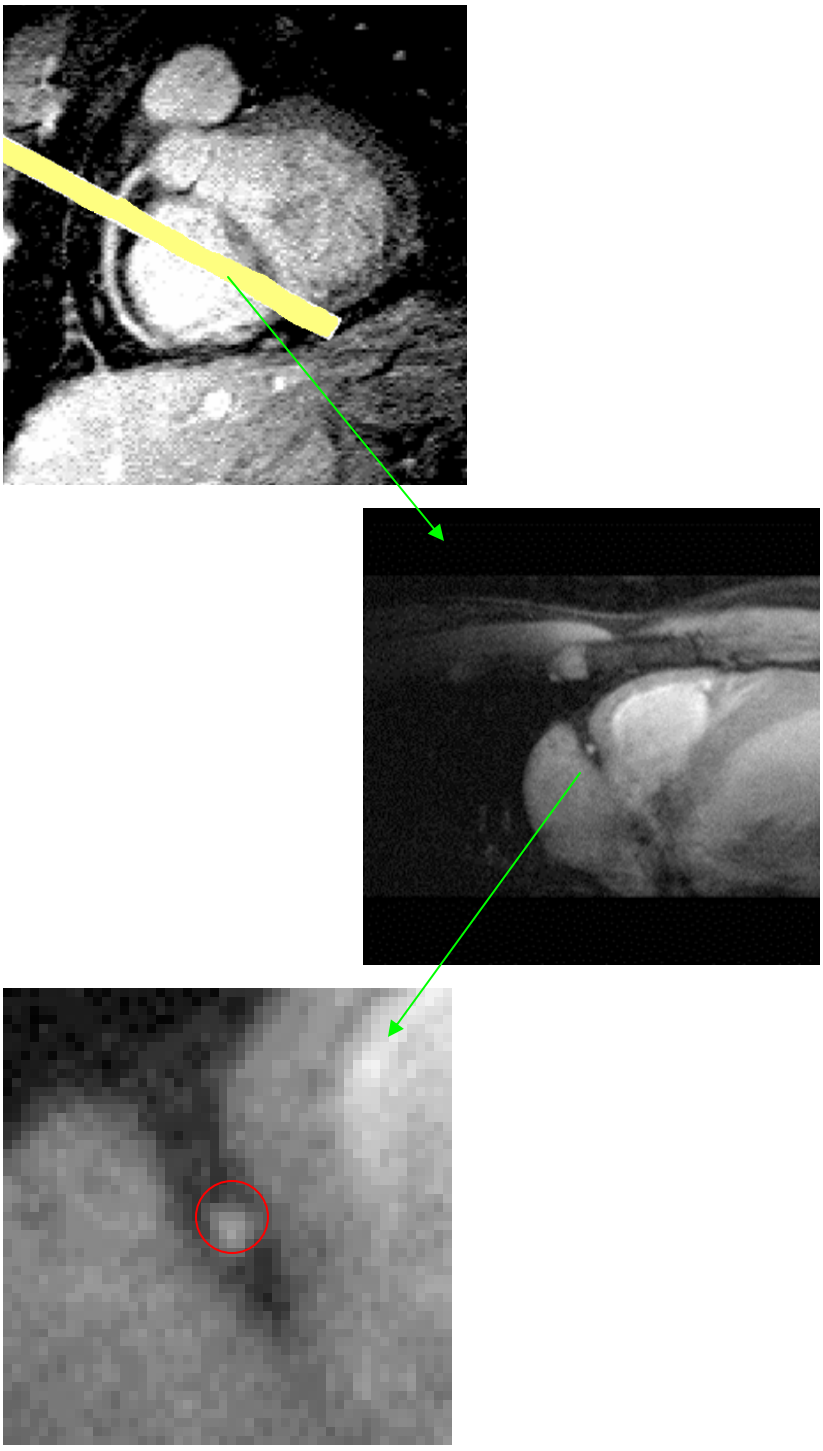

Figure 3.15: MRI scanning across the right coronary artery; the middle image shows the section of the slice and the low image shows the zoom-in lumen of the right coronary artery.

Each circle was reproduced around its center on a plane that was orientated normal to the local tangential direction of the curve and passing through the center point.

Sequential circles produced by the above method formed the skeleton of the coronary arteries (see the upper image of Figure 3.16). NURBS surfaces were used to cover the skeleton, and smooth models of the right and left coronary arteries were produced (see the lower image of Figure 3.16).

The blood flow simulation in the coronary arterial models and in the aortic models was performed simultaneously. As discussed in Chapter 1, blood flow in the coronary arteries is expected to be affected by the flow in the aorta root, especially the flow patterns in the proximal segments of the coronary arteries. Thus, flow modeling in the major trunks of the coronary arteries cannot be isolated from the aorta. However, the big difference in geometrical size and flow conditions between the aorta and coronary arteries makes it undesirable, from the standpoint of optimum MRI parameters, to scan both vessels simultaneously; so we elected to scan the aorta and coronary arteries separately and to reconstruct their geometrical models before assembling them into a united configuration.

The most difficult operation in assembling separate models of the aorta and coronary arteries is how to determine the relative orientation of the coronary arteries to the aorta root in 3D space. Two ways to find the locations of the coronary arteries were used in the study. The first was to control the aorta transverse slices so as to penetrate the major trunks of the coronary arteries in the MRI scans in such a way that the joined regions of the coronary arteries could be distinguished from the slices. Figure 3.17 (a) shows such an image where the orientation of the left coronary artery relative to the aortic root is

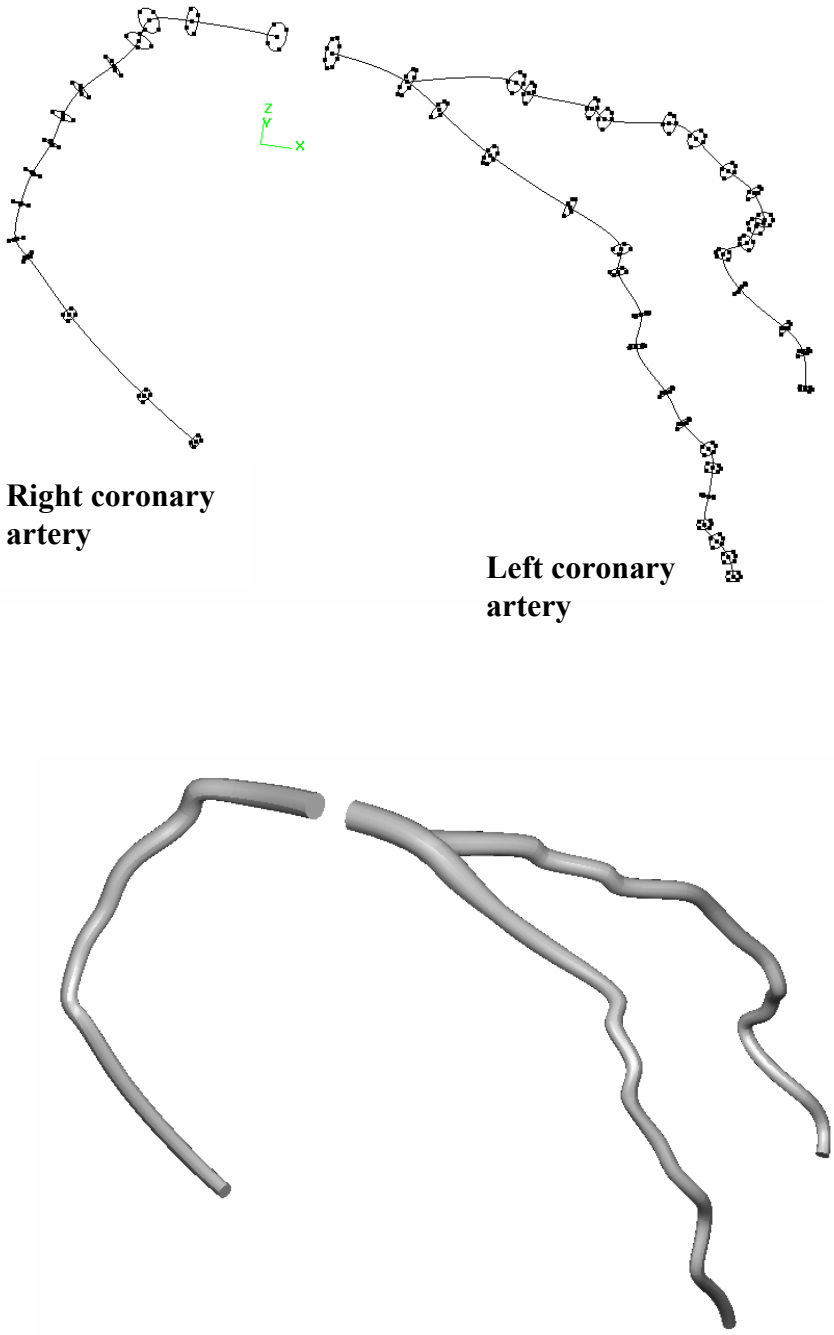

Figure 3.16: Reconstruction of the right and left coronary arteries; the upper shows the skeletons of the coronary arteries and the lower shows the models covered by NURBS surfaces.

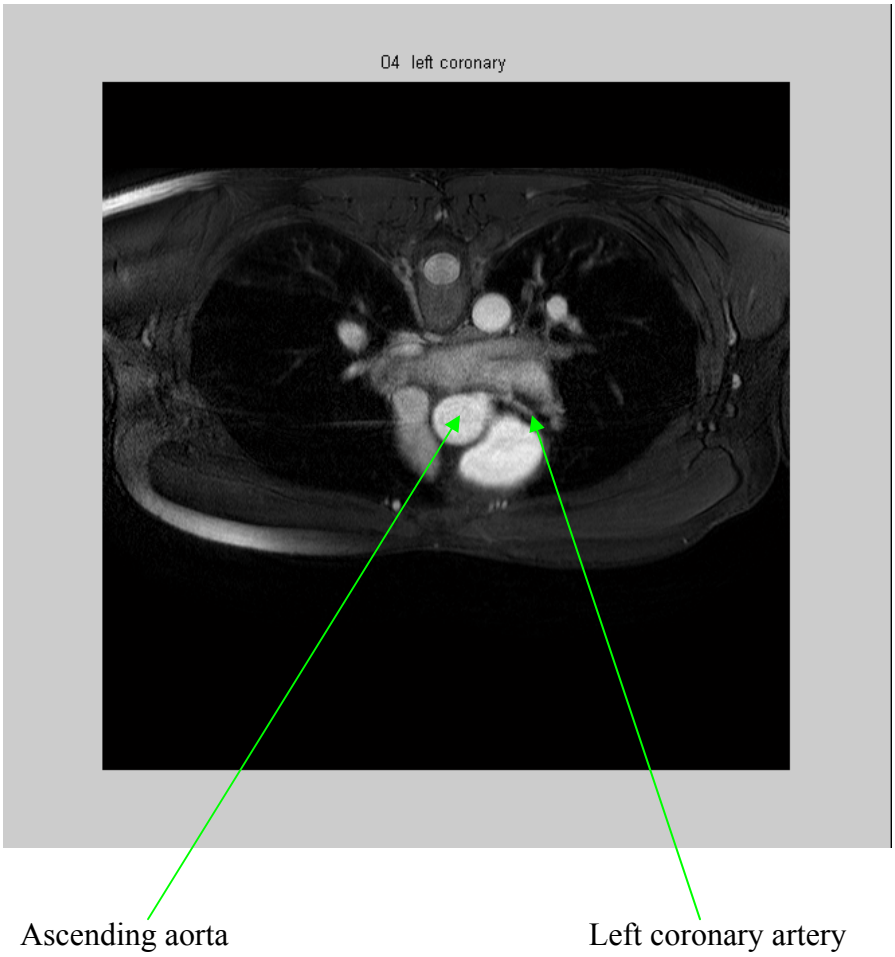

Figure 3.17 (a): The MR slice clearly shows the aortic root and left coronary artery.

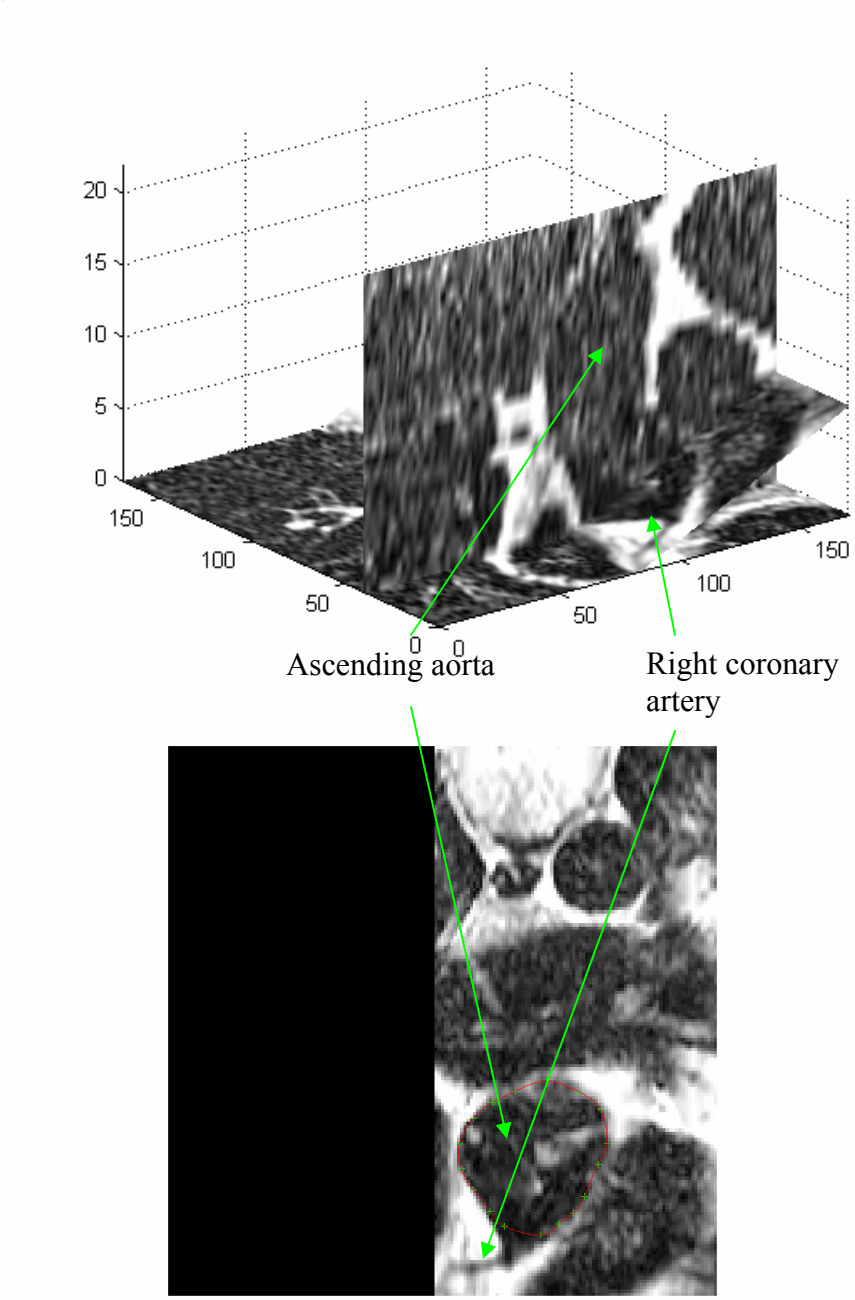

Figure 3.17 (b): The re-slices of the ascending aorta represent the orientation of the right coronary artery.

obvious. The second was to use a re-slicing technique in the 3D image data to find the joined regions. Figure 3.17 (b) shows an example where the re-sliced image indicates the exact 3D orientation of the right coronary artery.

Our numerical studies showed that slight deviations of the orientation of the coronary arteries relative to the aorta are not problematic for reproducing flow patterns in the coronary arteries. Deviations in assembling the two vessels were unavoidable in some cases, for example, the in-plane orientation of the main trunk of the left coronary artery could be determined from the image (see Figure 3.17 (a)) but the orientation in the vertical direction, perpendicular to the plane, was uncertain and depended on the thickness of the slice. The exact angle between the aorta and the coronary artery in the vertical direction is difficult to determine if the thickness of the transverse slice is greater than the diameter of the left coronary artery. Fortunately, the experiments with CFD modeling illustrated that the effects of such a slight confusion caused by the slice thickness upon the calculations of entrance flow patterns in the coronary arteries was small.

Given these assumptions, Figure 3.18 shows the combined model of the coronary arteries and aorta that was used for the CFD simulations.

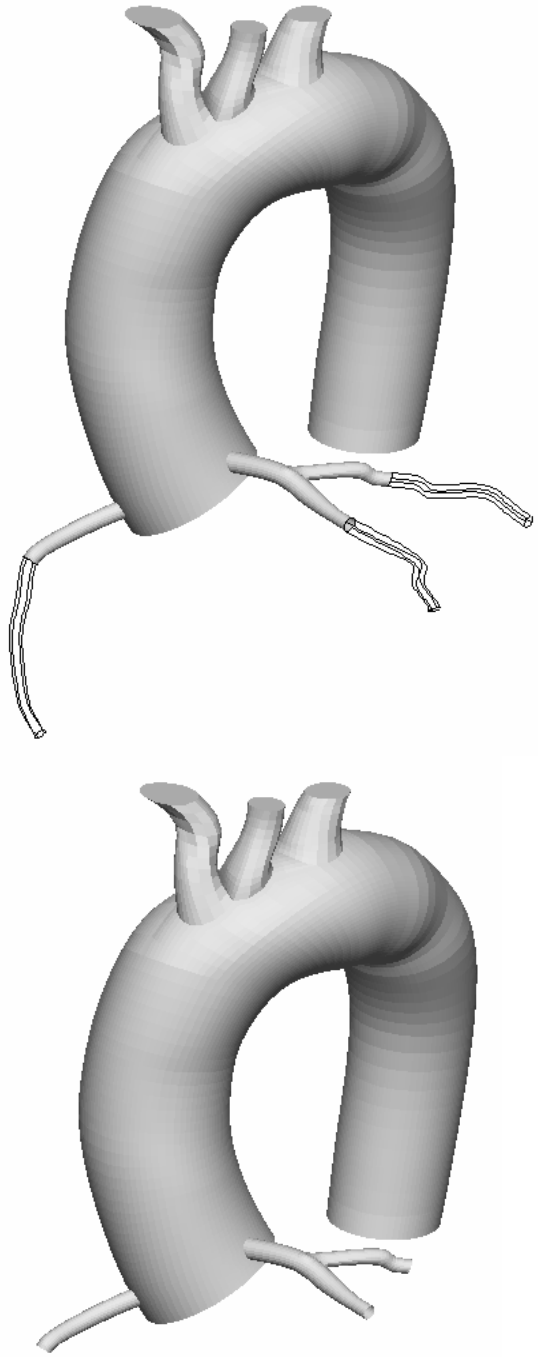

Figure 3.18 Combined CFD models of the aorta and coronary arteries. Due to limits in the blood velocity information, only the proximal segments of the coronary arteries are considered in the CFD flow computations.

3.5 Phase Contrast MRI and Flow Velocity Information

After the reconstruction of a realistic geometrical aorta model, velocity boundary conditions for the CFD simulation become essential. We have discussed two techniques that can measure the blood flow velocities *in vivo* in Chapter 3.1, and only the PC-MRI method can present the velocity distribution on a section of arterial lumen. To reproduce realistic blood flow patterns in an aorta using CFD modeling, the boundary conditions should come from measurements *in vivo*, and velocity distributions obtained by PC-MRI on the inlet and outlet sections are the best boundary conditions for the modeling.

3.5.1 Phase Contrast MRI

There are two MRI techniques to measure blood flow velocity *in vivo*: Phase contrast (PC) MRI and Time-of-flight MRI. We selected the former in this research because PC-MRI avoids magnetization saturation and it is possible to interrogate for specific velocity ranges as well as for the direction of velocity. The PC-MRI technique is not affected by the T1 of the tissues, unlike time-of-flight method. The 2-D PC-MRI technique capitalizes on a flow gradient obtained on gradient echo sequences, so high in-plane resolution is easily obtainable, although the high resolution is only in the plane of the section. To obtain 3D velocity information in a section, 2-D PC-MRI scanning should be done three times in the section because in each scan only one direction of the flow gradient is obtained. Three orthogonal components of the velocity in the section are scanned individually, even though this operation prolongs the scanning time.

In the present study, PC-MRI scanning was performed at three sections in the aorta, as Figure 3.19 shows, where these sections were perpendicular to the local aortic

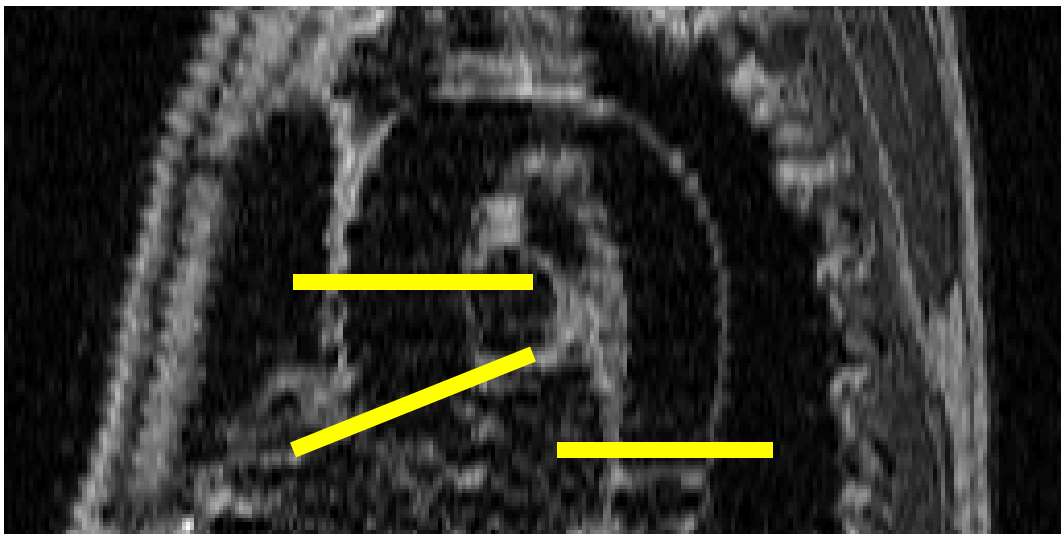

Figure 3.19: PC-MRI scanning was performed at three sections (yellow lines) in the aorta where the left lumen is the ascending aorta and the right lumen is the descending aorta.

longitudinal directions and were acquired immediately after the MRI geometrical imaging sequence. The first section, the inlet section, was located at the aorta root, and gave the inlet velocity conditions for CFD modeling. Another section crossed the descending aorta where the outlet section of the model was located. The remaining section was approximately midway in the ascending aorta, and it was employed as a "test section" for validation of the computational results, i.e., if the simulation is accurate, CFD would present the same velocity distribution as the PC-MRI results at that section.

PC-MRI scanning for each section and each velocity component generated 20 images (field of view, 300 × 300 mm; image resolution, 256 × 256 pixels; slice thickness, 6 mm). The 20 time-resolved images were taken at about 57 milliseconds time intervals to cover one cardiac cycle. The inlet section slices allowed measurement of three orthogonal velocity components. Since the length-diameter ratio of the ascending aorta is relatively small and the flow near the aortic valve is three-dimensional, the complex inlet flow might dominate the flow patterns in the ascending aorta. Figure 3.20 shows some images of the PC-MRI slices of the axial velocity component on the section, which included a pair images at each time. The first one of each pair is a signal modulus image that was used to segment the lumen, and the second is a signal phase image that presented the axial velocity magnitude. The number at the top of each image is the time when the image was taken, as referenced from electrocardiogram (ECG) monitoring. There are three groups of such slices, as the Figure 3.20 shows, in the inlet section. The other two groups of slices present the orthogonal velocity components on the plane.

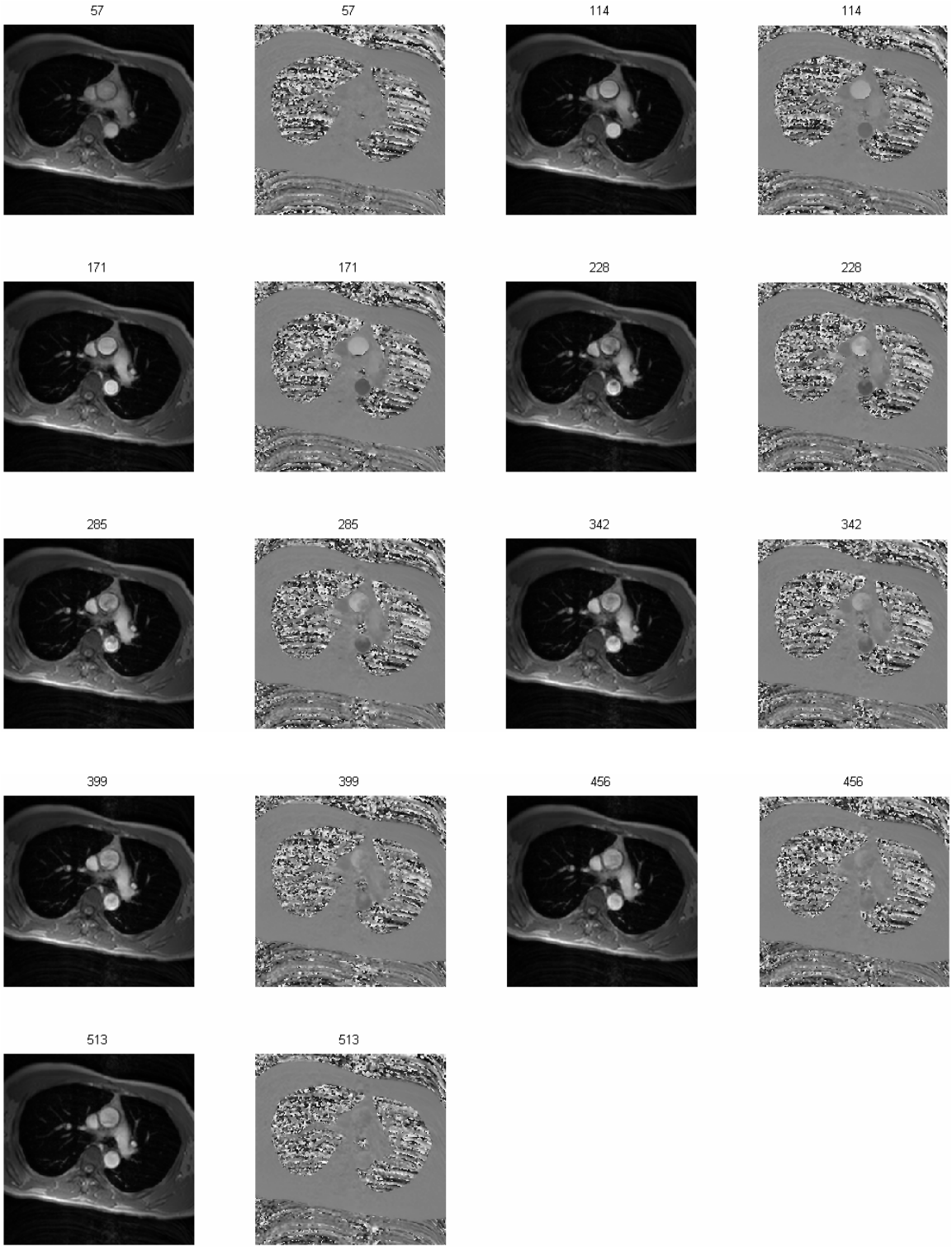

Figure 3.20: PC-MRI slices for the axial velocity component in the inlet section - field of view, 300 × 300 mm; image resolution, 256 × 256 pixels; slice thickness, 6 mm. The slices include 20 images to cover one cardiac cycle.

At the outlet section of the descending aorta, the PC-MRI only measured the axial velocity component. We elected to ignore the two in-plane velocity components due to two reasons: first, the section is located far away from the ascending aorta and the aortic arch, so the axial flow is expected to be dominant there, and also our interest was in the ascending aorta; second, to include the two in-plane velocity components would have added significantly to the scanning time the subject would have been in the magnet, resulting in subject discomfort.

3.5.2 Blood Velocity Distribution in the Aorta in Vivo

Similar image segmentation was performed in the PC-MRI slices as described for the MRI slices. Aorta lumens were segmented by the Snakes program on each signal modulus image at different times (see Figure 3.20), and then the corresponding lumen on the phase image at the same time was isolated. The segmentation must be done in all slices because the aorta is moving during the cardiac cycle, and the position of the lumen is unsteady in the PC-MRI slices. The velocity magnitude in each pixel of the lumen on a phase image was calculated, and all the velocity magnitudes represented a velocity distribution of one velocity component at a time in the cardiac cycle. As there are three velocity distributions arising from the three orthogonal velocity components at each time on the inlet section, the three velocity components in each pixel of the lumen were combined to form a 3D velocity vector, and then all the vectors made up the 3D velocity distribution in the inlet section at that time. The upper pictures of Figure 3.21 show the distributions of the 3D velocity vectors at several representative times. As the three velocity components came from three images that were scanned independently although

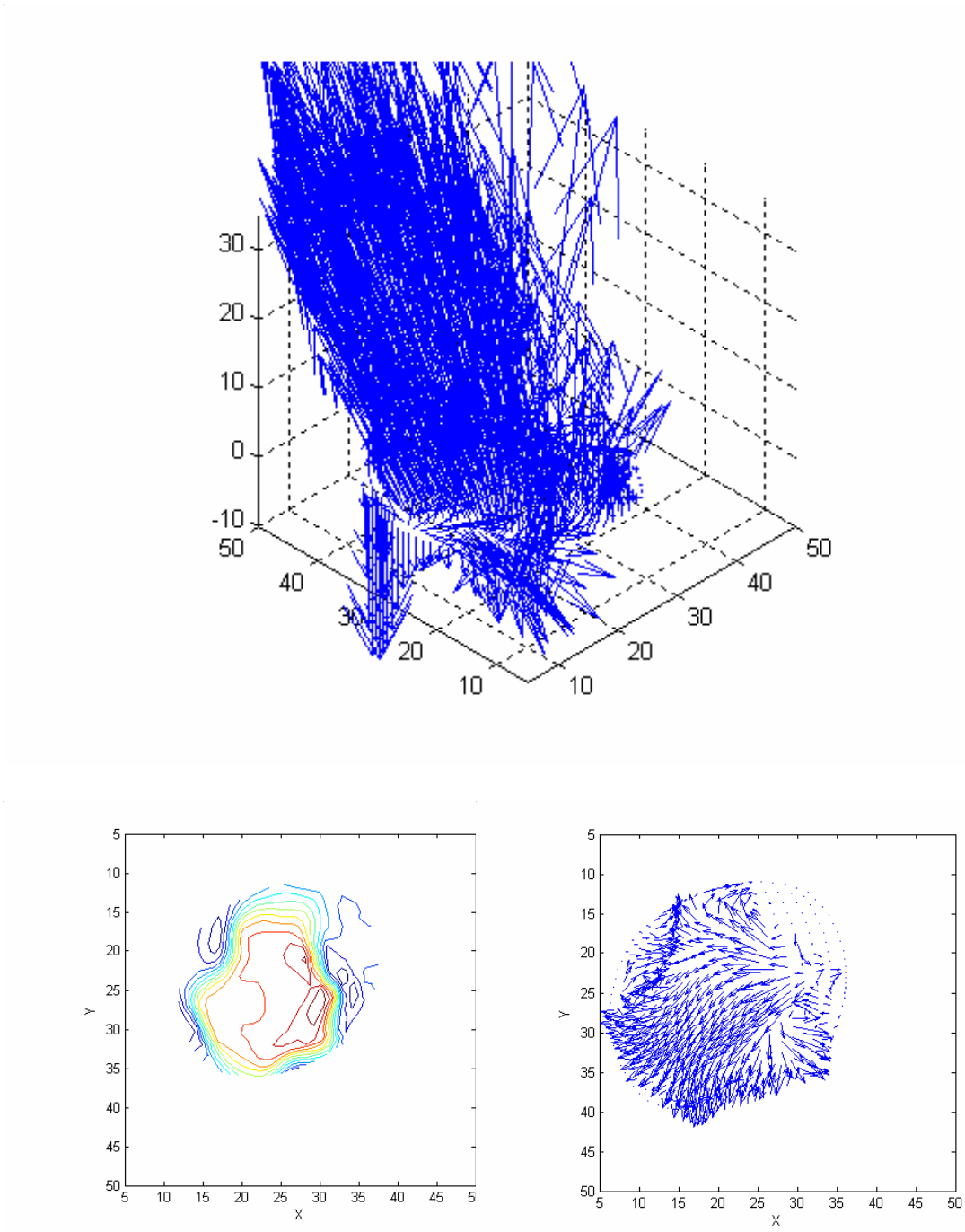

Figure 3.21 (a): The flow patterns come from PC-MRI scanning on the inlet section at 226 ms (indicated by the left arrow in Figure 3.17 (a)).

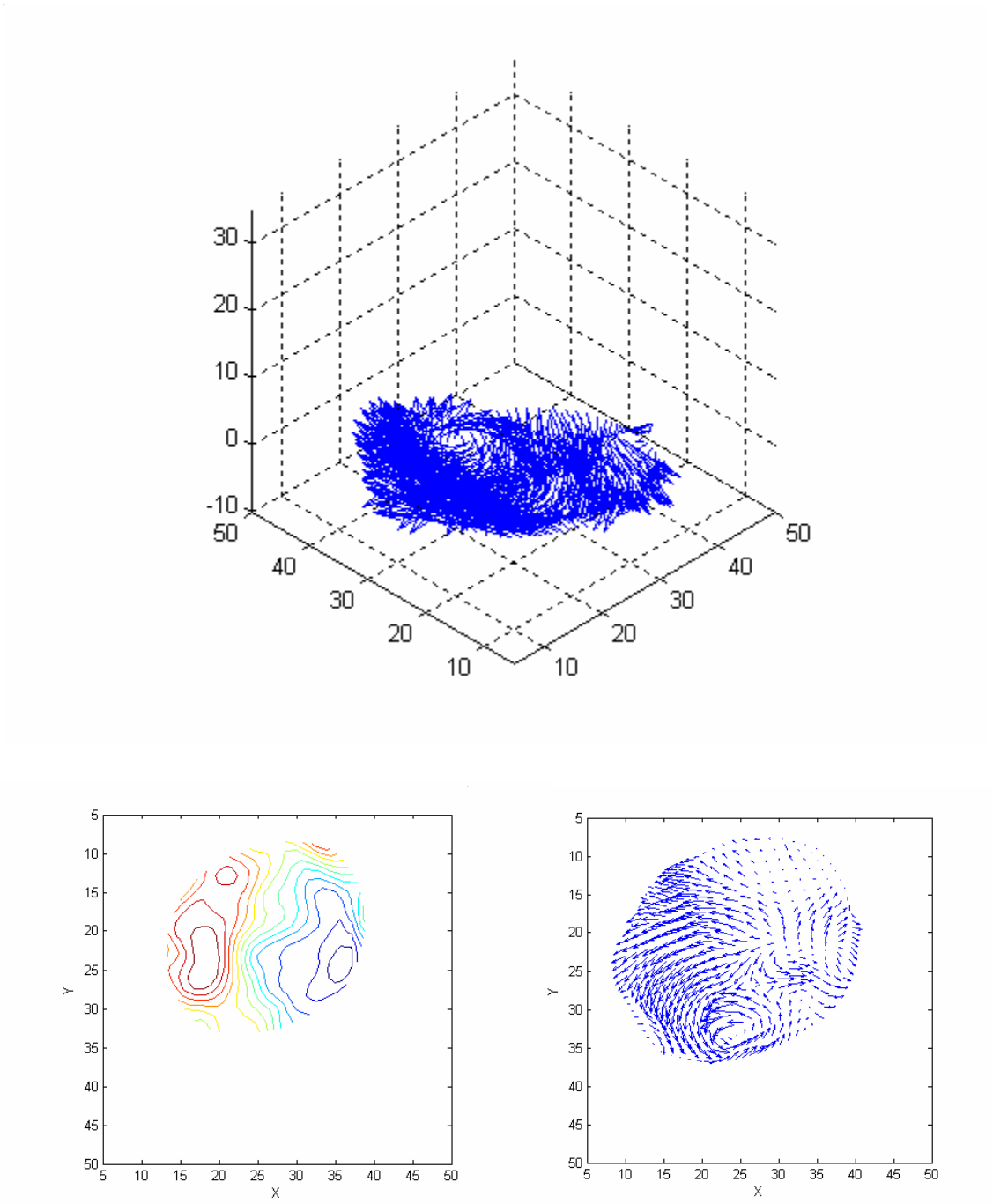

Figure 3.21 (b): The flow patterns come from PC-MRI scanning on the inlet section at 352 ms (indicated by the middle arrow in Figure 3.17 (a)).

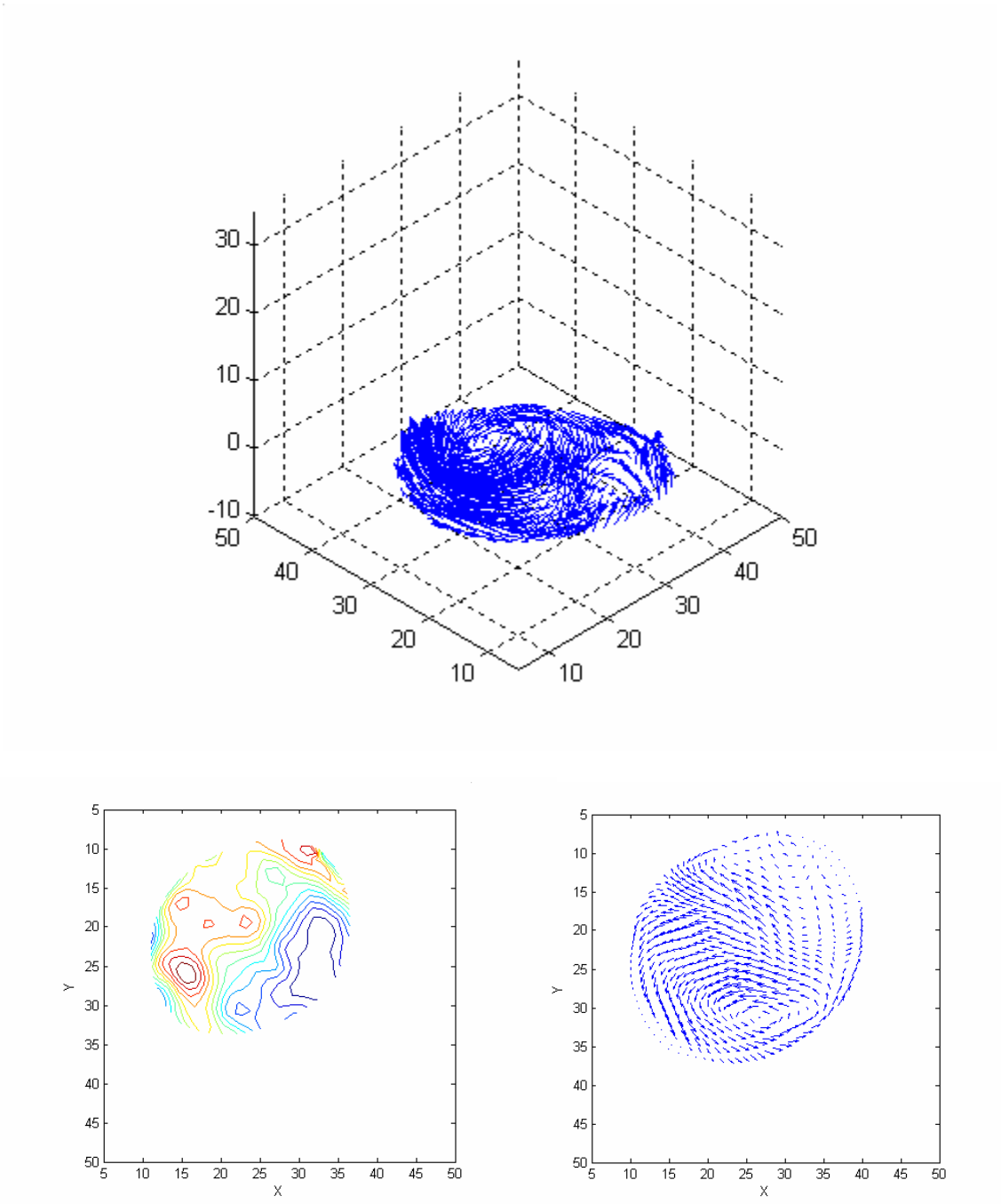

Figure 3.21 (c): The flow patterns come from PC-MRI scanning on the inlet section at 566 ms (indicated by the right arrow in Figure 3.17 (a)).

they had the same cardiac time, there may be deviations among the three lumen's boundaries at a given time in the cardiac cycle. There may be some pixels near the boundary of the lumen that may lose one or two velocity components when the three images are overlapped together. In such cases, these pixels would simply be ignored in the processing. Twenty such sequential distributions of the velocity vectors at different times that spanned a cardiac cycle composed the inlet velocity condition in the CFD modeling. Figures 3.21 (a), (b) and (c) show the velocity distributions at three times where the lengths of the vectors are proportional to the velocity magnitude. The same scale for the velocity vectors is used in all three figures.

The dynamic and varying velocity distributions in the inlet section not only provided insight into blood flow patterns in the aorta root, but also supplied information on the effects of the aortic valve and sinuses of Valsava upon the flow. Figures 3.21 (a), (b) and (c) show the velocity distributions at three specific times, which are the peak flow time, the time of aortic valve closure, and a time in early diastole, as the arrows indicate in Figure 3.22. The velocity distribution on the inlet section at time 226 ms, peak flow time, is shown by 3D vector forms in the upper picture of Figure 3.21 (a); and the lower left picture shows the magnitude contours of the axial velocity, while the lower right picture shows the in-plane velocity vectors. At the peak flow time (indicated by the left arrow in Figure 3.22), the axial velocity component was intensive and dominant, and the major secondary flow direction shown by the in-plane vectors implied that the blood ejection from the heart was not directly along the aortic longitudinal direction, but sloped to the non-coronary cusp or sinus. Some of the re-circulating flows, or vortices, which were

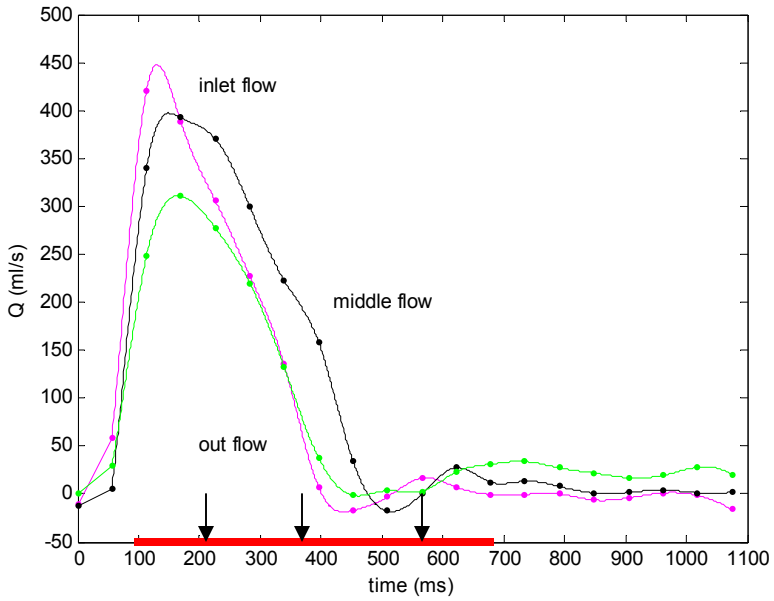

Figure 3.22: Flow waveforms through the aortic lumens on the inlet, outlet and middle sections.

induced by the valve leaflets and located in the sinuses, can be seen in the upper and lower left pictures of Figure 3.21 (a) at this time.

The axial velocity intensity was much diminished and the flow became an asymmetrical rotational or helical flow (see Figure 3.21 (b)) at the later time of systole (indicated by the middle arrow in Figure 3.22). As the three valve leaflets will close together at the same time, the flow pattern in the aorta root becomes an axially oriented, re-circulating flow that moves towards the valve along the inner curvature of aorta and moves away from the valve along the outer curvature (see the lower left picture of Figure 3.21 (b)). The specific helical flow patterns were induced by the specific geometrical structure of the aorta root, aortic valve and sinuses of Valsava. This phenomenon of rotational flow taking place at this time indicates that the original rotational flow components in the aorta root do not come from within the heart.

In early diastole, the re-circulating flow in the aorta root splits into two or more re-circulating flows that can be seen from the lower right picture of Figure 3.21 (c) (the time is indicated by the right arrow in Figure 3.22). Although the intensity of the flow had diminished at this time, the flow patterns became complex. The dynamics of the specific flow patterns shown by Figure 3.21 (b) and Figure 3.21 (c) in the aorta root in the diastolic phase would be expected to affect the entrance flow patterns in the right and left coronary arteries, since most of the coronary artery flow occurs during diastole.

In the outlet section of the descending aorta, only the axial velocity distribution was measured by PC-MRI because the section was located across a relatively straight tube and was far away from the complex flow region of the aorta arch. A traction-free velocity condition was assumed in the outlet sections of the three branches that are

located in the aortic arch. The choice to limit the in-plane velocity information from PC-MRI in the outlet section of the descending aorta and to assume the traction-free condition in the arch branches was based on the following: first, the total MRI scanning time for a single procedure has practical limits, since lying still for a long time can be uncomfortable for the volunteer; second, in order to conserve mass in the CFD computations, there must be at least one outlet where the velocity is not prescribed; and third, the diameters of the arch branches are too small to give good resolution of the velocity distribution.

The velocity distributions obtained *in vivo* were used directly in the simulations, and hence the flow waveforms are illustrative of the time-varying characteristics of the flow. Figure 3.22 shows the flow waveforms in one cardiac cycle through the inlet section in the ascending aorta, the middle section in ascending aorta, and the outlet section in the descending aorta (See Figure 3.19). The flow values were integrations of the axial velocities calculated from the values of the pixels on the PC-MRI phase images in the sections. The time axis of Figure 3.22 expresses the time with respect to the electrocardiogram (ECG), since the PC-MRI scanning was ECG gated.

3.5.3 Blood Flow Data in the Coronary Arteries in Vivo

As discussed previously, the small size of the coronary arteries limits the resolution of the image processing through which the velocity information is obtained from PC-MRI slices. Figure 3.23 shows a slice of the left coronary artery where the field of view is 260 × 260 mm; image resolution is 512 × 512 pixels and the slice thickness is 5 mm. The circular lumen assumption can be used in the modulus image (see the lower left image of

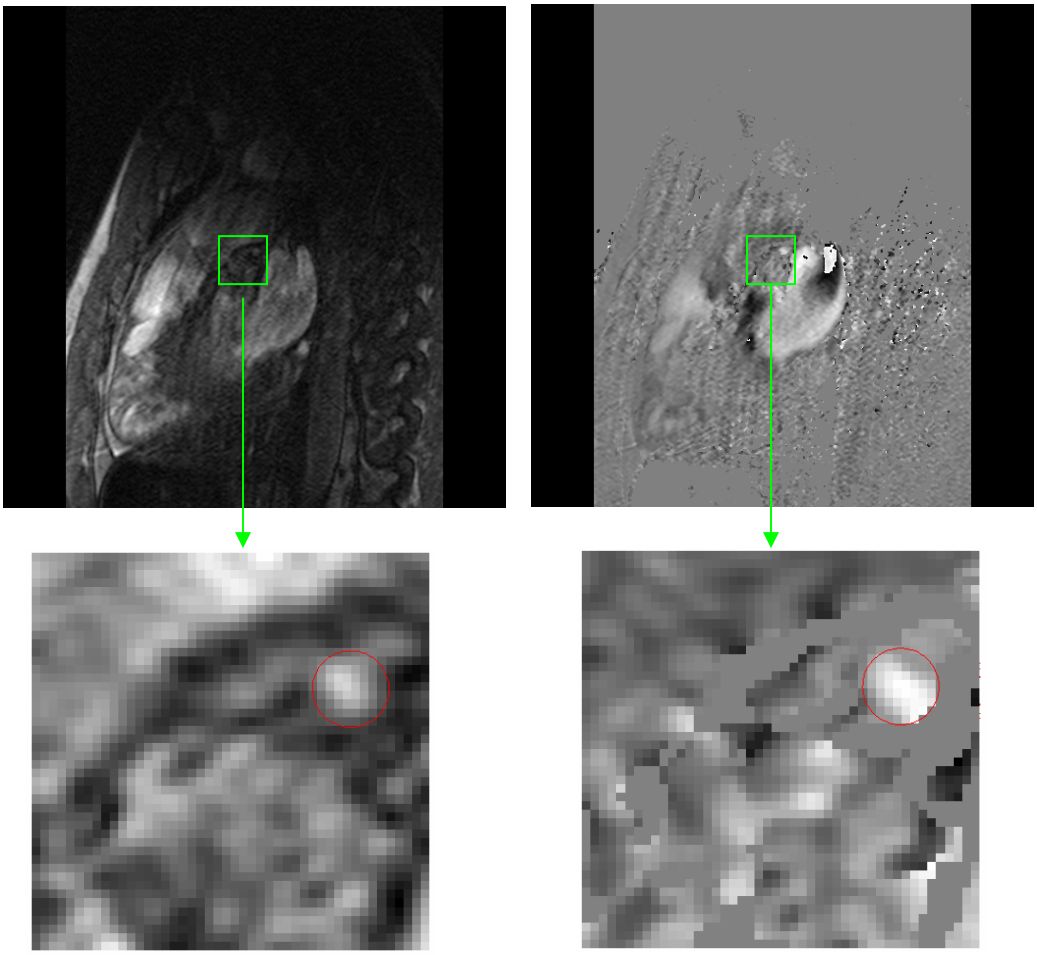

Figure 3.23: PC-MRI slices of the left coronary artery in diastole; the left panels are the modulus images and the right panels are the phase images; the lower figures are the zoom-in images

Figure 3.23), and the circle was controlled to have the same area as the best estimate of the lumen identified in the images. In this case, only the mean velocity in the lumen in the phase image is considered because some velocities apparently registered from outside the lumen may be interpreted as being inside the lumen mistakenly (see the lower right image of Figure 3.23). The waveforms of the mean velocities through the RCA, LAD and LCX are shown in Figure 3.24 where the span of time is normalized to one cardiac cycle.

3.6 Phase Contrast MRI and Information on Compliance and Motion of the Arterial Lumen

3.6.1 Compliance of Aortic Wall

The compliance of the aortic wall certainly affects the instantaneous flow in the aorta, as can be illustrated from the flow waveforms. Figure 3.25 shows an example, which came from another PC-MRI scan of a volunteer different than that for Figure 3.22. In this example, the flow through the branches of the aorta arch was measured by the PC-MRI scanning that went across the outlet sections of the branch lumens (see Figure 3.29). The branch flow was integrated from the velocity distributions and represented in Figure 3.25 (the red curve). The difference between the inlet flow and the sum of the outflow in descending aorta and the outflow in branches could be computed. The difference of flow (the blue curve in Figure 3.25) was not zero, which included two parts: the flow in the coronary arteries and the flow produced by the lumen's compliance in the aorta. The flow in the coronary arteries can be ignored because the flow is very small related to aorta flow and mainly happens in diastole. Therefore, the curve of the difference of flow (the blue curve in Figure 3.25) represents the effects of aortic compliance on the flow.

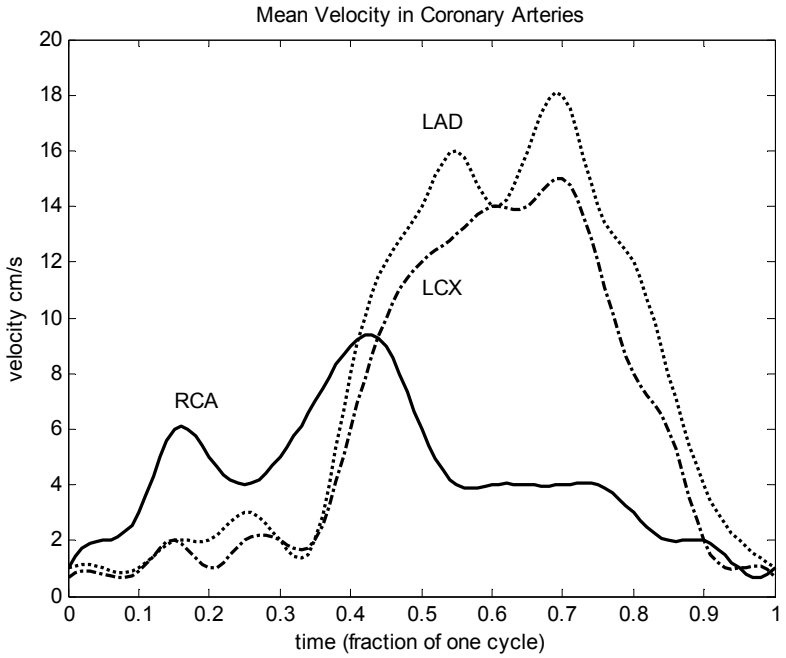

Figure 3.24: Velocity waveforms in the lumens of the RCA, LAD and LCX supplied by PC-MRI scanning across the distal sections of coronary arteries *in vivo*.

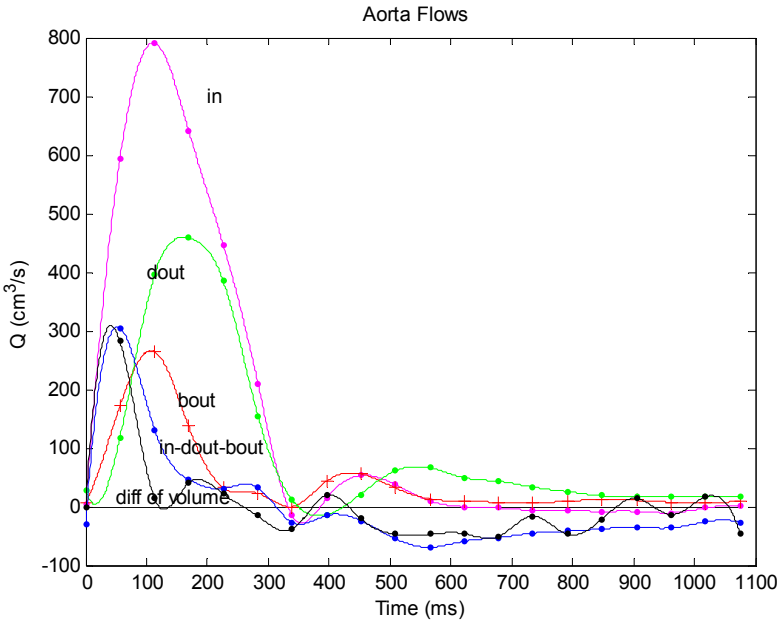

Figure 3.25: The compliance of the ascending aortic lumen.
Bout - sum of flow in the three branches; in-dout-bout – the difference between inflow and outflow; diff of volume – volume gradient of the ascending aorta.

We can make an estimation of these effects on the out flow in the aorta, although we lack complete information about the 3D deformation of the aortic lumen. The periodic changing of the area of the lumen in the middle section of the ascending aorta has been obtained from the PC-MRI slices. Although the deformations of each section along the lumen of the aorta were not the same and the phases of the deformations also had slight differences, the deformation gradient of the lumen in the middle section is assumed to approach the mean deformation gradient of the whole lumen of the aorta. The black curve in Figure 3.25 shows the volume gradient of the aorta that is the deformation gradient of the lumen of the middle section multiplied by the length of the aorta. The blue curve and the black curve have very similar magnitudes and phase in Figure 3.25, which illustrated that the volume gradient of the aorta was approximately equal to the difference of flow between the inflow and the outflow. The phenomenon verifies the buffer function of the aortic lumen in that the aorta expands to store blood and moderates the intensity of the inflow in early systole, and then contracts to increase the outflow in the later time.

3.6.2 Motion of the Aortic Lumen

The boundaries of the aortic lumen segmented from the signal modulus images of the PC-MRI slices were represented by sequential oscillating contours in the scanning plane. The contours presented not only the compliance information of the wall of the lumen but also carried motion information of the lumen. The dynamic contours involved two main movements:

- expansion and contraction of the wall around the center of the lumen due to vessel compliance

- total motion of the aorta in the thorax due to the beating heart

Figure 3.26 (a) shows some of the sequential contours of the inlet lumen from one cardiac cycle. To distinguish the two kinds of motion, the geometrical center of each contour was calculated, forming a time sequence of points. As previously discussed, the contour of a lumen can be approximated as circular if the section is perpendicular to the local axis, so the trace of the centers of the sequential contours in a cardiac cycle describes the motion of the contours, but not its compliance. The motion due to compliance can be simplified to expand or contract around each center symmetrically. The current of arrows in the middle of the contours in Figure 3.26 (a) shows the trace of the centers. Figure 3.26 (b) shows a zoom-in picture of the current of arrows, where the direction of an arrow points in the direction of motion of the center of the contour at the corresponding time and the length of the arrow represents the magnitude of the velocity of the contour motion. The maximum displacement of the movement is 9 mm in Figure 3.26 (b), and the maximum velocity of the movement is about 8 cm/s. The trace of the centers represents an oscillatory movement of the vessel along a curve that has a right hand rotational direction. The specific motion of the ascending aorta and its effects on the flow in the ascending aorta were first described by this current research (Suo, Oshinski and Giddens, 2001). The physiological significance of the specific motion has not yet been investigated.

Information on compliance of the lumen can be obtained from subtracting the movement component of the centers from the total motion data of the contours. Figure 3.26 (c) again shows the contours of Figure 3.26 (a), but their positions are rearranged such that the location of each point of the contours in Figure 3.26 (a), represented by X

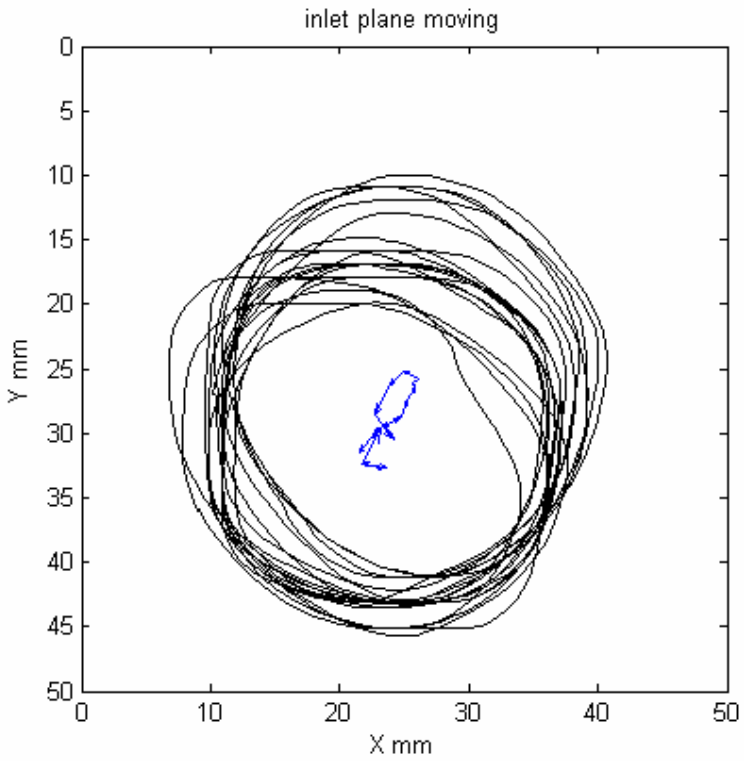

Figure 3.26 (a): Sequential boundary contours of the inlet lumen in one cardiac cycle.

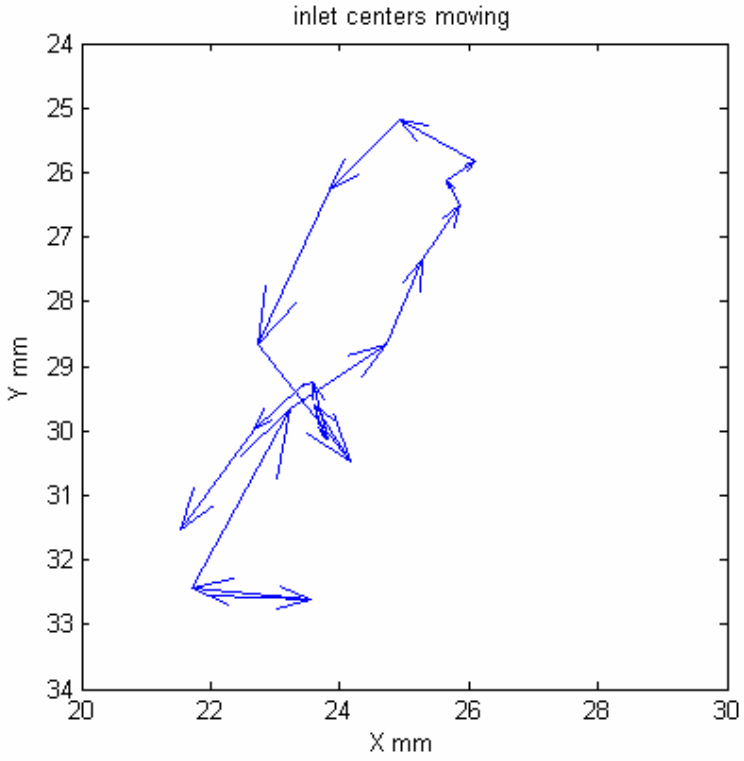

Figure 3.26 (b): Trace of the centers in one cardiac cycle.

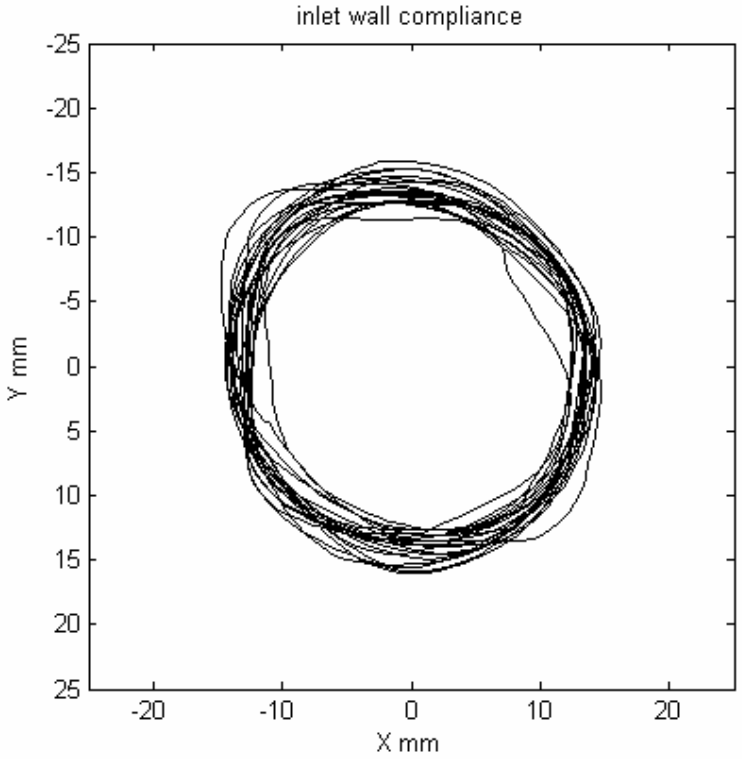

Figure 3.26 (c): Compliance of the inlet lumen.

and Y in the coordinate system, has had the coordinates of the corresponding centers overlaid to a single point. From Figure 3.26 (c) we can calculate the areas and the diameters of the inlet lumen at each time. The relative difference between the minimum and maximum of the areas on the inlet lumen is about 20%, and the average relative difference of the diameters is about 12%.

In the middle section of the ascending aorta, we perform similar processing to obtain the compliance and movement data from the PC-MRI slices. Figure 3.27 shows results of the middle section that have the same description as the inlet section in Figure 3.26. The maximum displacement of the movement of this section is 4 mm (see the middle figure of Figure 3.27), that is, about half the displacement of the inlet section. The distal section of the ascending aorta connects with the aortic arch, so that the bearing axis, or fulcrum, of the oscillatory motion of the ascending aorta seems to be at the arch and the beating heart is the source of the movement. The average relative difference of the diameters of the middle lumen is 10% in one cardiac cycle.

Figure 3.28 shows the compliance and movement of the boundary contours of the outlet lumen that is in the descending aorta. The maximum displacement of the movement of the outlet lumen is less than 2 mm and the average difference of the diameters of the lumen exceeds 2 mm, so that the compliance of the lumen is the dominant source of wall motion at the outlet section.

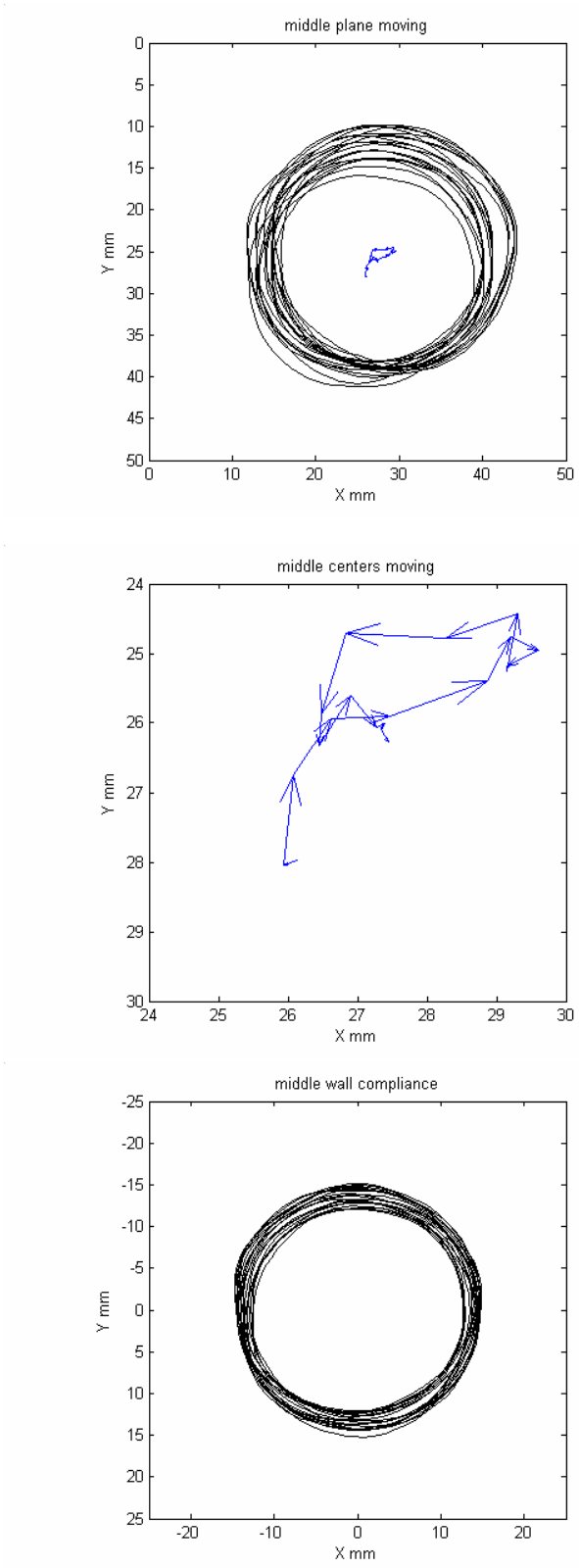

Figure 3.27: Compliance and movement of the middle lumen

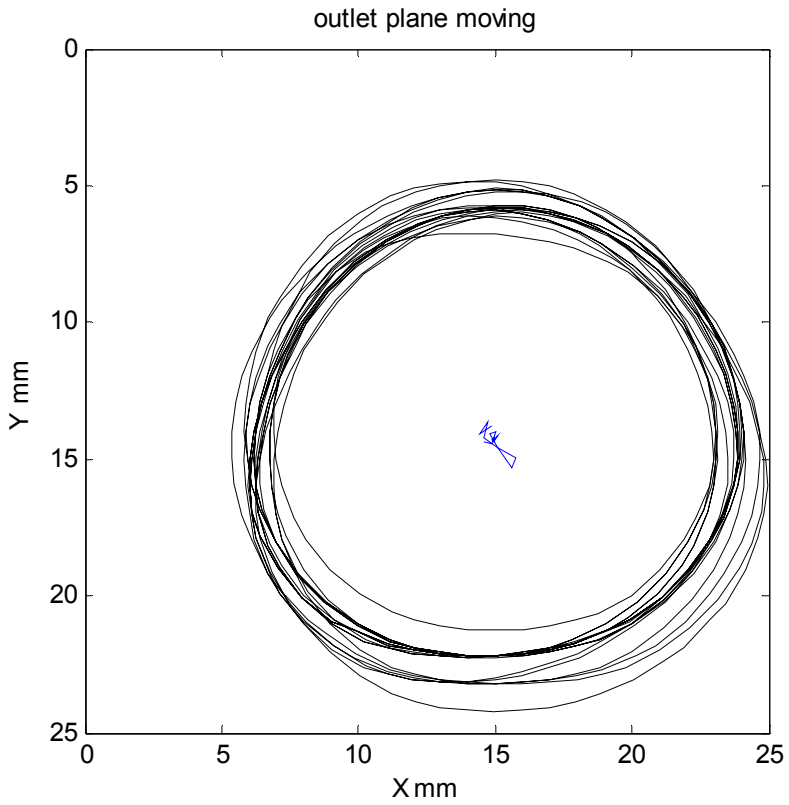

Figure 3.28: Compliance and movement of the outlet lumen that is in the descending aorta.

3.7 Governing Equations and Assumptions

Arterial blood flow is pulsatile and three-dimensional; and although blood exhibits non-Newtonian behavior at steady, low shear rates, it is generally accepted that blood in large arteries (> ~ 1 mm) may be considered to be Newtonian to a good approximation. Further, Nichols and O'Rourke (1998) concluded that in subjects with normal aortic valves and cardiac output, blood flow disturbances were only present near the aortic valve during a small portion of time of one cardiac cycle. Thus, we assumed laminar flow in the computations. Further supporting the assumption of laminar flow was the fact that the PC-MRI velocity data in the inlet section gave no indications of signal losses from turbulence.

3.7.1 Governing Equations

The general mathematical statements of fluid flow are the conservation equations: mass, momentum and energy. Since blood flow in arterial segments is isothermal, the energy equation can be ignored, leaving the continuity and momentum equations as the governing relations for flows of interest in this research:

Continuity equation:

$$\frac{\partial \rho}{\partial t} + \vec{\nabla} \bullet (\rho \vec{U}) = 0$$

Momentum equations:

$$\frac{\partial (\rho u)}{\partial t} + \vec{\nabla} \bullet (\rho u \vec{U}) = -\frac{\partial p}{\partial x} + \frac{\partial \tau_{xx}}{\partial x} + \frac{\partial \tau_{yx}}{\partial y} + \frac{\partial \tau_{zx}}{\partial z} + \rho f_x$$

$$\frac{\partial (\rho v)}{\partial t} + \vec{\nabla} \bullet (\rho v \vec{U}) = -\frac{\partial p}{\partial y} + \frac{\partial \tau_{xy}}{\partial x} + \frac{\partial \tau_{yy}}{\partial y} + \frac{\partial \tau_{zy}}{\partial z} + \rho f_y$$

$$\frac{\partial (\rho w)}{\partial t} + \vec{\nabla} \bullet (\rho w \vec{U}) = -\frac{\partial p}{\partial z} + \frac{\partial \tau_{xz}}{\partial x} + \frac{\partial \tau_{yz}}{\partial y} + \frac{\partial \tau_{zz}}{\partial z} + \rho f_z$$

where ρ is the fluid density, $\vec{U}$ = (u,v,w) is the fluid velocity vector, p is the pressure, $\vec{f}$= (f_x,f_y,f_z) is the body force, τ_{ij} are the viscous stresses and $\vec{\nabla} = (\frac{\partial}{\partial x}, \frac{\partial}{\partial y}, \frac{\partial}{\partial z})$.

For blood flow in human arteries, some practical assumptions of the flow can be made to simplify the equations:

- blood flow is incompressible
- the viscosity of the blood is constant

With these assumptions, the continuity and Navier-Stokes equations become:

$$\frac{\partial u}{\partial x} + \frac{\partial v}{\partial y} + \frac{\partial w}{\partial z} = 0$$

$$\frac{\partial u}{\partial t} + u\frac{\partial u}{\partial x} + v\frac{\partial u}{\partial y} + w\frac{\partial u}{\partial z} = -\frac{1}{\rho}\frac{\partial p}{\partial x} + \upsilon\nabla^2 u$$
$$\frac{\partial v}{\partial t} + u\frac{\partial v}{\partial x} + v\frac{\partial v}{\partial y} + w\frac{\partial v}{\partial z} = -\frac{1}{\rho}\frac{\partial p}{\partial y} + \upsilon\nabla^2 v$$
$$\frac{\partial w}{\partial t} + u\frac{\partial w}{\partial x} + v\frac{\partial w}{\partial y} + w\frac{\partial w}{\partial z} = -\frac{1}{\rho}\frac{\partial p}{\partial z} + \upsilon\nabla^2 w$$

where υ is the kinematic viscosity of the blood and $\nabla^2 = \frac{\partial^2}{\partial x^2} + \frac{\partial^2}{\partial y^2} + \frac{\partial^2}{\partial z^2}$.

The equations represent 4 transport equations in 4 unknowns: u, v, w, and p, so they are well posed.

3.7.2 Boundary Conditions

The numerical solution of the above equations of fluid motion requires boundary conditions to be defined. The equations and boundary conditions represent a unique description of the state of the flow in a geometrical model. The boundary conditions can be divided to two types for purposes of the present research:

- Data measured *in vivo*, which are used in the boundary conditions directly
- Assumed boundary conditions that come from reasonable assumptions regarding the physical phenomena involved.

The inlet conditions are important considerations in arterial CFD modeling (e.g. Chang and Tarbell, 1985; Komai and Tanishita, 1997; Ting, 1999). In this research the pulsatile 3D velocity distribution on the inlet section of the aorta supplied by PC-MRI scanning *in vivo* was transferred to the CFD model directly (see Figure 3.29). The transfer process is a mathematical interpolation on the inlet section. Figure 3.30 illustrates this, where the red points are the cell's centers of the CFD mesh (as the velocity is available on the cell's surface of the mesh at the inlet section of the CFD model) and the green points represent the boundary of the lumen on the modulus image that was segmented by the Snakes method. The CFD mesh was registered on the PC-MRI images by overlapping both geometrical centers of the lumen and the CFD mesh, and then the velocity interpolation of the red points took place on the phase image. There are some red points that are located outside the lumen (see the lower image of Figure 3.30). In these cases, the velocity value at the red points is forced to zero. The transfer process shown in the figure was for only one velocity component, but the other two components were transferred similarly. The three velocity components at the red points represent the inlet conditions at one time in the cycle, and all the velocity component data at 20 times were saved in a file that could be read out and put in the correct cells during the CFD calculation.

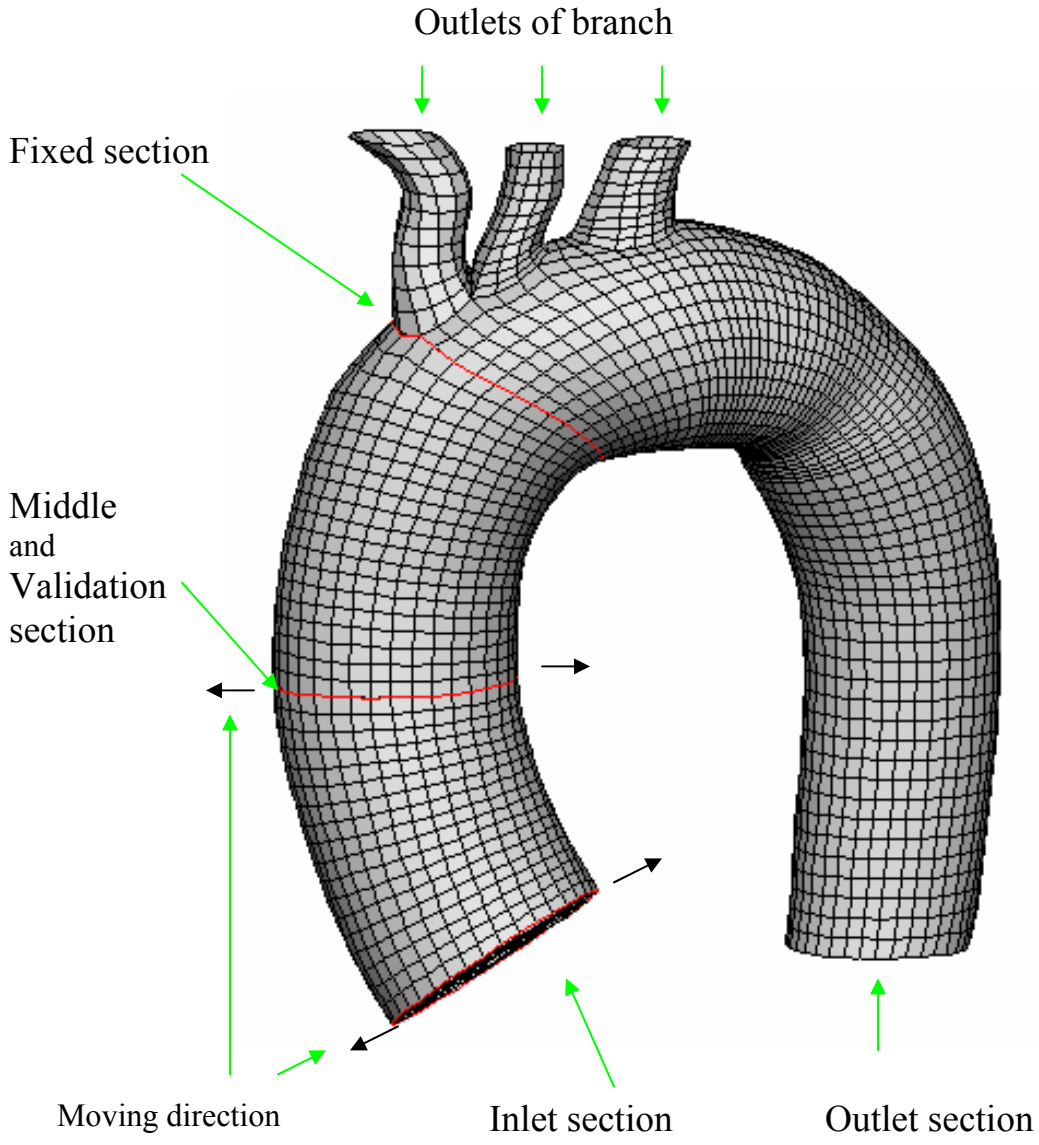

Figure 3.29: Boundary conditions of the CFD modeling.

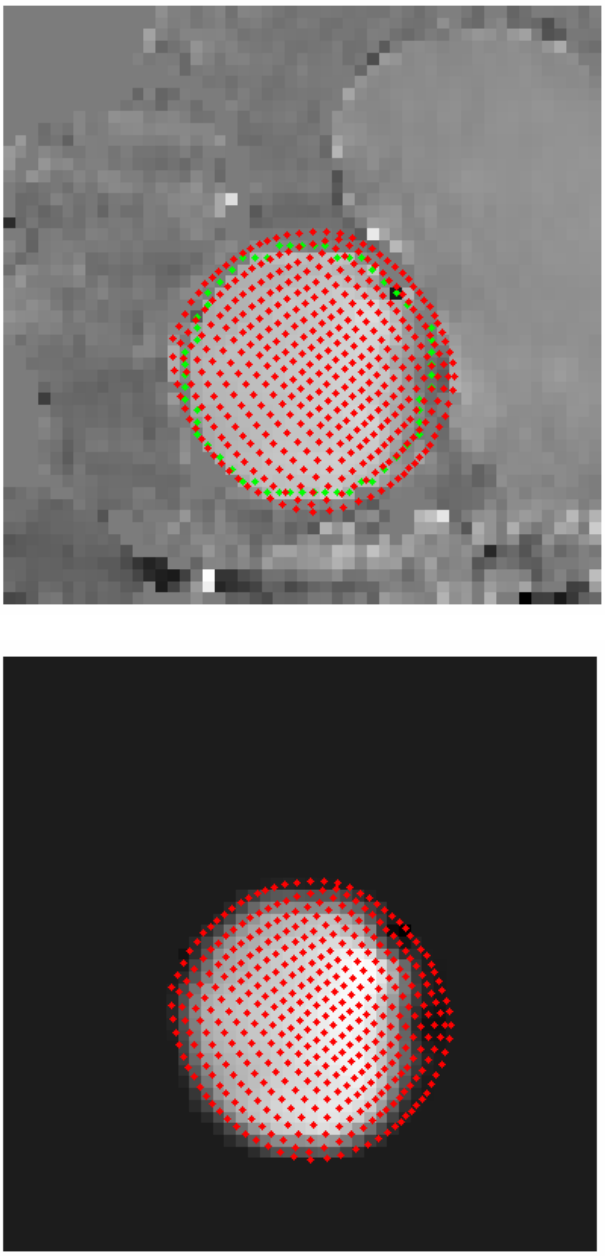

Figure 3.30: PC-MRI inlet velocity distribution was transformed to the CFD inlet section: the red points are the cell's centers of the mesh on the inlet section of the CFD model; green points are the boundary segmented from the modulus image; the upper image is the modulus image; the lower image is the phase image where the pixels outside the lumen are forced to be zero.

As discussed in the previous chapter, the outlet section in the descending aorta is located across a relatively straight tube and is far away from the ascending aorta, so that only the axial velocity was considered to be important. The velocity distribution at the outlet section was also supplied by PC-MRI scanning *in vivo*, and the transfer process from the image slices to the CFD model was the same as described for the inlet section.

Other outlet conditions are at the three branches of the aortic arch. As described previously, the traction-free flow condition was assumed in the branches' outlet sections:

$$-p\vec{U}+\frac{1}{\mathrm{Re}}\frac{\partial\vec{U}}{\partial\vec{n}}=0$$

where $\vec{n}$ is the unit normal vector at the outlet section.

If we further assume that the pressure at the outlet sections is zero, which means all the pressures in the modeling will be relative pressures, the condition becomes:

$$\frac{\partial\vec{U}}{\partial\vec{n}}=0$$

On the arterial wall, the no-slip condition was assumed:

- In the modeling with rigid wall: $u=v=w=0$
- In the modeling with moving wall, the blood on the wall had the same velocity as the wall.

3.7.3 Wall Motion

As the vessel movement is mainly in the ascending aorta, the CFD model was a partial wall motion model in the research. The inlet and middle sections were controlled to change their areas and centers according to the PC-MRI data in the modeling, and

other grid positions between the inlet and fixed sections (see Figure 3.29) were interpolated at each time step. All the surfaces beyond the fixed section are rigid walls.

Attention was first focused on two objectives of the research: to reproduce the flow in the ascending aorta and to check whether vessel motion affects the flow field inside. To explore the latter, two other CFD models were designed in addition to the full wall motion model. The first model assumed that the wall of the ascending aorta is compliant but the lumen centers do not move; the second assumed all rigid walls with no motion. In the case of the rigid wall model, we imposed the geometry measured during diastole, when radial motion was minimal. For examining compliance effects, the axis of the ascending aorta was fixed, but the wall was forced to move radially with the motion that was measured in the PC-MRI scanning. For the "full motion" model, both radial expansion-contraction and the measured motion of the axis were imposed. Wall motion perpendicular to a section was not considered in the research.

3.7.4 Velocity Boundary Conditions

PC-MRI scanning across the distal sections of coronary arteries *in vivo* supplied the mean velocities in the lumens of the RCA, LAD and LCX individually (see Figure 3.24), and these velocity data were transformed to the coronary outlet sections in the models to be the outlet conditions in the combined model, as the upper part of Figure 3.31 shows. The assumption of uniform velocity in the outlet sections of coronary arteries is expected to have little effect on the exploration of velocity distributions in the coronary entrance segments, as the outlet sections are located more than 10 diameters downstream. According to this consideration, the coronary entrance flows should be controlled by the

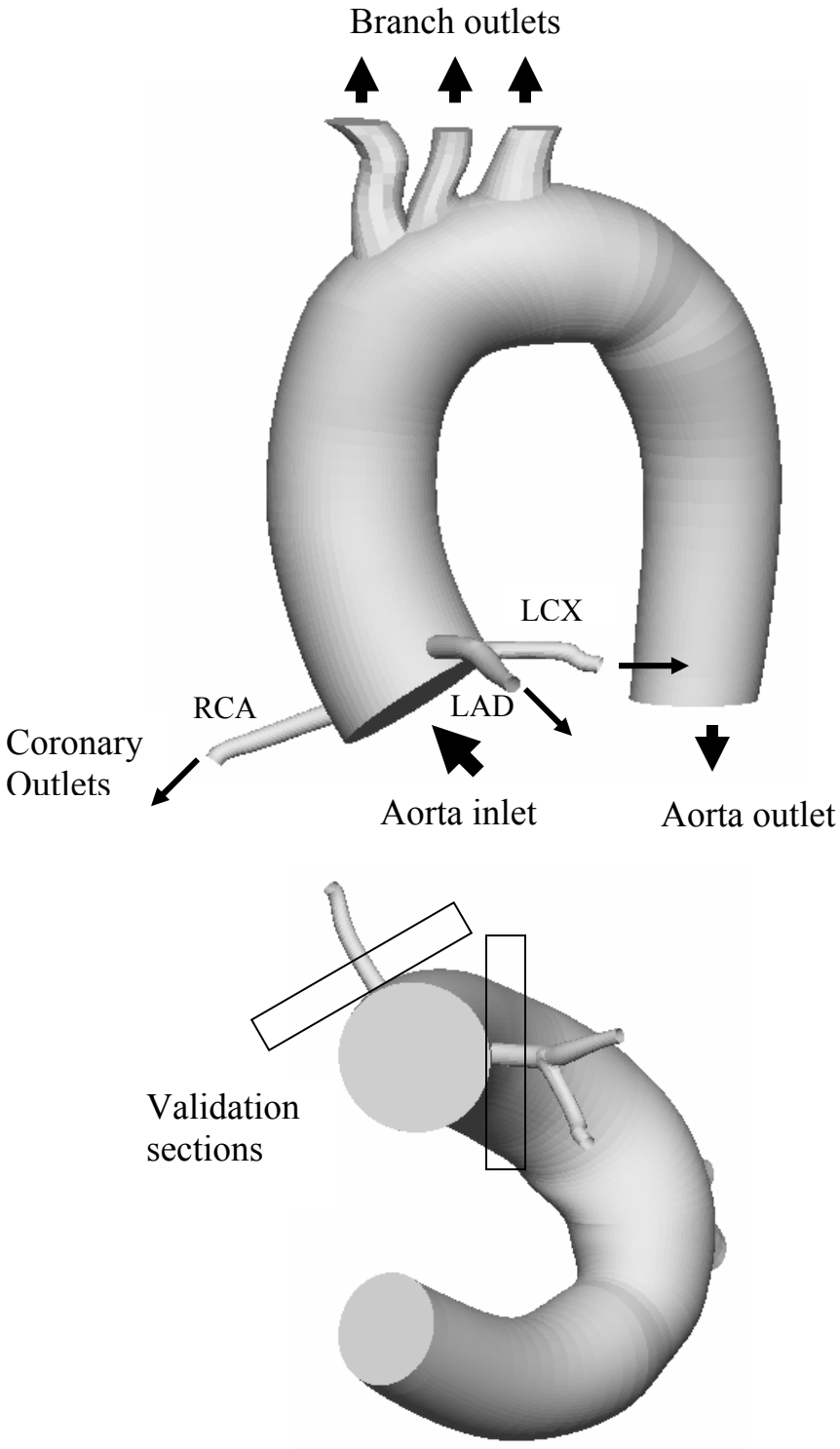

Figure 3.31: The boundary conditions and validation sections of the combined model.

flow patterns in the aorta root and the spatial orientations of the coronary arteries that join with the aorta root.

The CFD results of the combination modeling should be validated, as with the aorta modeling, using PC-MRI scanning *in vivo*. The PC-MRI scanning was performed in two specific sections (see the lower of Figure 3.31) that were perpendicular to the axis of the local coronary arteries and near to the aorta, and only the axial velocity distribution was considered in the scanning. As we discussed previously, the PC-MRI slices cannot supply exact velocity distributions across lumens of coronary arteries in all times of cardiac cycle, but some characteristics of the velocity distribution, such as the peak velocity position, can be distinguished at certain times. The characteristics of the velocity distribution will be used to compare with the corresponding CFD results and to perform the validation.

3.7.5 Initial Conditions

It is necessary to supply initial velocity and pressure conditions in CFD simulations. In the study, it was difficult to obtain detailed data of the blood flow states in an arterial lumen at any given time *in vivo*. A solution may be to perform the simulation in more than one cardiac cycle, and another simple approach is to assume a constant velocity and pressure for the initial conditions. We found in practice that the difference in the results between constant initial conditions and computing more cycles was small, so that constant initial conditions is used in the study.

CHAPTER 4

RESULTS

4.1 Flow Patterns in the Ascending Aorta

The aortas of four healthy males were scanned by MRI, and the blood flow patterns were computed using the methodology described in the previous chapter. Results from the four subjects were very similar in their qualitative nature, and thus we will concentrate on presenting results from one of the models that were developed, using additional subjects only to illustrate certain points.

4.1.1 PC-MRI Results

In addition to providing data for the CFD simulations, the results from PC-MRI scanning also yield much useful information about aortic blood flow. Figure 4.1 shows several sequential PC-MRI slices at the middle section of the ascending aorta at 114 – 683 milliseconds (See the time span covered by the red line in Figure 3.22.): the left column shows the modulus images; the middle column shows the corresponding phase images; and the right column shows the zoom-in images of the lumens where the axial velocity distributions have been isolated and coded by color. The velocity values can be transformed from the color bars that below the images. The dynamic velocity profiles represented by the sequential velocity distributions express the time dependent blood flow patterns in the ascending aorta.

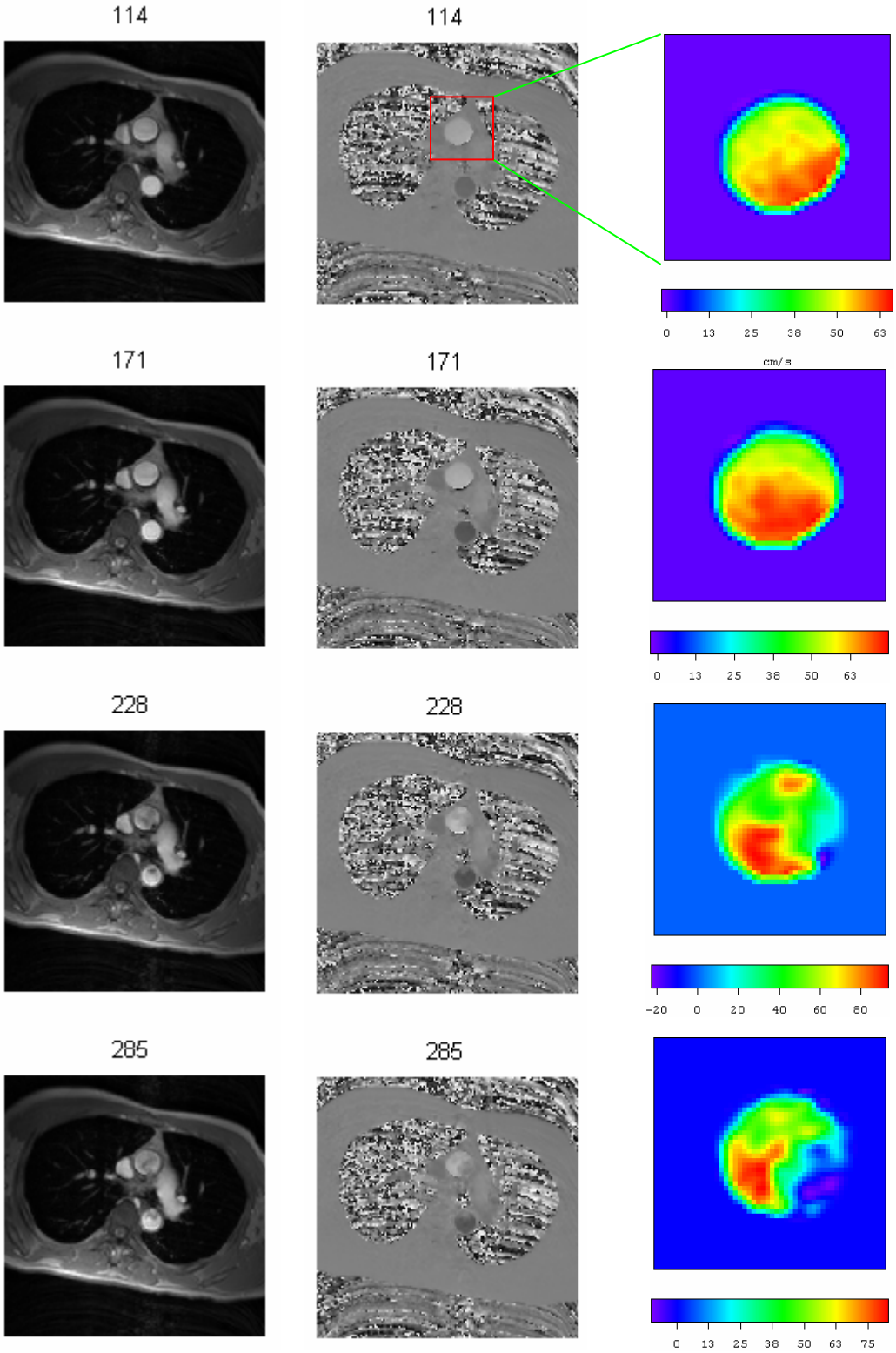

Figure 4.1: Eleven PC-MRI slices in the middle section of ascending aorta across 114 - 683 milliseconds (see the red line in the Time axis of Figure 3.22): the lefts are the modulus images; the middles are the phase images; the rights are the axial velocity distributions in the lumens of the ascending aorta.

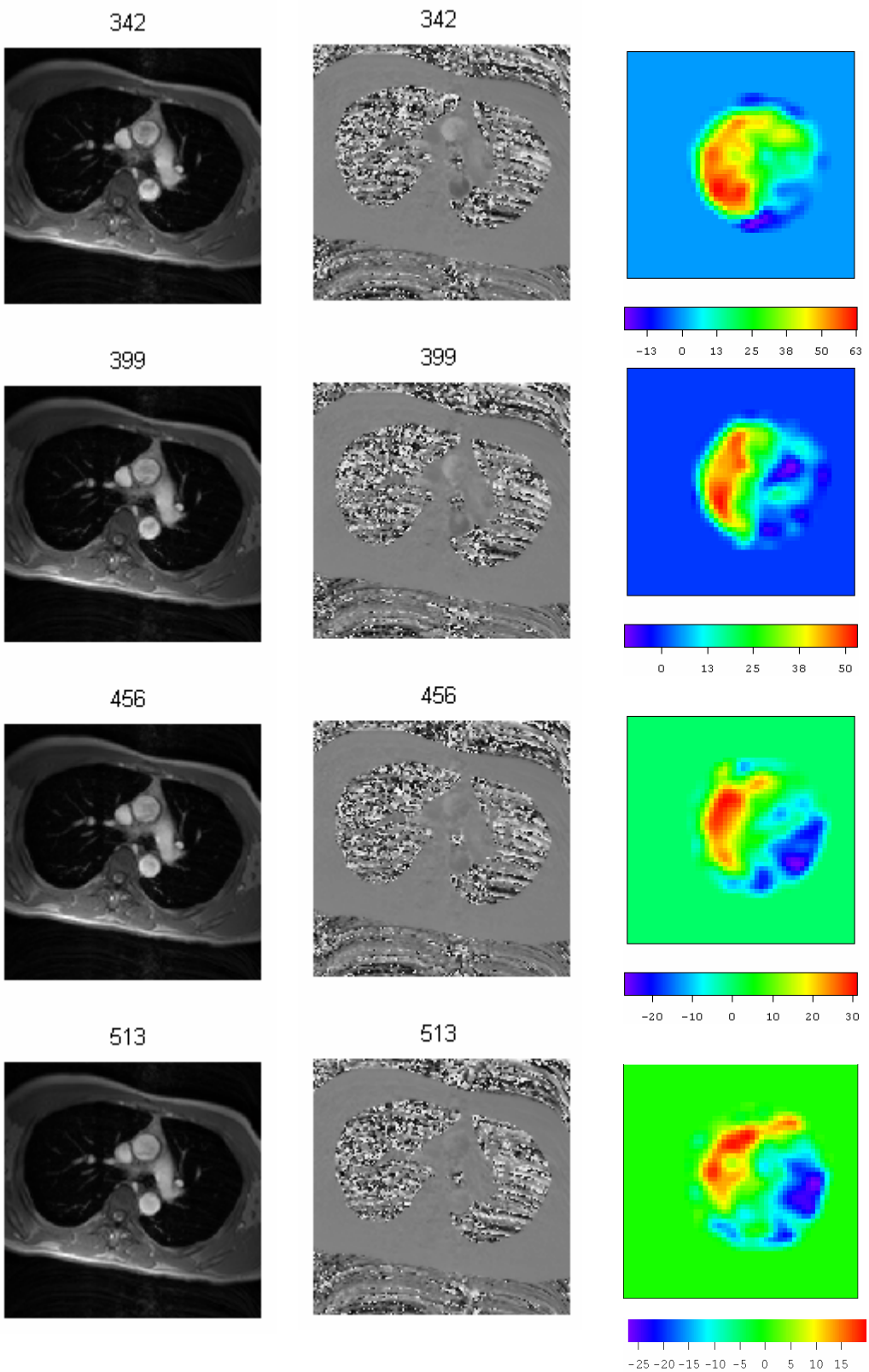

Figure 4.1: (continued)

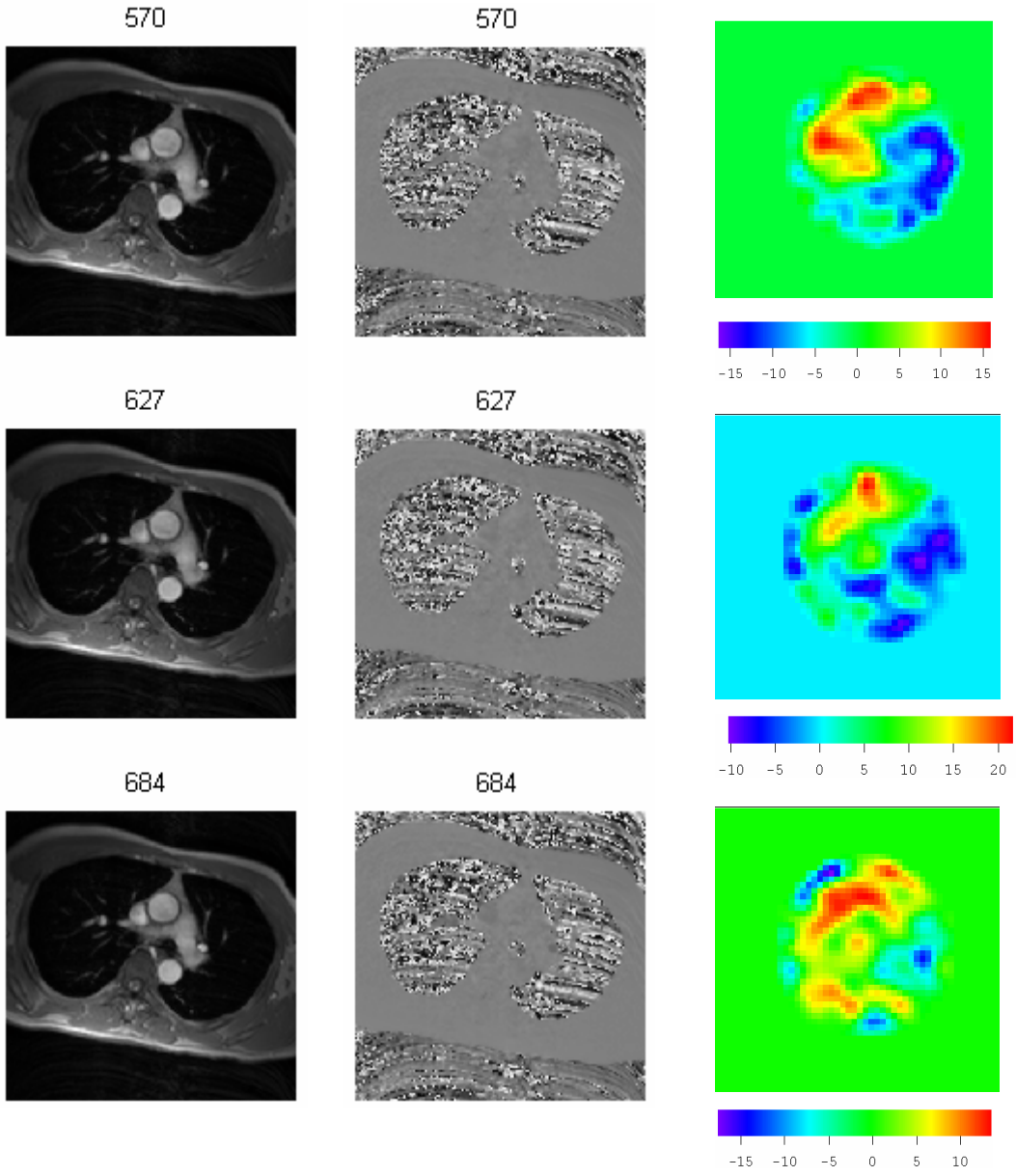

Figure 4.1: (continued)

In Figure 4.1, all the lumens are in the same orientation related to the body as shown in the left modulus images, and the view is looking from the heart toward the arch. The flow waveforms in Figure 3.22 give a reference for time in the cycle. At 114 milliseconds, the jet flow front emanating through the aortic valve reached the middle section where the maximum axial velocity was above 60 cm/s (Figure 4.1, right panel). The velocity distribution was asymmetric in the lumen, with the peak velocity occurring in the neighborhood of the inner curvature and the low velocity region along the outer curvature. As systole continued, the peak velocity position rotated clockwise, and total flow reached a maximum at 171 ms. This rotation of the location of peak velocity continued during the next four sequential times: the peak velocity position was in the right posterior side of the lumen at 228 ms; the right side at 285 ms; and the right anterior position at 342 ms and 399 ms. Although the maximum velocity was more than 50 cm/s at 399 ms, the flow rate was much decreased as there were areas of low and even negative velocities. This movement of the peak velocity position implies that flow in the ascending aorta has a strong secondary rotational component forming a right-hand helical pattern during systole.

The aortic valve closed and the inflow became zero at 456 ms, but the maximum velocity remained near 30 cm/s on the outer curvature and a region of locally negative velocity appeared on the inner curvature of the ascending aorta. After 456 ms, positive velocity continued to occupy the right half of the lumen and negative velocity occupied the other half, while the maximum velocity decreased to less than 15 cm/s at 683 ms. This phenomenon of positive velocity in the outer curvature and negative velocity in the

inner curvature continued through almost all the diastolic period, suggesting formation of an axial vortex in the ascending aorta.

There was no inflow into the aorta during diastole, but there would be some outflow due to blood being supplied to the coronary arteries and possible outflow through the arch vessels as the compliance of the aorta caused recoil of the walls. The phenomenon has been discussed in chapter 3.6.1 where we estimated the mean compliance of the lumen and diameter of the ascending aorta (see Figure 3.25).

Figures 4.2 (a) and (b) show the velocity distributions in the inlet section that came from the PC-MRI slices shown in Figure 3.20, and these velocity data were used for boundary conditions for the CFD computations. Figure 4.2 (a) shows the axial velocity distribution where the velocity magnitude is coded by color as the right column in Figure 4.1 shows. The in-plane velocity is shown in Figure 4.2 (b) by 2D vectors that were composed of two in-plane velocity components. The lengths of the vectors are proportional to the magnitude of the in-plane velocity.

The axial velocity (Figure 4.2 (a)) and the in-plane velocity (Figure 4.2 (b)) compose the 3D velocity in the inlet section. Observing the velocity distribution in Figure 4.2 (a) we find that the rotation of the peak velocity position in the lumen that was observed in the middle section does not happen in the inlet section in systole. At this same time, we cannot find any uniform rotational flow patterns from the in-plane velocity distribution in Figure 4.2 (b). These PC-MRI slices tell us that the rotational tendency of the helical flow patterns in the aorta do not originate from the heart but are produced and strengthened in the ascending aorta.

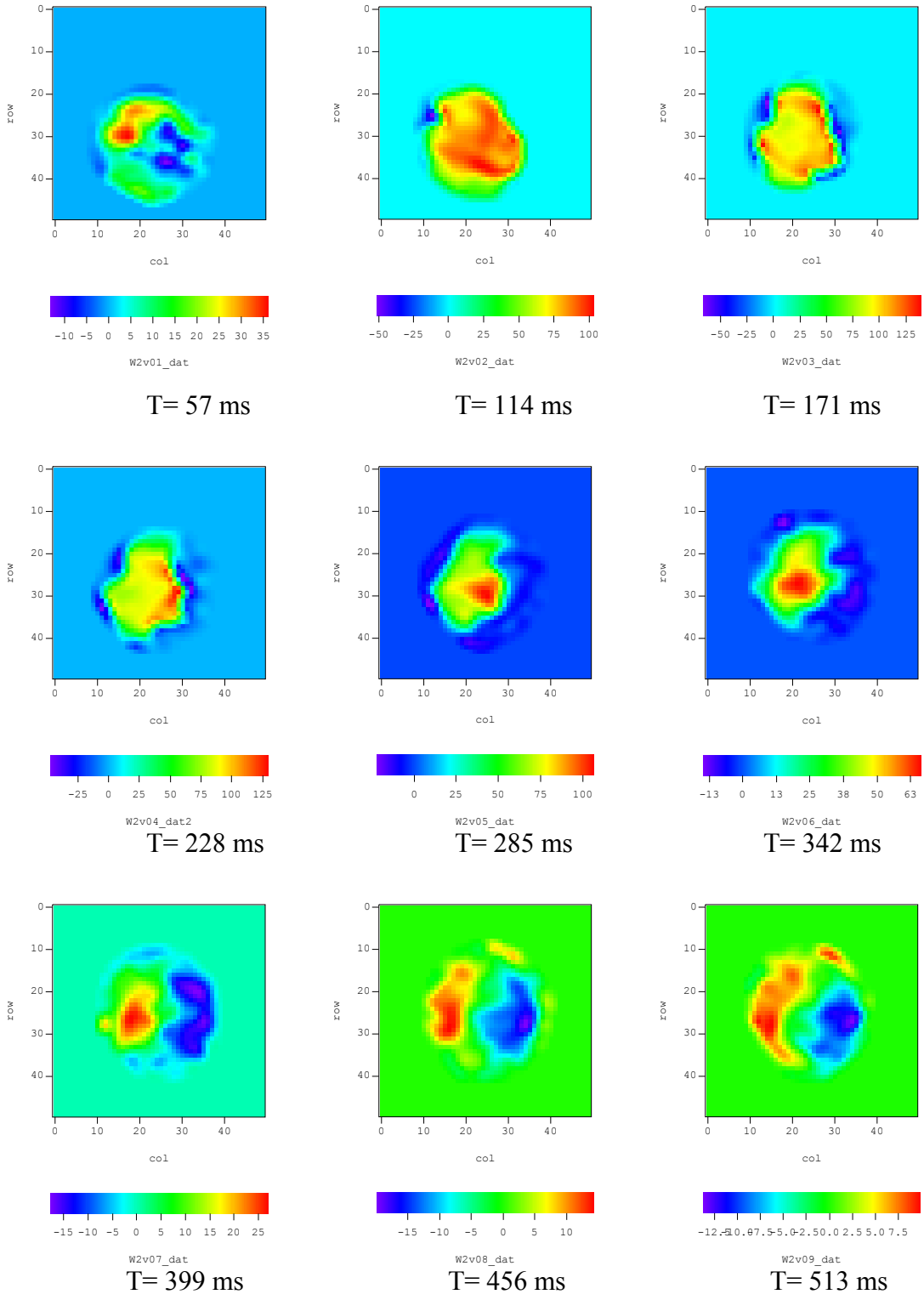

Figure 4.2 (a): PC-MRI slices: axial velocity distribution in the inlet lumen.

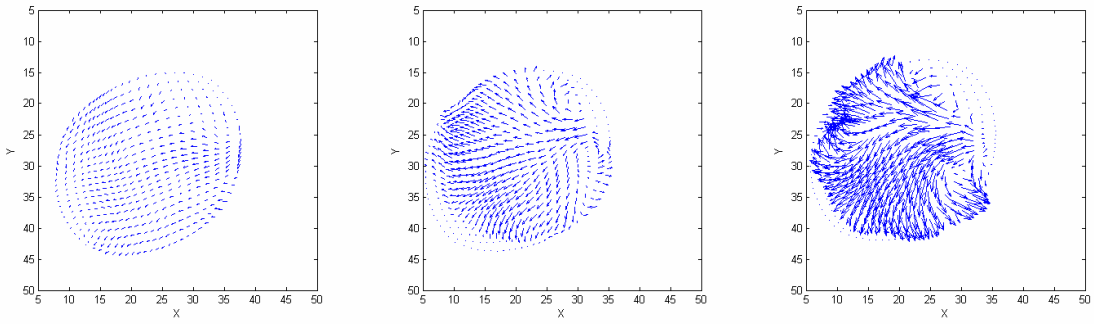

T= 57 ms T= 114 ms T= 171 ms

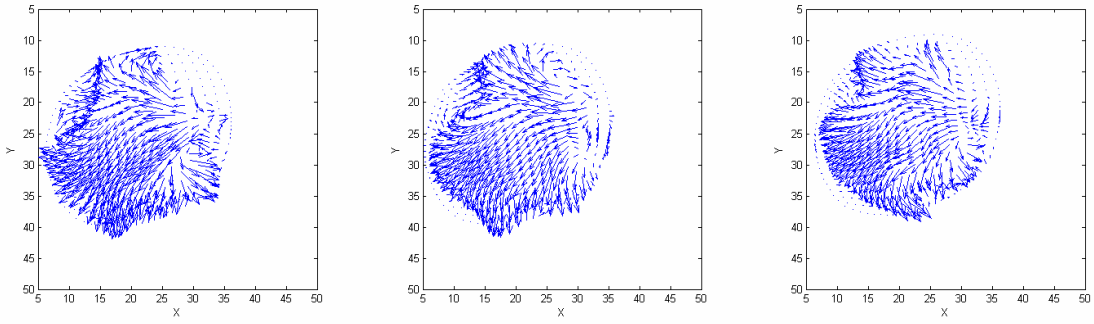

T= 228 ms T= 285 ms T= 342 ms

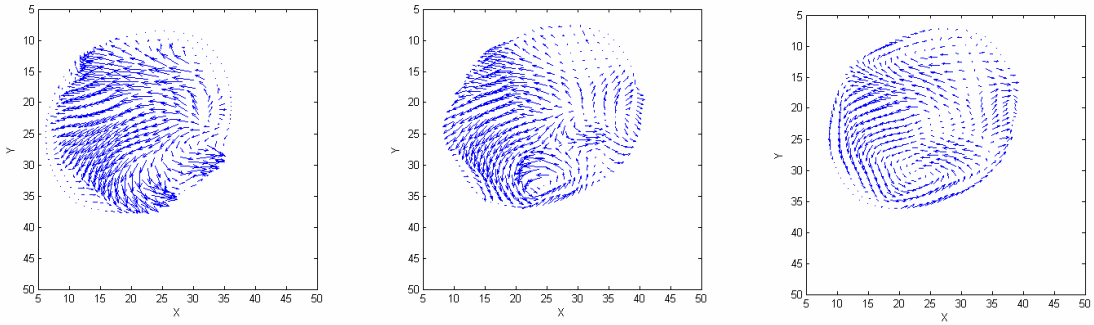

T= 399 ms T= 456 ms T= 513 ms

Figure 4.2 (b): PC-MRI slices: inplane velocity distribution in the inlet lumen where the lengths of the vectors are all on a common scale.

In diastole, the positive axial velocity occupied the outer curvature of the lumen and the negative velocity appeared on the inner curvature, similar to the flow behavior in the middle section. These clear velocity distributions in both sections suggest that the axial flow patterns spanned most of the ascending aorta and formed a large axial vortex. The blood flowed backward to the left coronary sinus along the inner curvature of the ascending aorta; its direction was turned when the leaflets were encountered; and then it flowed forward again along the outer curvature. Observing the in-plane flow at this time, the velocity magnitude was diminishing but the rotational components continued, implying that the axial vortex flow was dominant, although it was a "twisted" vortex. After 513 ms the vortex flow pattern became unclear and appears to have split into several small vortices. During the latter stage of diastole, the flow patterns had no clearly defined structure and the velocity magnitudes were small, so no additional images are presented.

4.1.2 CFD Results

Figure 4.3 shows the 3D velocity distribution produced by CFD modeling in the ascending aorta, and the color map on each section expresses the local axial velocity magnitude. In this figure, the velocity distribution on the inlet section is taken directly from the PC-MRI results shown in Figure 4.2, where the axial velocity distribution coded by color is transposed from Figure 4.2 (a). The quiver of vectors in each section expresses the 3D velocity distribution, with the length of the vectors being proportional to the local velocity modulus and the direction being that of the velocity. The velocity vectors in Figure 4.3 describe the 4D blood flow patterns in the ascending aorta, and the

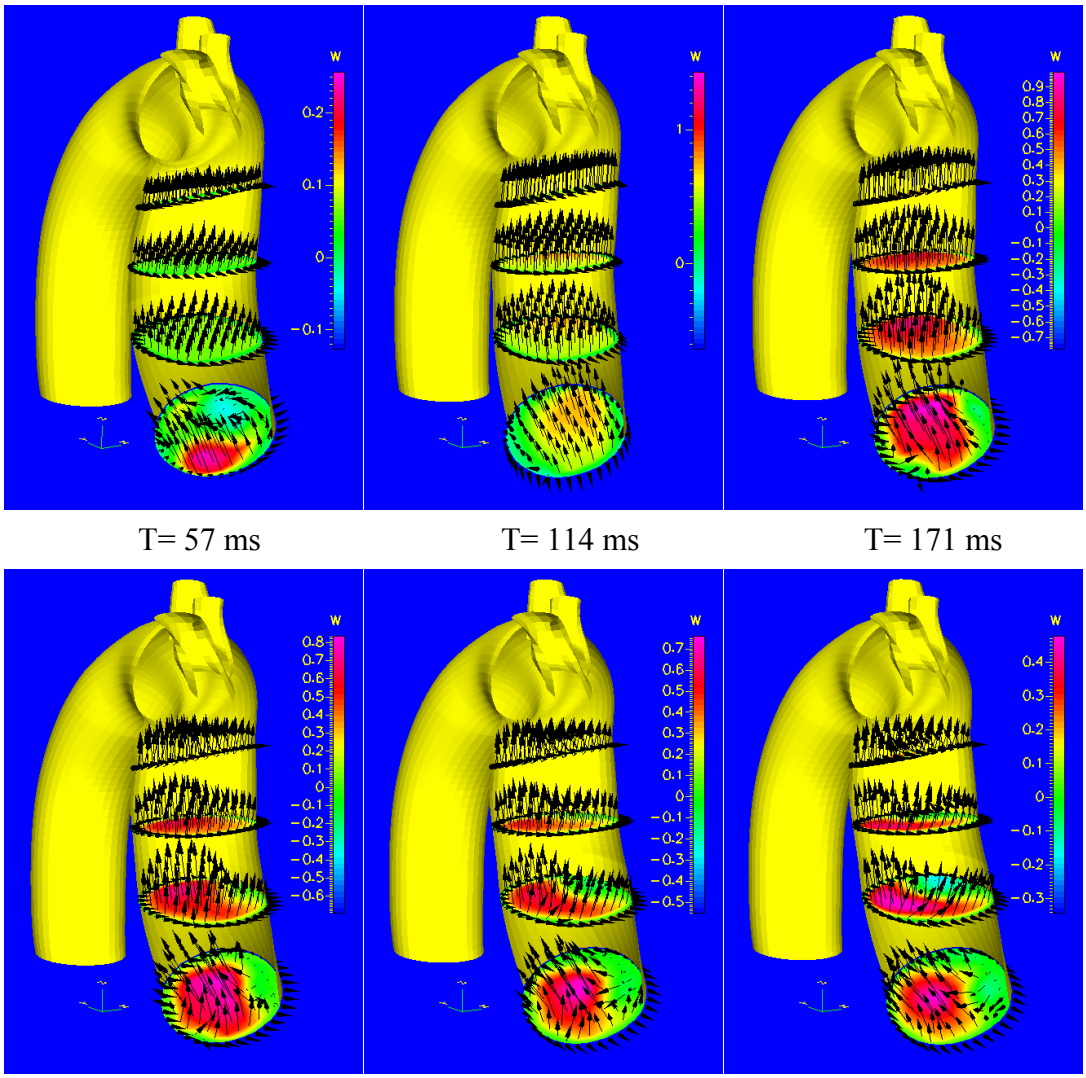

Figure 4.3: CFD results: velocity vectors and magnitude distributions in the ascending aorta, where the arrows were the 3D velocity vectors and the color map in the sections represented the axial velocity magnitude. The velocity distribution in the inlet section is the PC-MRI results (see Figure 4.2).

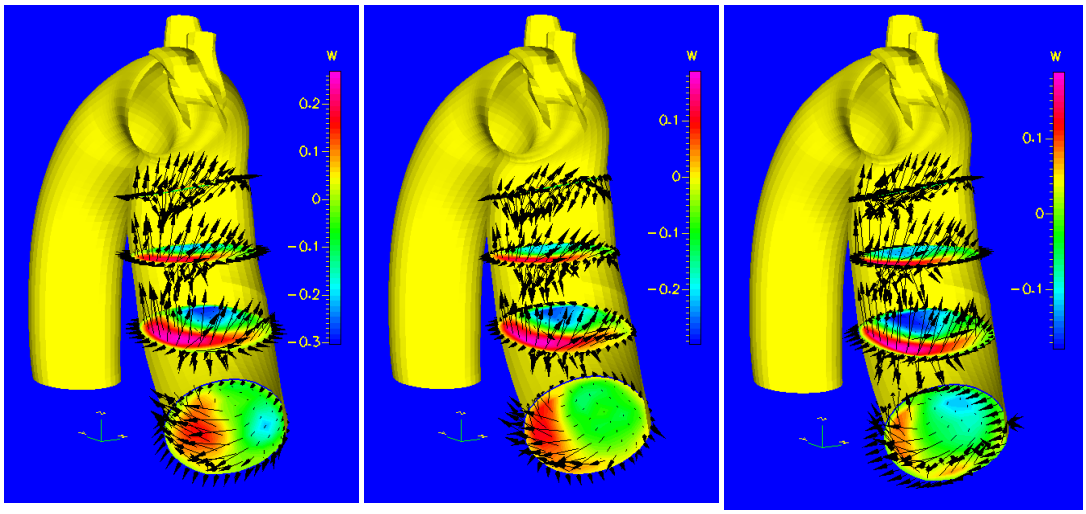

T= 399 ms T= 456 ms T= 513 ms

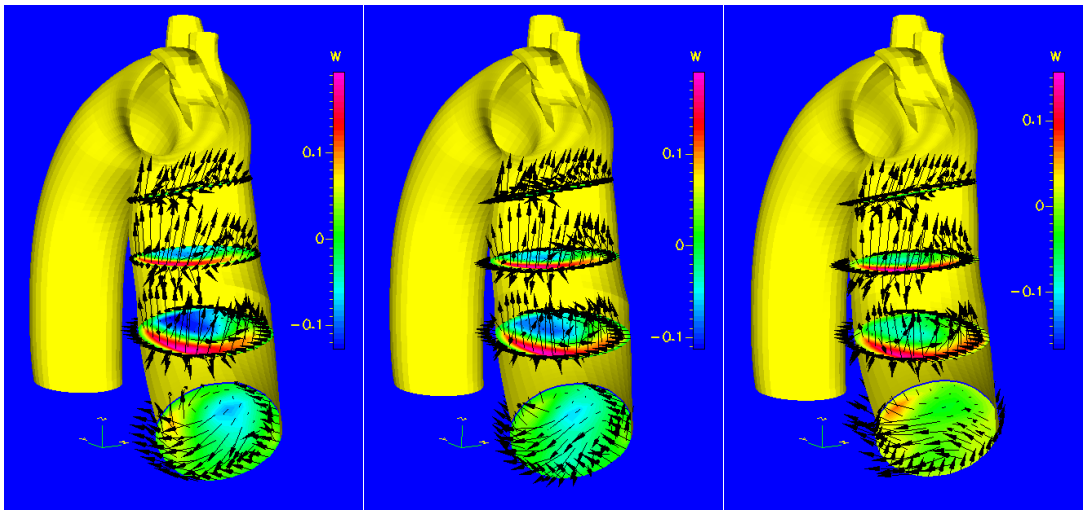

T= 570 ms T= 627 ms T= 684 ms

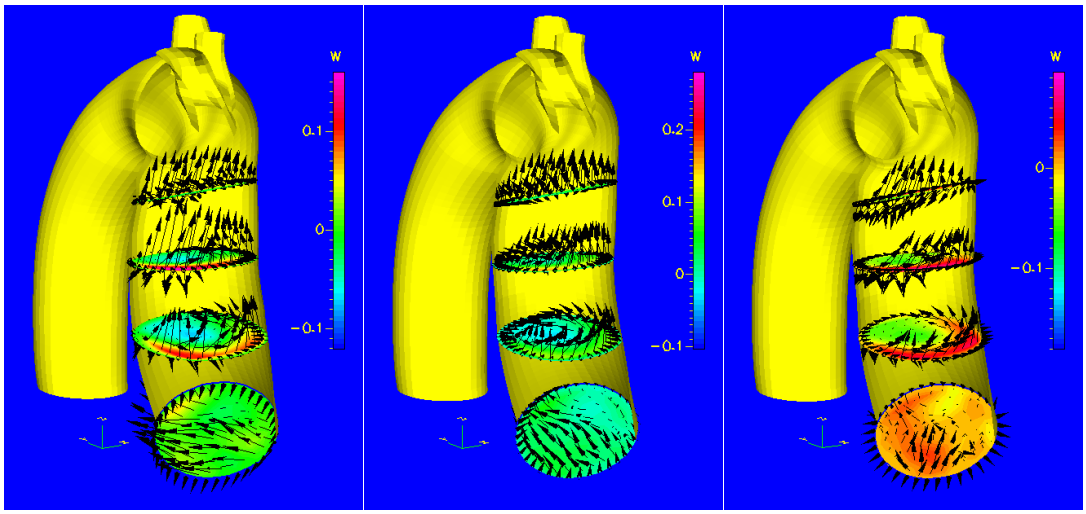

T= 741 ms T= 798 ms T= 855 ms

Figure 4.3: (continued)

dynamic flow states that appeared as right-hand helical flow patterns can be seen from a video animation of the sequential figures.

It is important to validate the CFD results by either *in vitro* experiments or measurements obtained *in vivo*. The validation in this study is performed by comparing the axial velocity distribution in the middle section with the PC-MRI scans at the same section. The CFD computations did not use any information from the PC-MRI scans in the middle section, so that the scanning results represent independently measured, *in vivo* data. To compare with the PC-MRI slices, the position of the CFD model was re-orientated (see the lower image in Figure 4.4 where the position of the model was re-orientated according to the upper image) to show the middle section in the same position as the PC-MRI image *in vivo* (see the left column in Figure 4.1). The lower image in Figure 4.4 shows the axial CFD velocity distribution in the middle section at 114 ms, and the vectors around the lumen's wall expressed the deformation velocity of the moving wall.

The axial velocity distributions in the middle sections of the sequential CFD results and the corresponding PC-MRI slices are shown in the left and right columns in Figure 4.5. The rotational characteristics of the peak velocity positions in the aortic lumen represented by the PC-MRI measurements also appeared in the CFD results. The shapes of velocity profiles expressed by the color maps in the PC-MRI slices and CFD sequential results were very similar. Additionally, the ranges of the velocity magnitude shown by the color bar in the PC-MRI slices and CFD results were also very similar at each time and showed that both velocity profiles coincided. There were some minor irregularities in the velocity distributions shown by PC-MRI slices in late diastole that

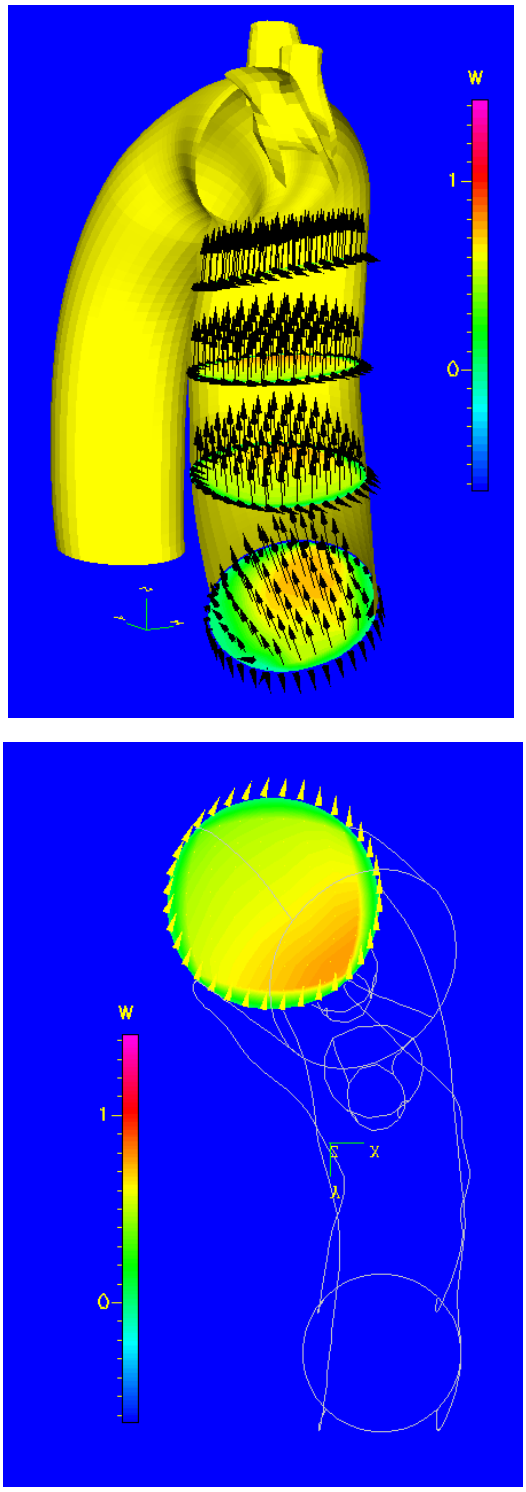

Figure 4.4: The axial CFD velocity distribution in the middle section at 114 ms. The upper image came from Figure 4.3 and illustrates the orientation of the lower image.

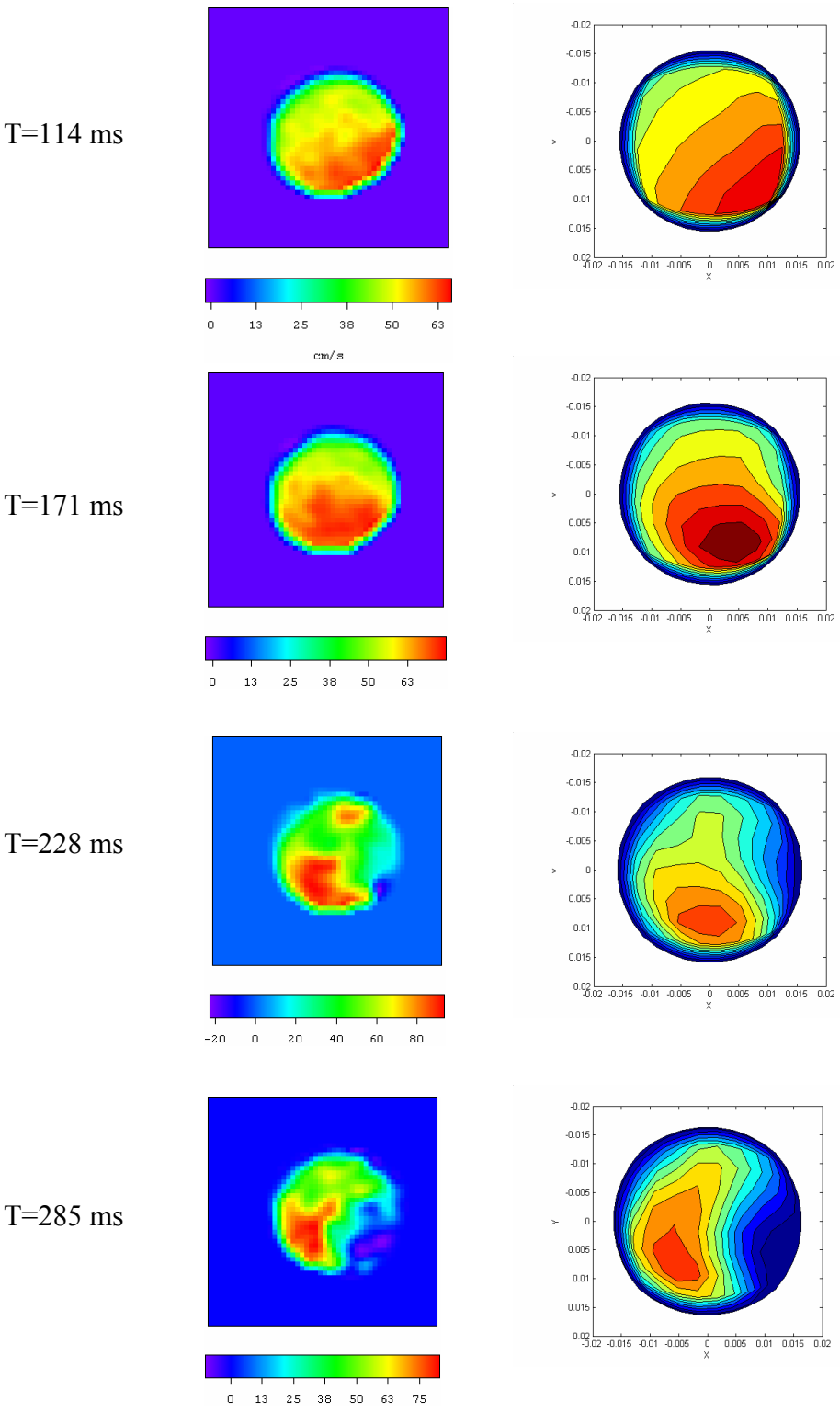

Figure 4.5: Validation of the CFD velocity distribution by PC-MRI measurements in the middle section. The velocity scale of the color bars is centimeters per second.

T=342 ms

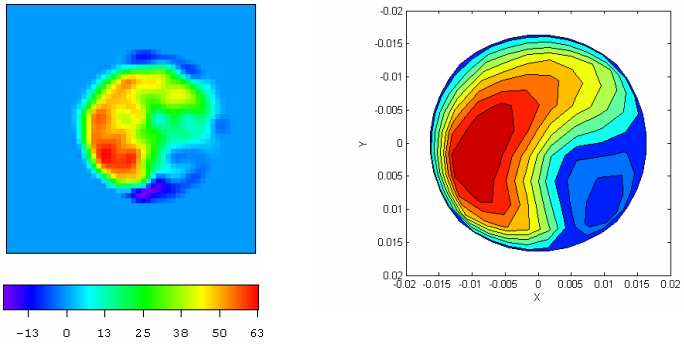

T=399 ms

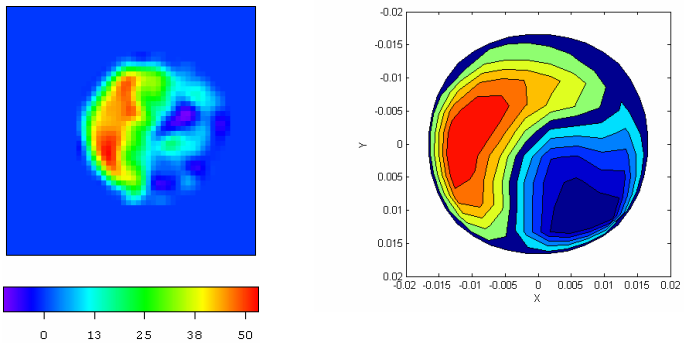

T=456 ms

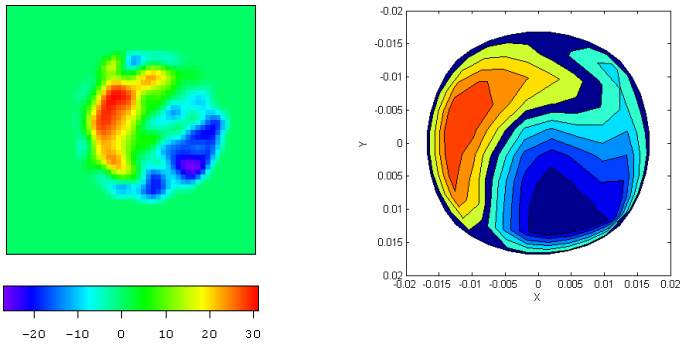

T=513 ms

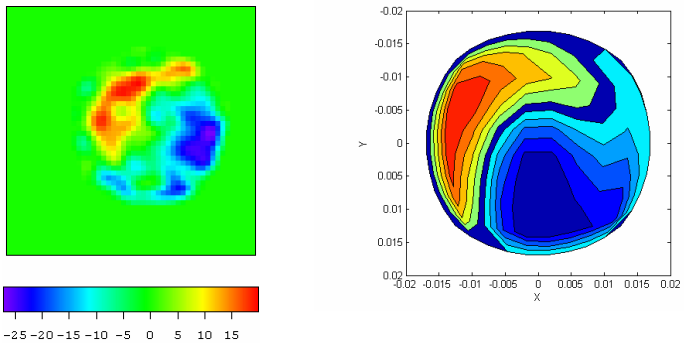

Figure 4.5: (continued)

may be due to the ratio of signal and noise being too small at these times in the MRI scans.

In addition to comparing with PC-MRI scanning *in vivo*, the CFD results can also be compared with clinical observations in the literature. As discussed in Chapter 2, Kilner et al. (1993) observed the right-hand helical flow pattern in human aortas using MR mapping techniques. Since their results were more flow visualization than velocity measurements, the flow patterns in the ascending aorta in a cardiac cycle were drawn schematically using their perception of stream lines. Figure 2.1 showed their results, and the drawings are depicted again in the right column of Figure 4.6 for comparison with the CFD results. Instantaneous streamlines, defined to be tangent to the local velocity vector at any instant of time, can be calculated from the computed velocity field, and these are shown in the left pictures of Figure 4.6.

The instantaneous streamlines are illustrated in Figure 4.6, shown "originating" at 12 grid locations in the inlet section. Four lines originated near the center of the lumen, four lines started near the wall, and another four lines began in the intermediate regions of the lumen. The streamlines were symmetrically distributed across the inlet section. The size of the arrows that was along the lines is proportional to the magnitude of the local flow velocity, and the direction pointed in the local velocity direction. It is emphasized that these do not represent particle path lines, however, because the flow is unsteady.

During the peak flow phase, 114, 171 and 228 milliseconds, axial flow dominates across the lumen, velocity is high, and there is no flow separation. The velocity located near the inner curvature of the aorta is higher than that near the outer curvature. The flow

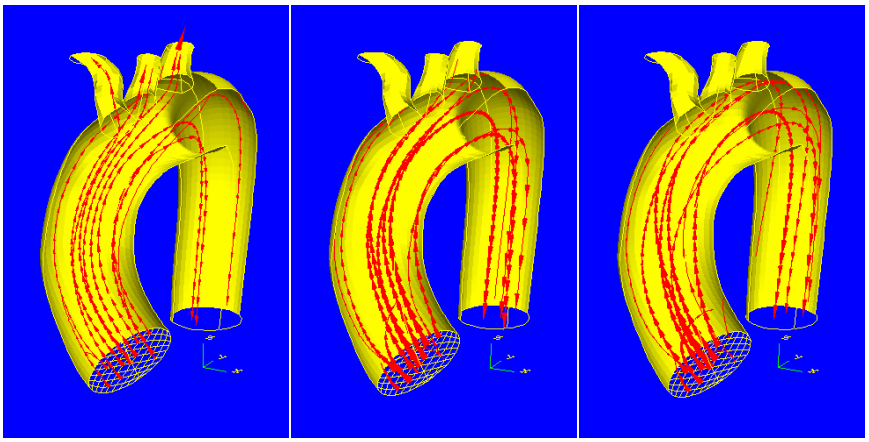

T=114 ms T= 171 ms T=228 ms

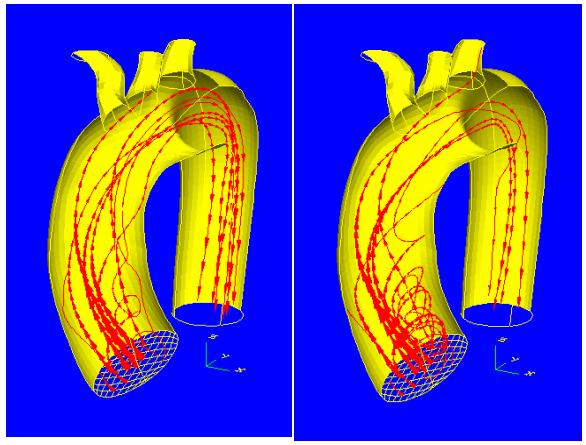

T=285 ms T=342 ms

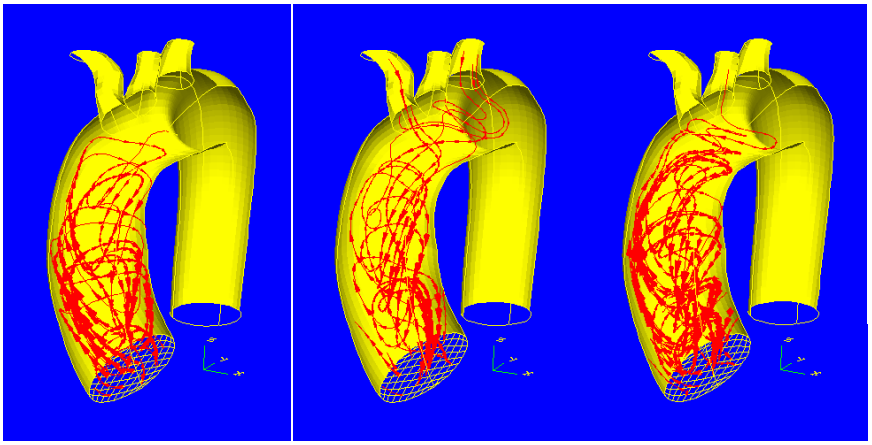

T=399 ms T=456 ms T=513 ms

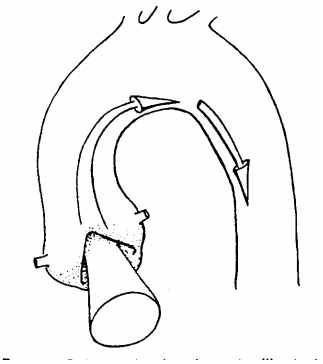

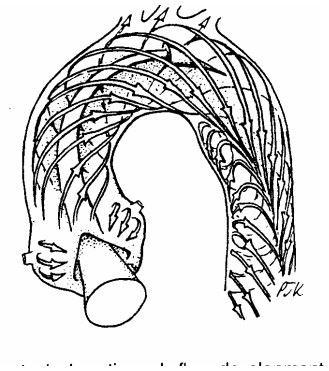

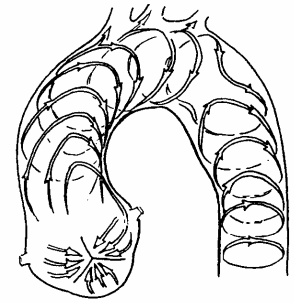

Kilner, P., etc.
Circulation, 88(5),1993

Figure 4.6: CFD results: streamlines in the ascending aorta (left), and Kilner's observations results in vivo (right).

pattern presented by the streamlines at this phase is very similar to the sketches of Kilner et al. (1993).

During the flow deceleration phase, 285 and 342 milliseconds, flow near the wall becomes skewed, especially along the outer curvature where the flow presents a right-hand helical tendency, while the flow in the center continues in the axial direction. This pattern is also consistent with observations from the clinical MR mapping.

At the later stages of systole and during early diastole, 399, 456 and 513 milliseconds, the aortic valve is closing and the inflow becomes zero. With no net forward flow, the streamlines in the ascending aorta demonstrate strong secondary flow patterns, forming right-hand helical loops. The structure of the flow resembles an oblique vortex in the lumen of the ascending aorta. As Figures 4.1 and 4.2 illustrate, the proximal end of this vortex-like structure was in the aortic sinus and extended distally well into the ascending aorta. As before, the characteristics of the computed streamlines during this time resembled those found *in vivo* by Kilner et al. (1993).

The close similarity of the dynamic velocity profiles in the CFD results with clinical observations could not be simply fortuitous, since these represent completely independent studies. The similarity demonstrated gives added confidence that the flow patterns produced by CFD modeling are a realistic representation of the blood flow patterns in the ascending aorta. Further, the helical flow patterns computed in the ascending aorta have not been reported from *in vitro* studies. The validation of the CFD results using *in vivo* data is perhaps the best certification of the methodology.

4.2 Causes of Helical Flow Patterns in the Ascending Aorta

The helical flow patterns observed in the human ascending aorta have been reproduced in this study, but the causes that create and control the skewed flow patterns are not immediately clear. As discussed in Chapter 2.1, the twisted curvature of the aorta has been proposed as a cause of creating the helical flow, and some investigators have postulated that the rotational secondary flow originates from the heart. The latter consideration lacks evidence, as demonstrated in this study, based on the analysis of PC-MRI slices in the inlet section presented in Chapter 4.1.1.

We developed three aorta models that were based on the CFD/MRI technique to examine the causes. We consider three candidates as possible contributors to the observed flow patterns: (i) the complex geometric curvature; (ii) wall motion due to compliance; and (iii) full wall motion, including that resulting from the beating heart. To investigate these factors, the aortic flow simulations were performed in the following three different CFD models:

- Model 1 incorporated expansion and contraction of the arterial lumen and overall motion of the ascending aorta
- Model 2 allowed only expansion and contraction of the lumen
- Model 3 was a completely rigid wall with no motion allowed.

Except for wall motion, all structures and boundary conditions of the three models were the same.

The CFD results for the axial velocity distribution at the middle section in the three models are shown in Figure 4.7. The PC-MRI *in vivo* results at this section at the same times are presented in the left column of Figure 4.5. All the CFD sections have the same

Compliance and movement Compliance Rigid

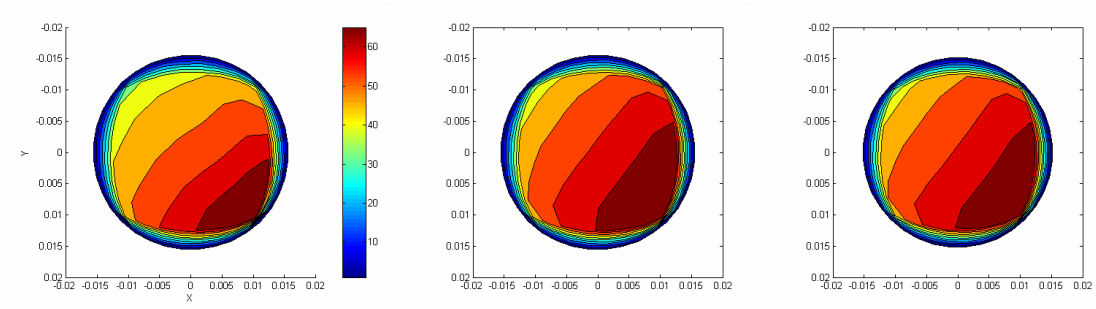

T=114 ms

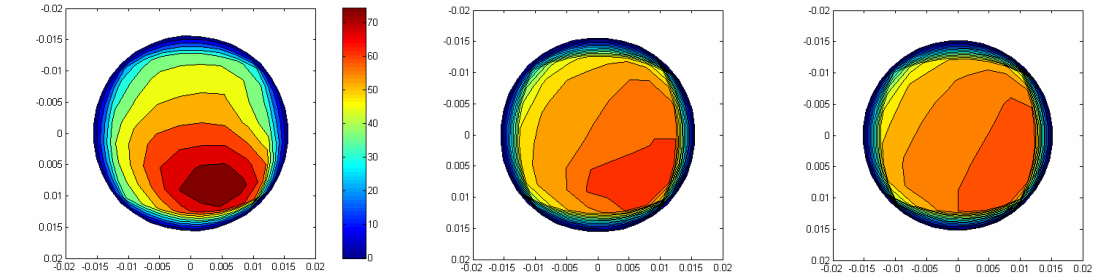

T=171 ms

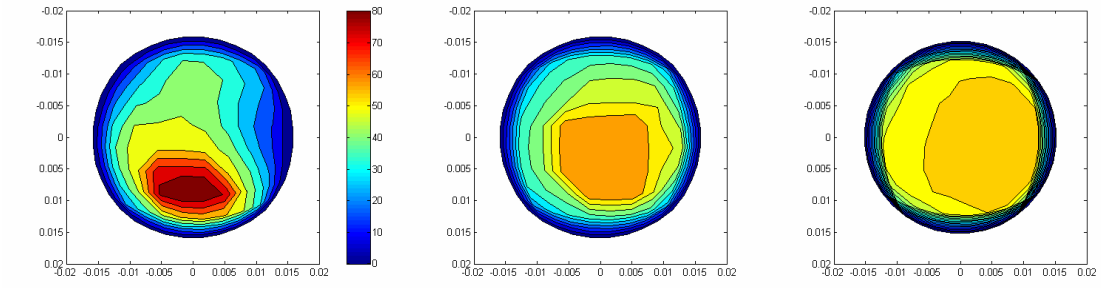

T=228 ms

Figure 4.7: Axial velocity distribution at the middle section - from the left to the right: PC-MRI slices; full wall motion; only radial wall motion (compliance effects); rigid wall. The velocity scale of the color bars is cm/s.

Compliance and movement Compliance Rigid

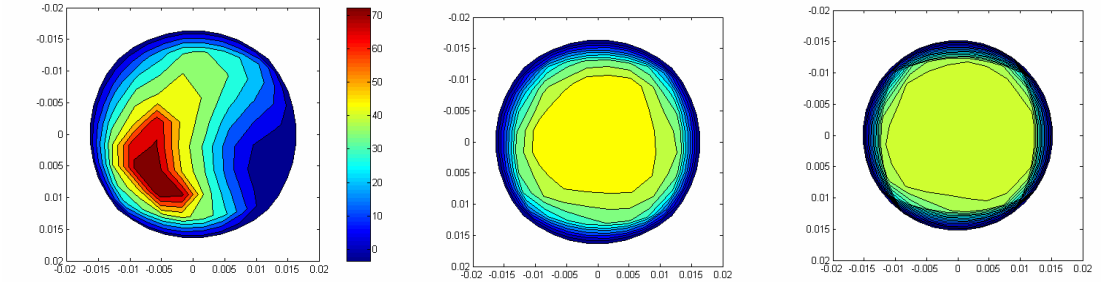

T=285 ms

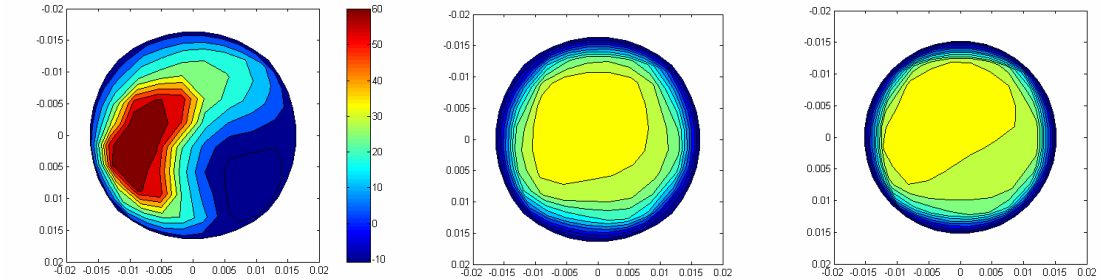

T=342 ms

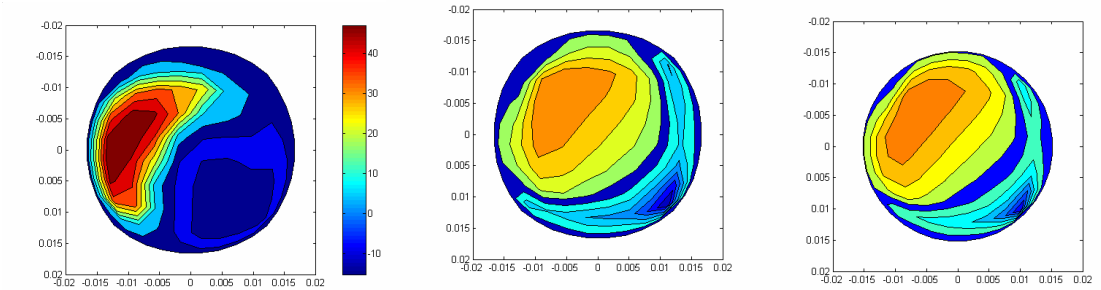

T=399 ms

Figure 4.7: (continued)

Compliance and movement Compliance Rigid

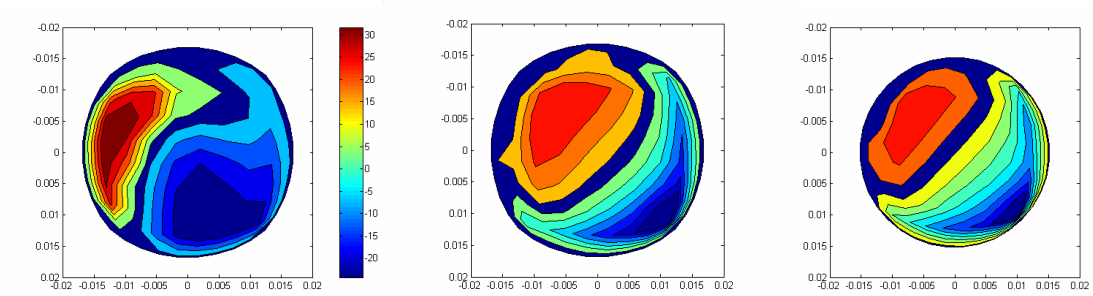

T=456 ms

Figure 4.7: (continued)

orientation, as illustrated in Figures 4.4 and 4.5. The axial velocity magnitude was coded by color and the units are centimeters per second, and the velocity distributions of the three models at each time are shown in the same rows. Note that the color scale is not the same at different times.

In Figure 4.7, the panels from left to right are presented according to the following scheme: the 1st column – Model 1, axial velocity computed assuming full wall motion; the 2nd column – velocity color bar that suits all models at the time, the units are centimeters per second; the 3rd column – Model 2, axial velocity computed assuming only radial wall motion (compliance effects); and the 4th column – Model 3, axial velocity computed assuming a motionless, rigid vessel wall.

The CFD velocity from Model 1 (first column) shows a very similar velocity distribution as the PC-MRI velocity (see the left column in Figure 4.5). The peak velocity position rotated clockwise from the left posterior side of the lumen at 114 ms to the right anterior side at 399 ms. The locations of the peak velocity at times t = 114, 171, 228, 285 and 342 ms were in good agreement with the PC-MRI data.

In addition to the location of peak velocity, the CFD velocity color contours in the first column and the PC-MRI color pixels in Figure 4.5 had approximately the same velocity ranges. For example, the maximum velocity was slightly more than 63 cm/s at 114 ms in the PC-MRI data, and the maximum velocity was 65 cm/s in the CFD results. The maximum velocity was 50 cm/s and the minimum velocity was –10 cm/s at 399 ms from PC-MRI, and the maximum and the minimum velocities were also 50 cm/s and –10 cm/s in the CFD results.

At 456 ms, in the diastolic period, the maximum axial velocity reduced to less than 20 cm/s in both the CFD and PC-MRI data. In the later diastolic period, there is less agreement between the PC-MRI and CFD results, with the PC-MRI data presenting a more nonuniform distribution. This difference may be due to the fact that the PC-MRI signal-to-noise ratio became lower when the absolute velocity magnitude became smaller during diastole.

A comparison of all columns in Figure 4.7 shows that during the acceleration phase at 114 ms, the peak velocity position is located in the left posterior position of the lumen in all three CFD models. However, at later times (171, 228 and 285 ms), the peak velocity positions in Model 2 (3^{rd} column) and Model 3 (4^{th} column) seem to move directly across the lumen, rather than rotating along the posterior wall, as with the PC-MRI data.

During late systole the locations of the peak velocity region of the three CFD models were in agreement again, i.e., located at the right anterior side of the lumen. However, differences in the velocity distributions and ranges of values among the three CFD models were seen, especially for regions of low and negative velocity. It appears that the computational model that incorporated both compliance and wall movement presents the best results by comparison with the PC-MRI *in vivo* data, and thus, Models 2 and 3 fail to capture faithfully the right hand helical flow behavior observed *in vivo* during systole. We conclude that it is necessary to model the overall aortic motion.

4.3 Wall Shear Stress (WSS) in the Aorta

There is interest in hemodynamic wall shear stress (WSS) and the possibility that mechanical stresses acting on the artery wall can affect its function, particularly as related to the development and rupture of atherosclerotic plaques. WSS can be computed from the velocity gradient near the vessel surface, but its measurement *in vivo* is not accurate except perhaps in very special and simple circumstances. Thus, no *in vivo* data for this variable are available for comparison with computed results. Furthermore, small errors in describing the model surface, derived from imperfect MR images, lead to larger uncertainties in WSS estimations than in velocity itself.

Figure 4.8 shows an example of WSS results that came from another model among the four aorta models developed in the study. In the figure the magnitude of WSS was coded by color, and the color bar in the right of the figure shows the color scale with units of dynes per square centimeter. Five WSS distributions occurring at five times are shown in the Figure. The upper left Figure in Figure 4.8 shows the flow waveform in the aorta, which is used as the reference time for the WSS distributions. Time was normalized by the cardiac cycle time.

Since our modeling emphasized the ascending aorta where the walls are compliant and moving, the interest on WSS was also focused on the ascending aorta. The magnitude of the WSS changes with time and flow. The peak values of WSS occur at time t = 0.2, which is the peak flow time in the aorta (See the upper left panel in Figure 4.8.). At this time, the largest WSS is concentrated along the sharp bending region of inner curvature of the ascending aorta. As we know from the study, the flow is skewed along the inner curvature during this time (See the streamlines at 114 – 228 ms in Figure 4.6.), and the

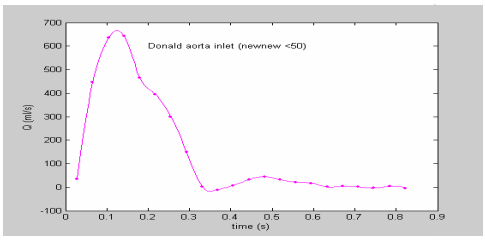

Time
0.1

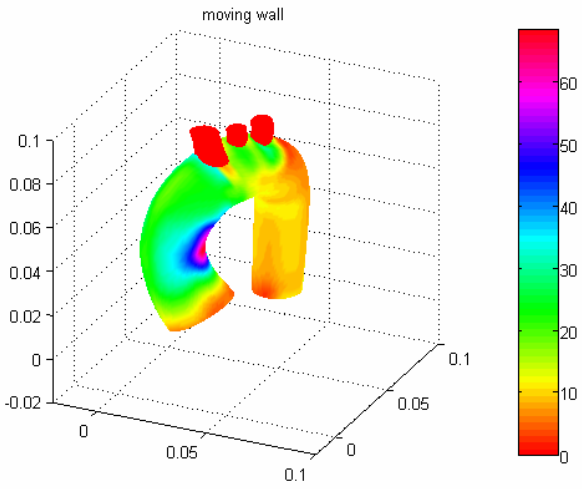

0.2

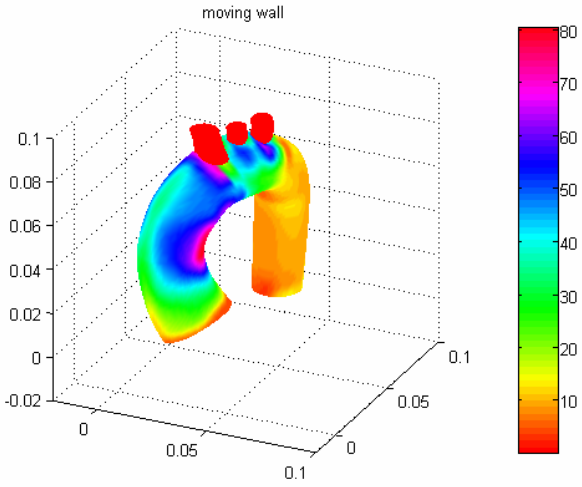

0.3

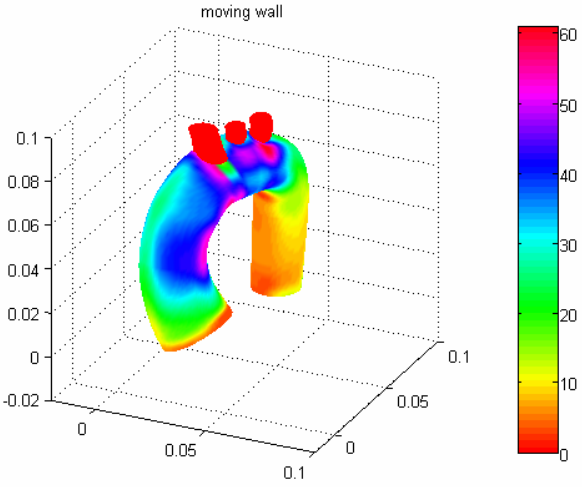

Figure 4.8: Wall shear stress (WSS) distribution with units dynes per square centimeter. The flow waveform shows the time background where the time was normalized.

0.4

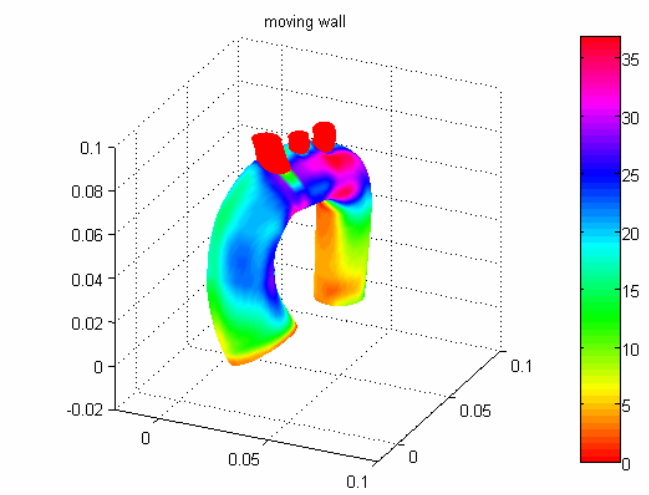

0.5

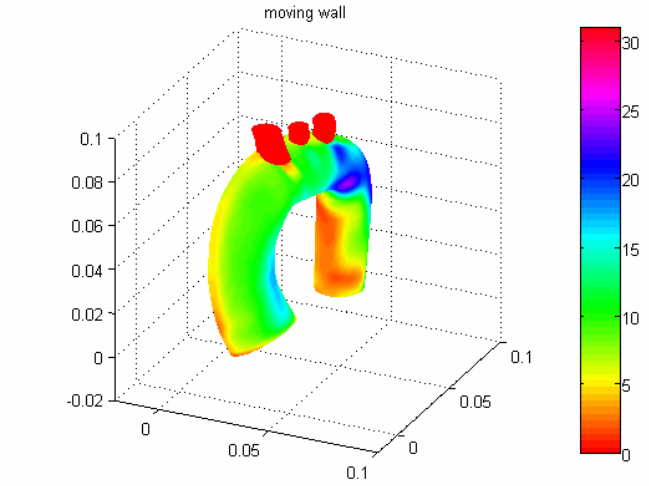

Figure 4.8: (continued)

sharp bend of the lumen enhances the WSS values. The mean value of WSS is about 30 dynes per square centimeter in most regions of the ascending aorta during systole (See the WSS at t = 0.1, 0.2 and 0.3 in Figure 4.8.), although the maximum WSS may reach as high as 80 dynes per square centimeter (e.g., t = 0.2).

In diastole, the WSS magnitudes are reduced as the flow rate diminishes. In most of diastole, all WSS values are less than 15 dynes per square centimeter in the ascending aorta.

This study showed that the compliance and motion of the lumen of the ascending aorta are significant in their effects on blood flow patterns. Thus, a useful question is how the compliance and motion of the lumen affect the WSS in the ascending aorta. Since we performed calculations using a rigid model (Model 3, Chapter 4.2), we can compare the WSS in the two models. Except for wall motion, all other geometrical and boundary conditions are the same in the two cases.

Figure 4.9 shows the WSS distributions in the rigid wall model that is the same model as in Figure 4.8 but where the wall structure was fixed at t = 0. In the peak flow time, t = 0.2, the WSS with rigid walls can exceed 105 dynes per square centimeter, which is approximately 25 dynes per square centimeters greater than the model with the moving wall (See Figure 4.8). In systole, t = 0.1, 0.2 and 0.3, the WSS in the rigid wall model averaged approximately 20 dynes per square centimeter more than the WSS in the moving wall model, or a 25% relative increase. The overall characteristics of the WSS distributions did not differ notably between the models. In diastole, at t = 0.4, the WSS in the rigid wall model is about 5 dynes per square centimeter greater than the WSS in the moving wall model, but in the remaining time of diastole both models presented similar

Time

0.1

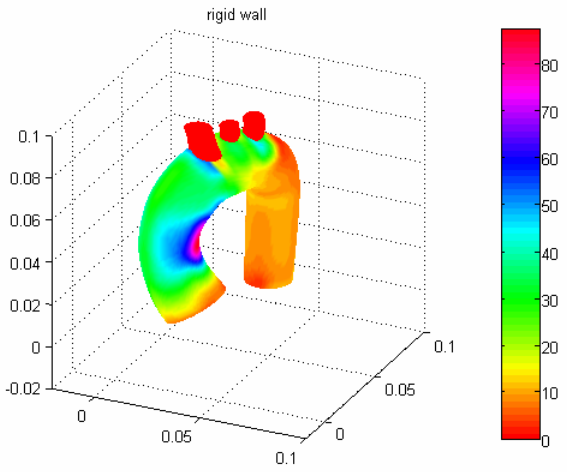

0.2

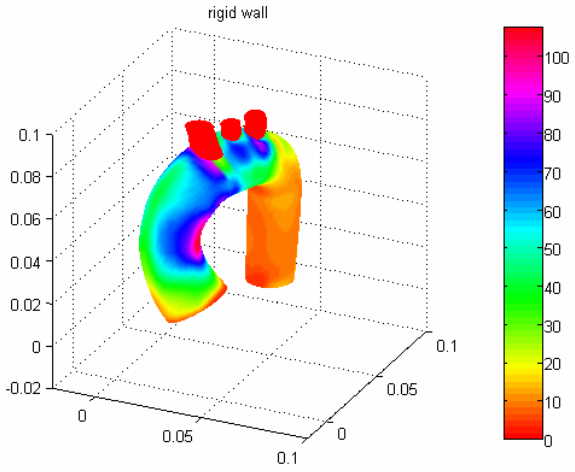

0.3

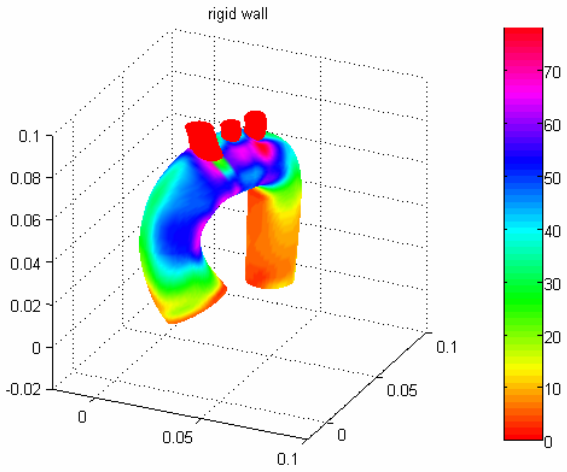

Figure 4.9: Wall shear stress (WSS) distribution in the model that had rigid walls. The units of WSS are dynes per square centimeter. The time is same as in Figure 4.8.

0.4

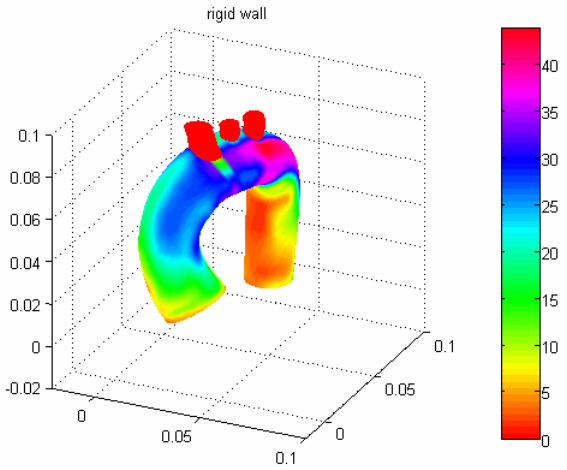

0.5

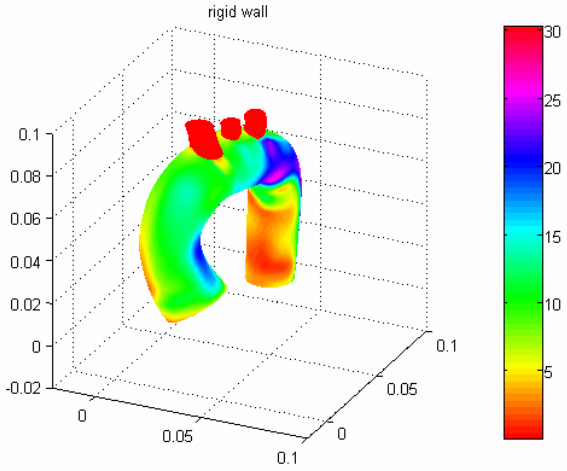

Figure 4.9: (continued)

values of WSS. Since the diameter of Model 1 is greater than that of Model 3 during systole due to expansion arising from intramural systolic pressures, it would be expected that the WSS in Model 3 would be greater; whereas during the lower pressure period of diastole, the diameters – and hence the WSS values – should be similar for the two models.

This study illustrates that the compliance of the aortic wall acts like a flow buffer to moderate the absolute values of WSS in the ascending aorta.

4.4 Entrance Blood Flow Patterns in the Coronary Arteries

As the aorta CFD modeling showed, a dynamic helical flow pattern occurs in the ascending aorta, and this flow would be expected to strongly affect the entrance flow conditions in the coronary arteries. Coronary artery entrance flow effects have not been explored until now because the geometry and flow conditions of the arteries are very complex. A combined model of the aorta and coronary arteries has been reconstructed in this study (see Chapter 3.4.3). Because we lacked velocity information in the small branches of the coronary arteries, the CFD modeling was limited in the major trunks of RCA, LAD and LCX.

The 3D flow velocity patterns in the entrance segments of the right and left coronary arteries computed from the CFD models are shown in Figure 4.10. Figure 4.10 (a) presents the geometry of the model and indicates stations in the LCA and RCA where velocity results will be presented. Axial velocity profiles and in-plane velocity distributions are used to represent the 3D velocity patterns. Figure 4.10 (b) shows the results at t = 0.2 (See Figure 3.24) where the upper left image presents the axial velocity

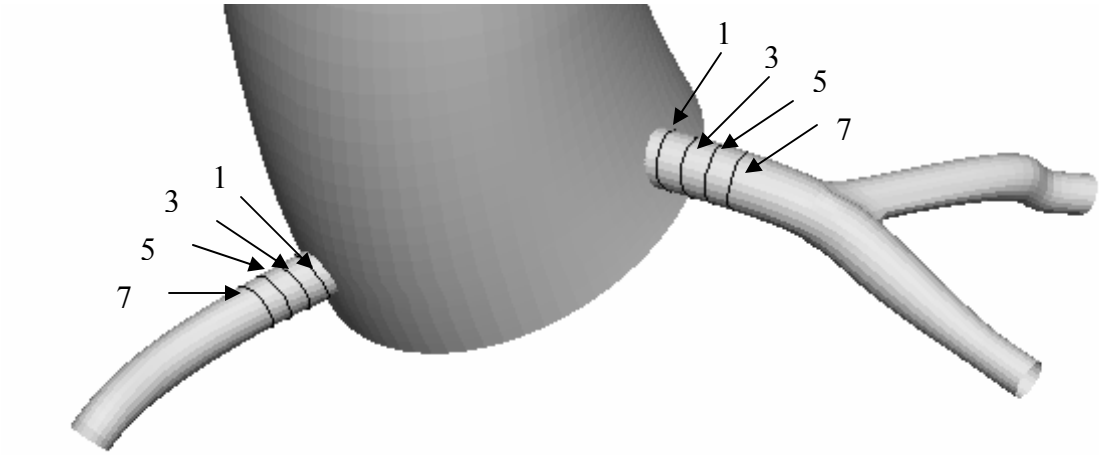

Figure 4.10 (a): Position of the sections - distances to the aortic orifice.

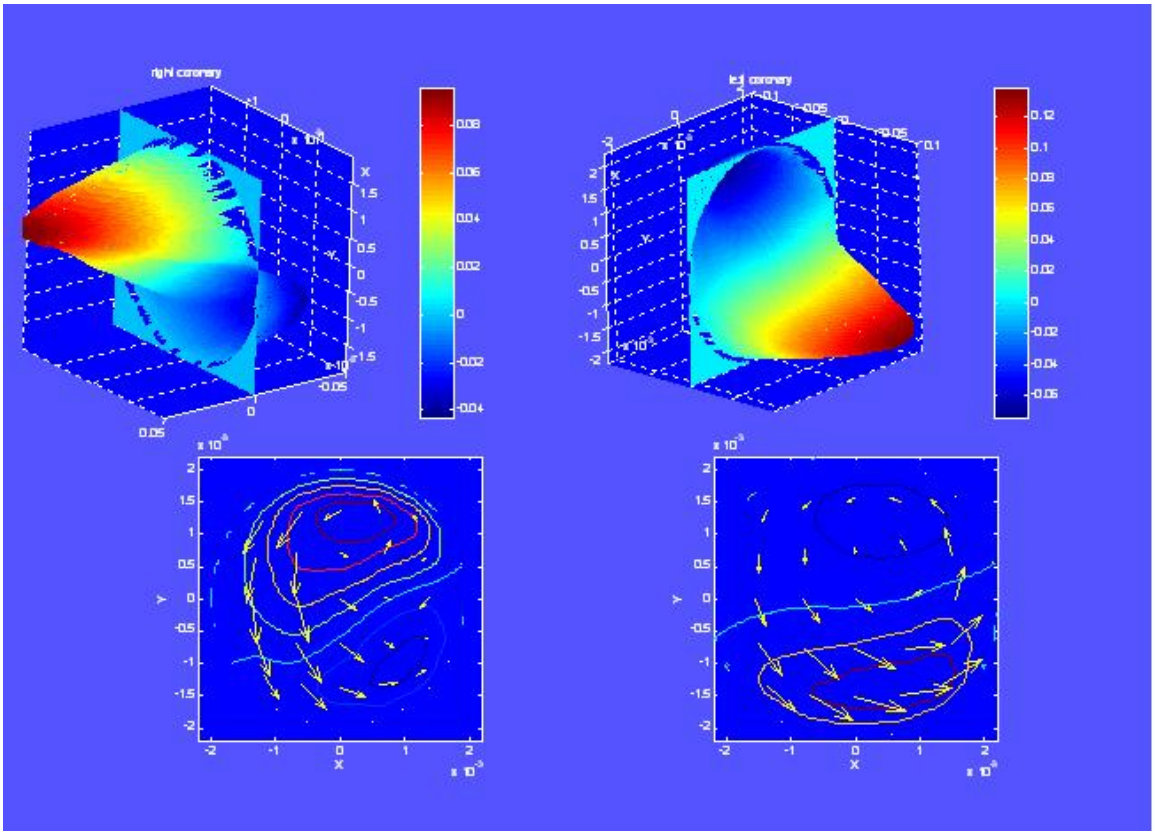

Right coronary artery Left coronary artery

Figure 4.10 (b): The axial velocity profile, and in-plane 2D velocity contours and vectors in the orifice sections at time 0.2 (see Figure 3.24).

profile in the right coronary artery in the aortic orifice section. The velocity magnitudes are coded by color in the image. The lower left image of Figure 4.10 (b) shows the in-plane 2D velocity contours and vectors. The vectors show the 2D velocity directions, and their lengths are proportional to the velocity magnitude. The right two images of Figure 4.10 (b) are the same as the left hand images, but are for the left coronary artery.

Figure 4.11 presents the axial velocity profiles, which demonstrate the dynamic nature of the velocity field. Each row shows four velocity profiles at a specific time, and these velocity profiles came from four transverse sections as indicated by the arrows in Figure 4.10 (a). The numbers in Figure 4.10 (a) express the distances in millimeters from the aortic orifice to the individual sections. Figure 4.11 (a) shows the velocity profiles in the right coronary artery at three times, t = 0.15, 0.3 and 0.45 (see Figure 3.24), while Figure 4.11 (b) presents the velocity profiles in the left coronary artery at the same times.

Certain flow characteristic can be observed from Figure 4.11. The axial velocity profiles in Figure 4.11 describe two strong axial vortices that occur in the entrance sections of the right and left coronary arteries individually during systole. The intensity of the axial vortices is a maximum in the aortic orifice and quickly diminishes as one enters the coronary arteries. During systole there is little net flow into the coronaries, so it is the aorta flow that is the main cause of the specific vortices.

A potentially significant finding is that the rotational directions of the axial vortices differ between the right coronary artery and the left. In the aortic orifice of the right coronary artery, fluid enters the artery along the epicardial side and some fluid returns to the aorta along the myocardial side during the systolic phase. On the other hand, in the

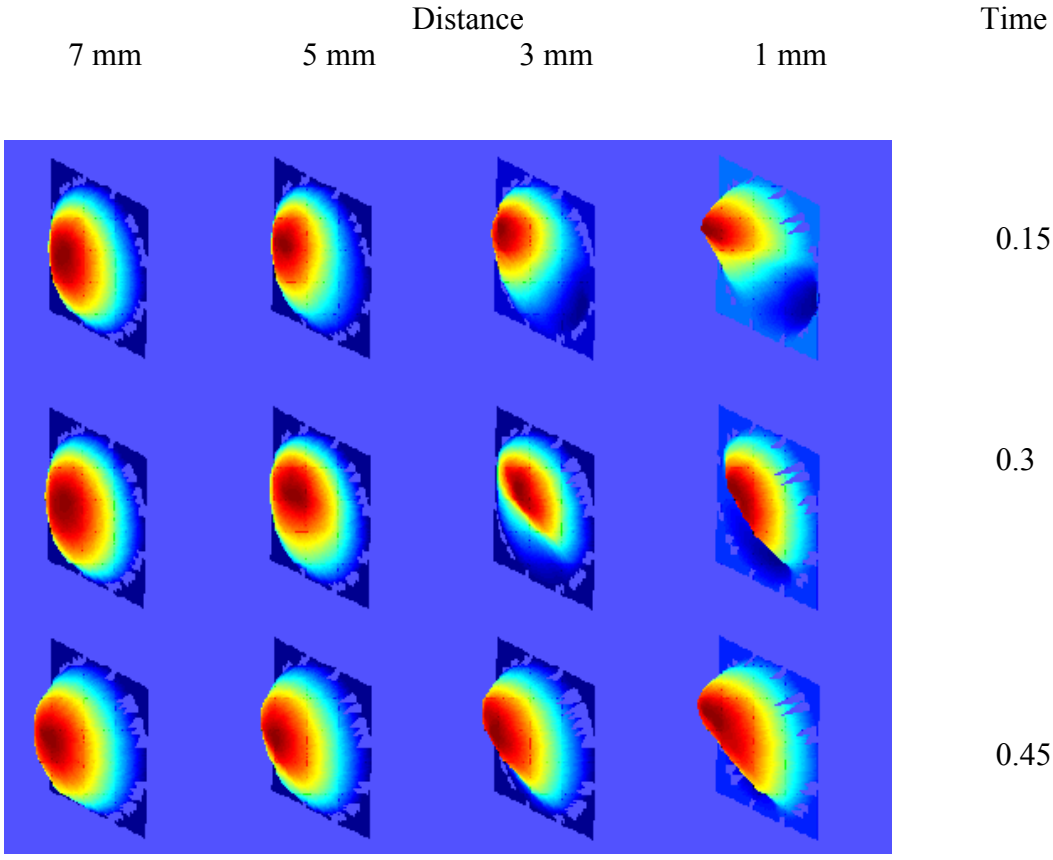

Figure 4.11 (a): Axial velocity profiles in the sections of the right coronary artery.

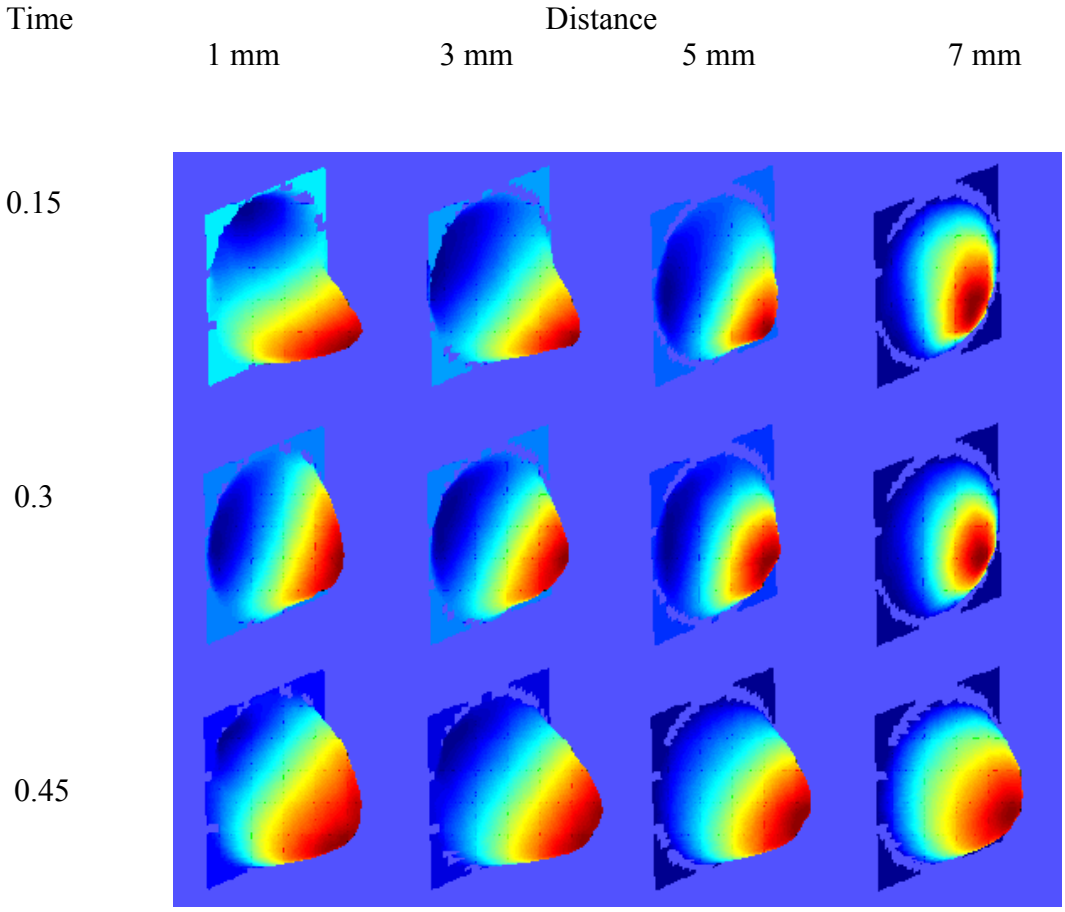

Figure 4.11 (b): Axial velocity profiles in the sections of the left coronary artery.

left coronary artery, fluid enters along the myocardial side and returns to the aorta along the epicardial side during most of systole. The intensity of the axial vortices in the entrance sections reaches the greatest level during systole (the aortic valve closes at t = 0.4), and then the vortices generally disappear. The velocity profiles become fairly symmetrical as the net flow into the coronaries increases. The positions of the entrance vortices are limited to a distance of about 1.5 times the diameter of the artery from the aortic orifices; and the nearer the location to the orifices, the stronger is their intensity. Each vortex in the right and left coronary arteries appears to be driven by the pulsatile flow patterns in the aortic root during systole. It is the specific flow patterns in the aorta that cause the vortices to have different rotating directions. The vortical flow patterns create a low and oscillatory wall shear stress region on the myocardial side in the entrance segment of the right coronary artery, but on the epicardial side in the entrance segment of the left coronary artery.

Are these entrance flow patterns specific to this individual or are they perhaps common for different persons? Figure 4.12 presents another result that came from another model at the same positions and times as shown in Figure 4.11s (a) and (b). The second model was reconstructed by the same methodology as the previous model, but came from another healthy subject. Comparing the axial velocity profiles between in Figure 4.11 and in Figure 4.12, the two CFD models that came from individuals with different geometrical sinuses of Valsava and different aortic inlet velocity distributions present very similar dynamic flow patterns in the entrance sections of the right and left coronary arteries. While these represent only two subjects, the fact that similar entrance

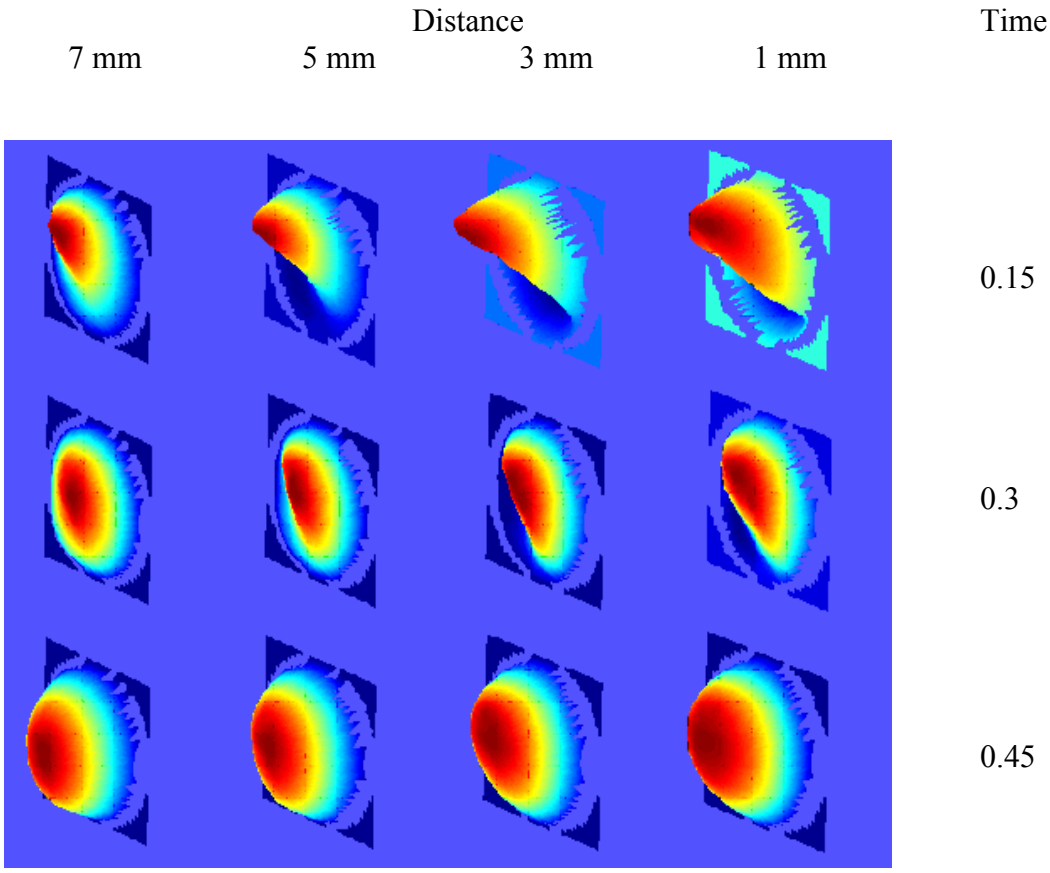

Figure 4.12 (a): Axial velocity profiles in the sections of the right coronary artery (Subject 2).

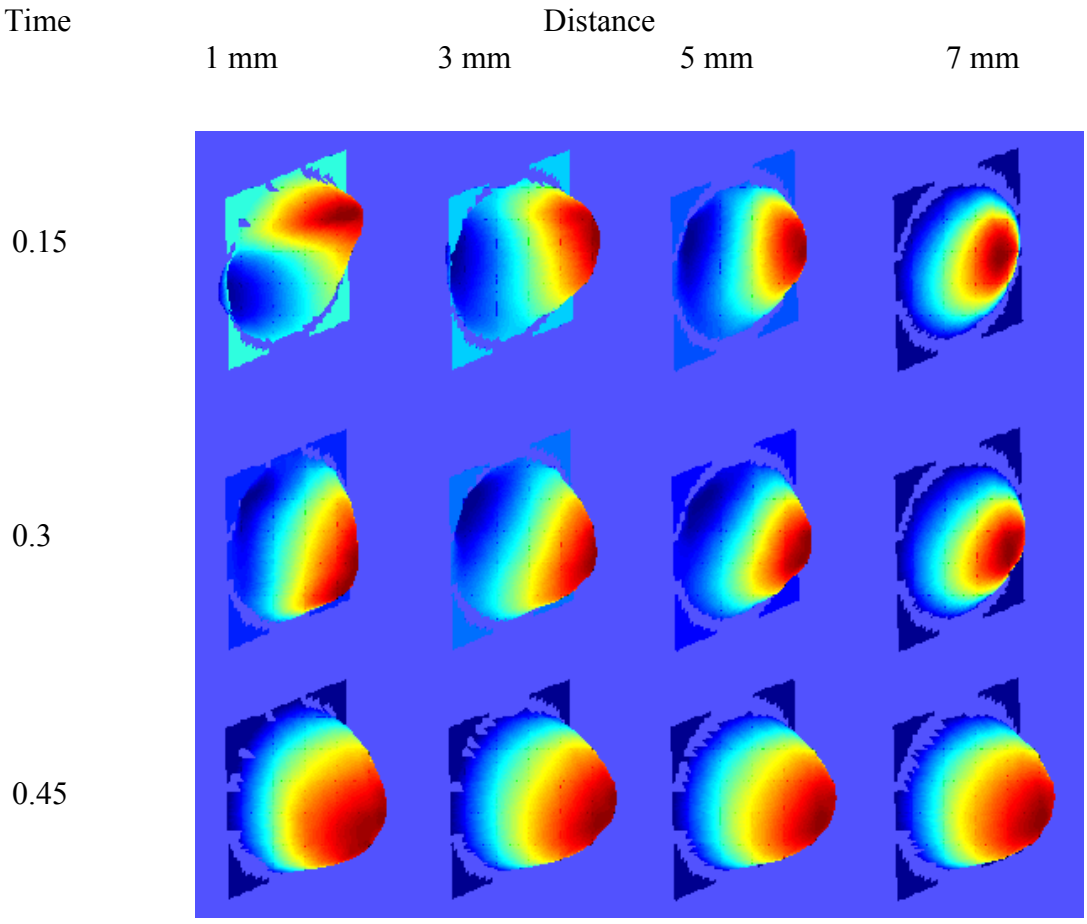

Figure 4.12 (b): Axial velocity profiles in the sections of the left coronary artery (Subject 2).

flow patterns are predicted for the coronary arteries leads us to hypothesize that these entrance vortices may be common.

To further verify the specific entrance flow patterns in the right and left coronary arteries predicted by the CFD modeling, PC-MRI coronary scans located at the coronary validation sections, as Figure 3.31 shows, were performed. Figure 4.13 (a) shows the axial velocity contours produced by the PC-MRI images across the right coronary artery at the three times shown in Figures 4.11 and 4.12. The image resolution in Figure 4.13 was 0.51 mm per pixel, but the slice thickness was 6 mm (A large slice thickness was required in order to achieve adequate signal to noise when attempting to obtain numerous pixels across the relatively small coronary artery lumen.). This means that each image in Figure 4.13 represents a velocity distribution that encompasses the first 2 or 3 velocity profiles in Figure 4.11 (or 4.12). In the images of Figure 4.13, the upper direction is the epicardial side of the heart and the lower is the myocardial side. The warm colors express a positive velocity direction that enters the coronary, and cool colors express a negative velocity.

Considering the limitations of PC-MRI, we focused our comparison on whether the velocities are positive (into the coronary artery) or negative (back to the aorta) in the lumen. As previously discussed, the computations predicted that during the early part of systole the (positive) flow entered the right coronary artery from the epicardial side of the heart and some (negative) flow moved back into the aorta from the myocardial side. Then, the positive flow gradually dominated the lumen in the latter phase of systole (See Figure 4.11 (a)). The PC-MRI observations, Figure 4.13 (a), show similar dynamic flow patterns as in Figure 4.11 (a). At t = 0.15 and 0.3, Figure 4.13 (a) shows the positive flow was in

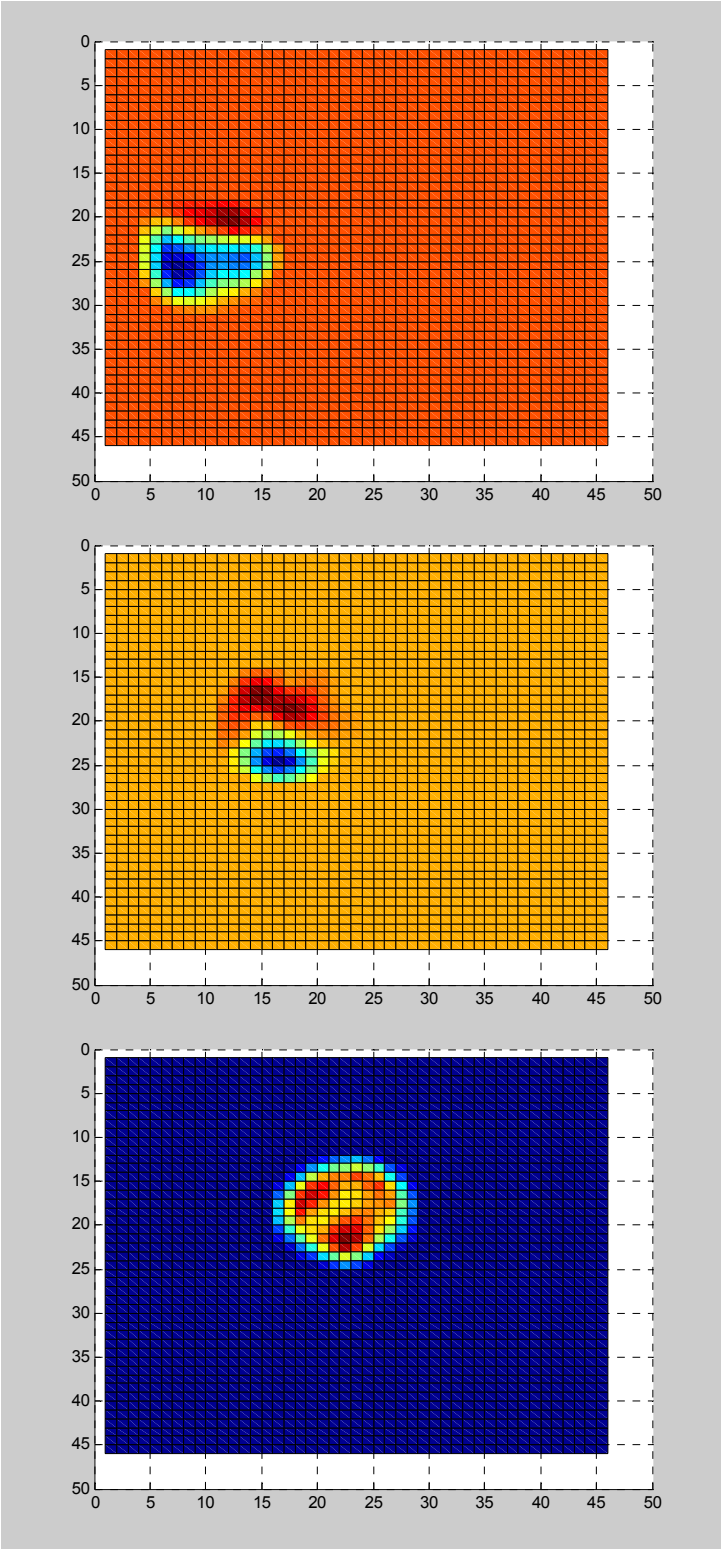

Figure 4.13 (a): PC-MRI axial velocity distribution of the right coronary artery.

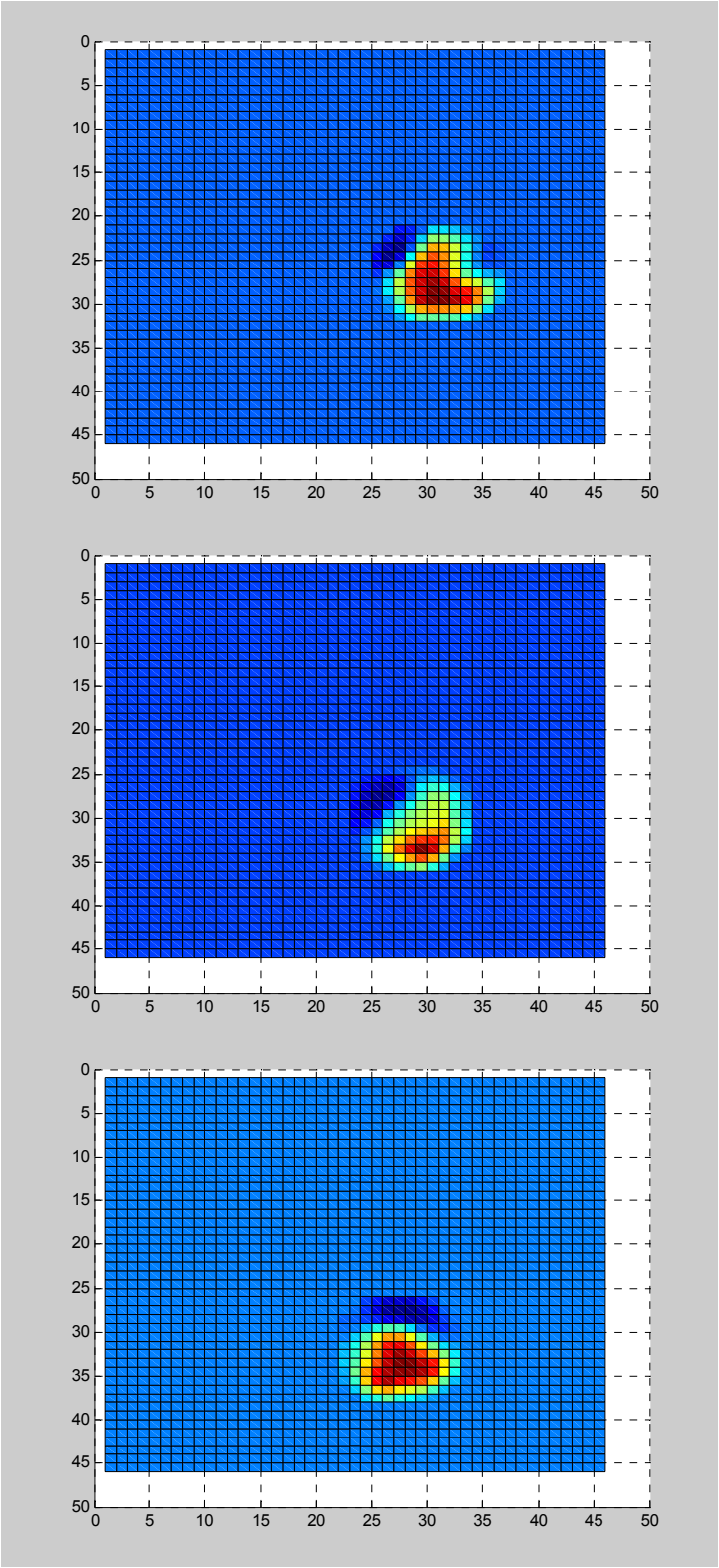

Figure 4.13 (b): PC-MRI axial velocity distribution of the left coronary artery.

the epicardial side and negative flow was in the myocardial side. At time 0.45, the negative flow disappeared and positive flow dominated the lumen. This dynamic flow pattern in the entrance segment of the right coronary artery agrees with the CFD modeling predictions (Figure 4.11 (a)).

In the left coronary artery, Figure 4.13 (b), the positive flow favors the myocardial side at t = 0.15, and the negative flow appears at the epicardial side during systole. These dynamic flow patterns are also similar to the CFD results in Figure 4.11 (b).

Here, although the validations of flow patterns in the coronary arteries using the characteristics of the velocity profile are more qualitative than quantitative, the velocity profiles that have distinctly eccentric features coming from PC-MRI observation *in vivo* demonstrate that the specific entrance velocity patterns predicted by CFD are realistic.

4.5 WSS in the Coronary Arteries

Wall shear stress (WSS) in the coronary arteries as calculated by CFD was related to the flow patterns in the lumens. The WSS distribution in the right coronary artery is shown in Figure 4.14 where the units of the WSS are dynes per square centimeter. A high WSS region produced by the entrance flow patterns is located on the epicardial side in the initial section of the right coronary artery during systole and early diastole, and a low WSS region (< 6 dynes per square centimeter) is located on the opposite myocardial side in all times in the cardiac cycle. The asymmetrical WSS around the circumference of the lumen in the initial segment of the right coronary artery gradually becomes symmetrical during later of diastole. The asymmetrical WSS distribution was produced by the dynamic flow patterns in the aortic root originally.

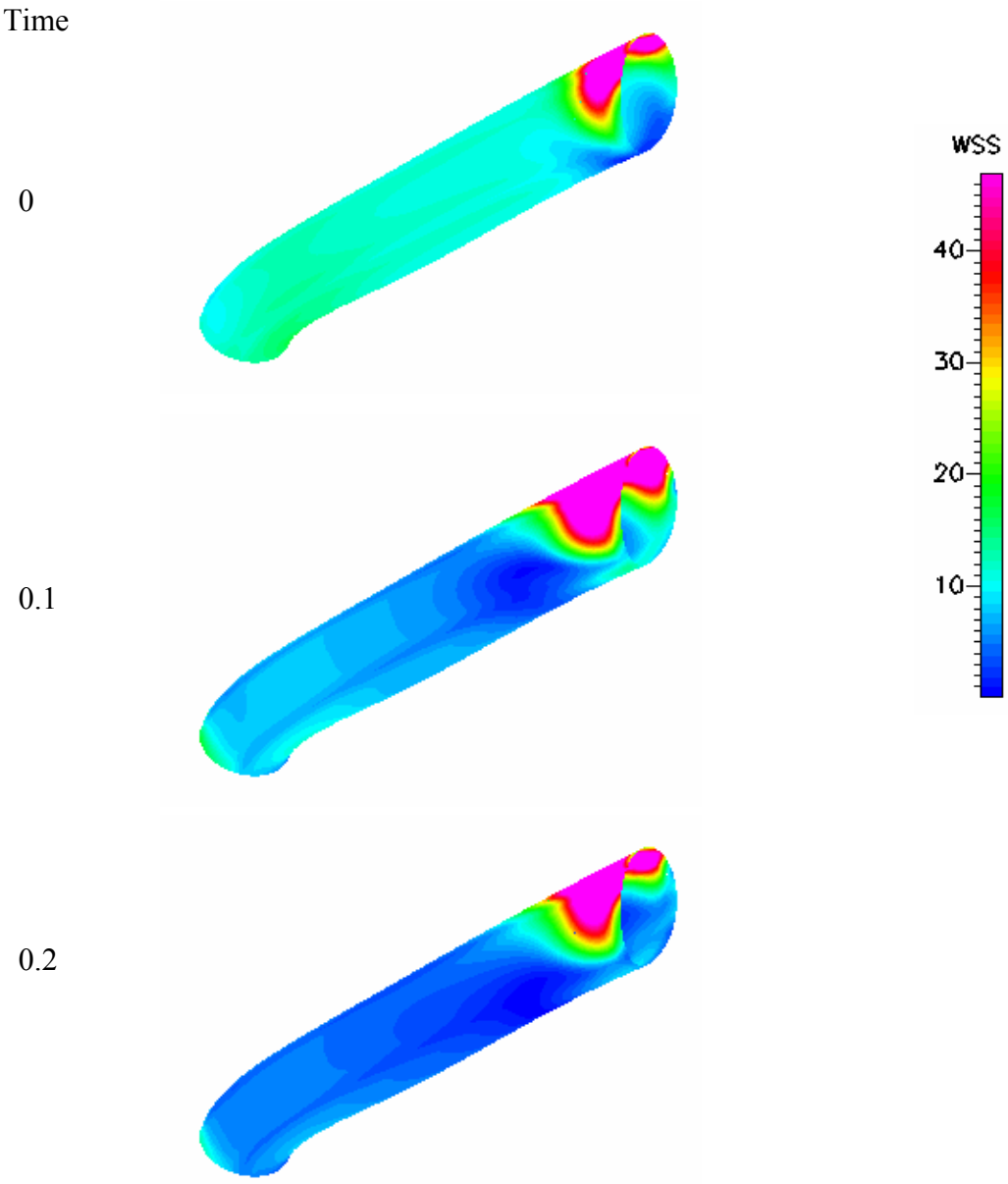

Figure 4.14: Wall shear stress distribution in the right coronary artery. The units of the WSS coded by color are dynes per square centimeter. The time is fractions of the cardiac cycle (see Figure 3.24).

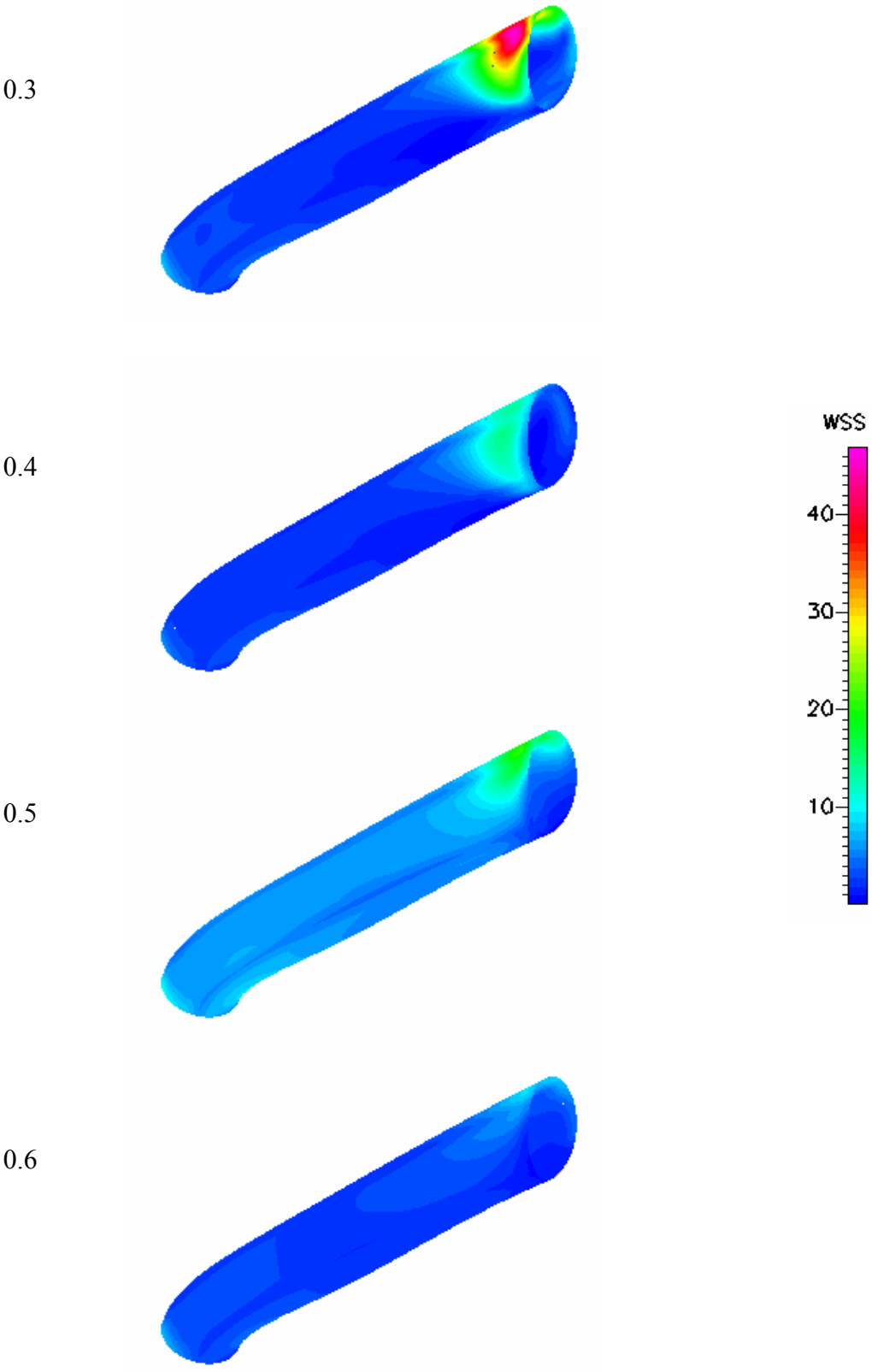

Figure 4.14: (continued)

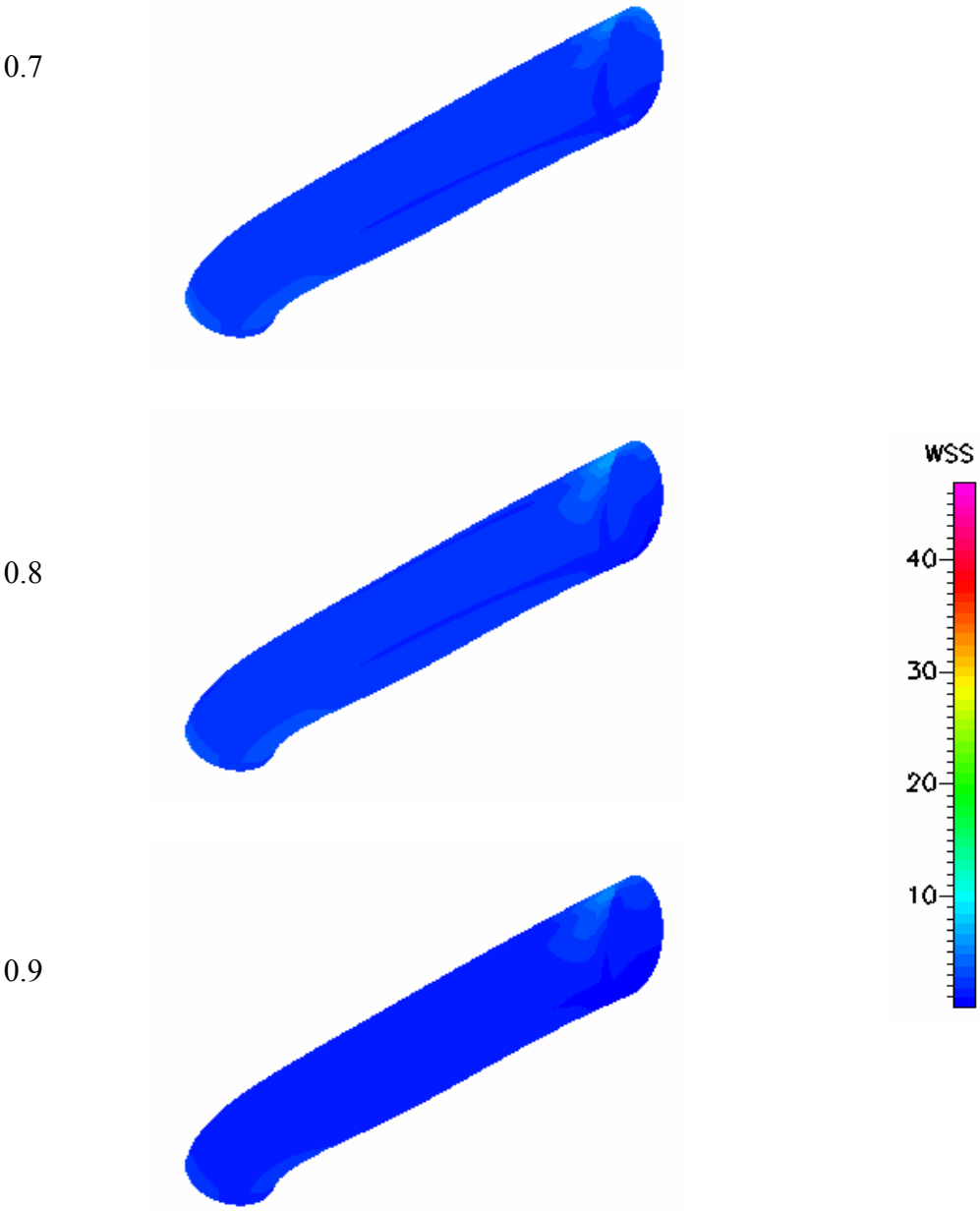

Figure 4.14: (continued)

In contrast, the high WSS regions in the left coronary artery are located on the myocardial side in the initial sections of the vessel (see Figure 4.15) in systole, and a low WSS region is located on the opposite epicardial side for most of the time, although these regions are more variable than those in the right coronary artery. This phenomenon also corresponds to the specific entrance flow patterns in the left coronary artery that were presented previously from the CFD modeling.

Of potential significance is the fact that the characteristics of the low WSS distribution in the initial sections of the coronary arteries are very similar to the characteristics of atherosclerosis distribution published in clinical literature. The low WSS regions in the CFD modeling corresponded with the regions of high frequency of atherosclerosis in the clinical observations. For example, after investigating 50 autopsies of subjects dying of non-cardiovascular causes, Fox and Seed (1981) found that there is tendency for plaques to be concentrated in the myocardial side downstream from the orifice in the right coronary artery, but it is opposite in the left coronary artery (see Figure 2.5). Ojha, et al. (2001) observed a similar distribution of intimal and medial thickening in the right coronary artery from autopsies (see Figure 2.6) in that a higher frequency of thickening is located at the myocardial side in the proximal RCA.

Figure 4.15 shows the WSS distribution in the left coronary artery where two views from different spatial points represent the entire WSS distribution in the lumen. Two low WSS regions (< 6 dynes per square centimeter) can be observed at all times in the figures: the myocardial side of the bifurcation extending to both outer sides of the bifurcation, and the epicardial side near the aortic orifice. We have previously discussed the fact that the second region is produced by the specific entrance flow patterns. The first region is a

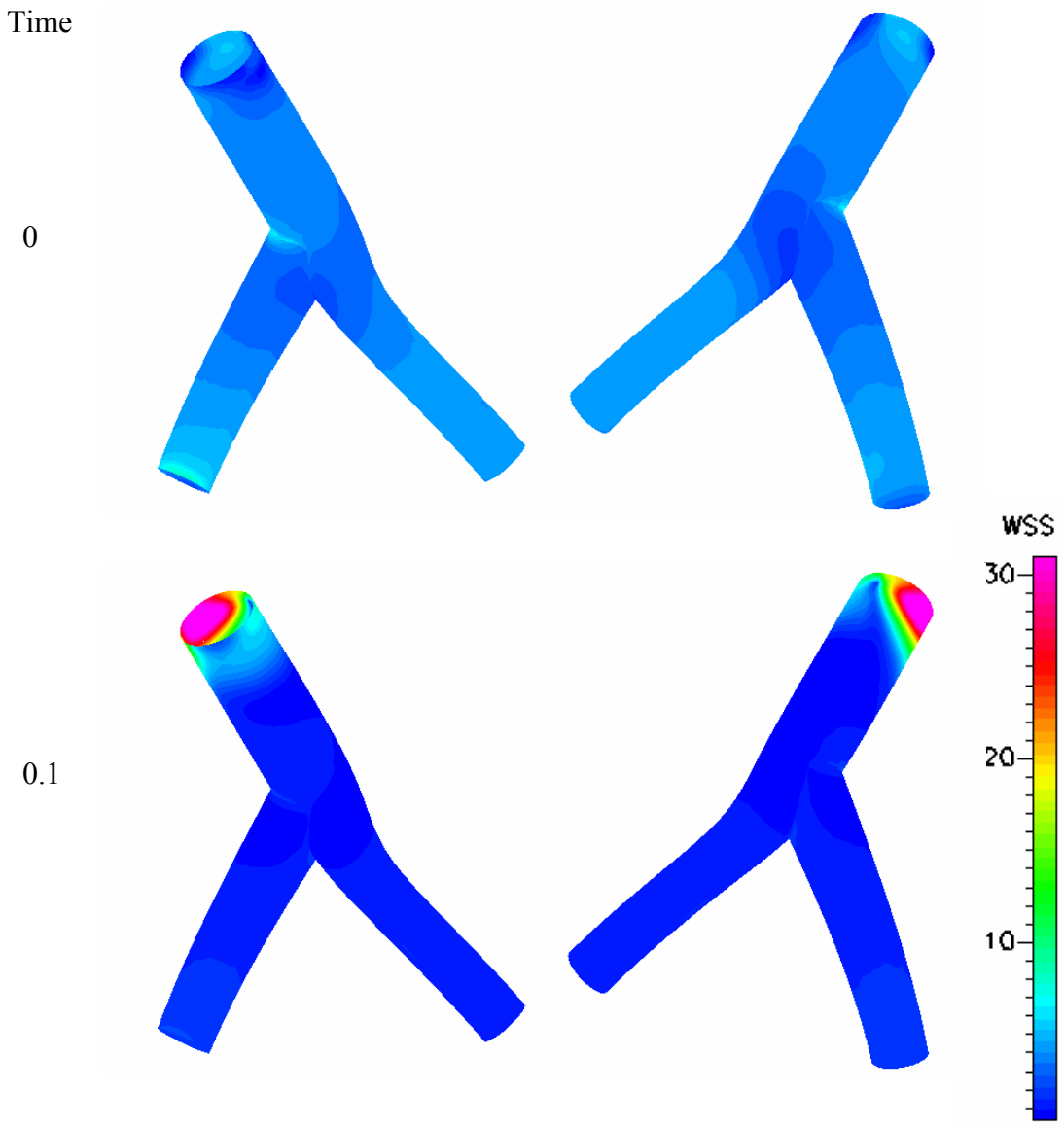

Figure 4.15: WSS distributions in the left coronary artery viewed from two different angles. The units of the WSS coded by color are dynes per square centimeter. The time is fractions of the cardiac cycle (see Figure 3.24).

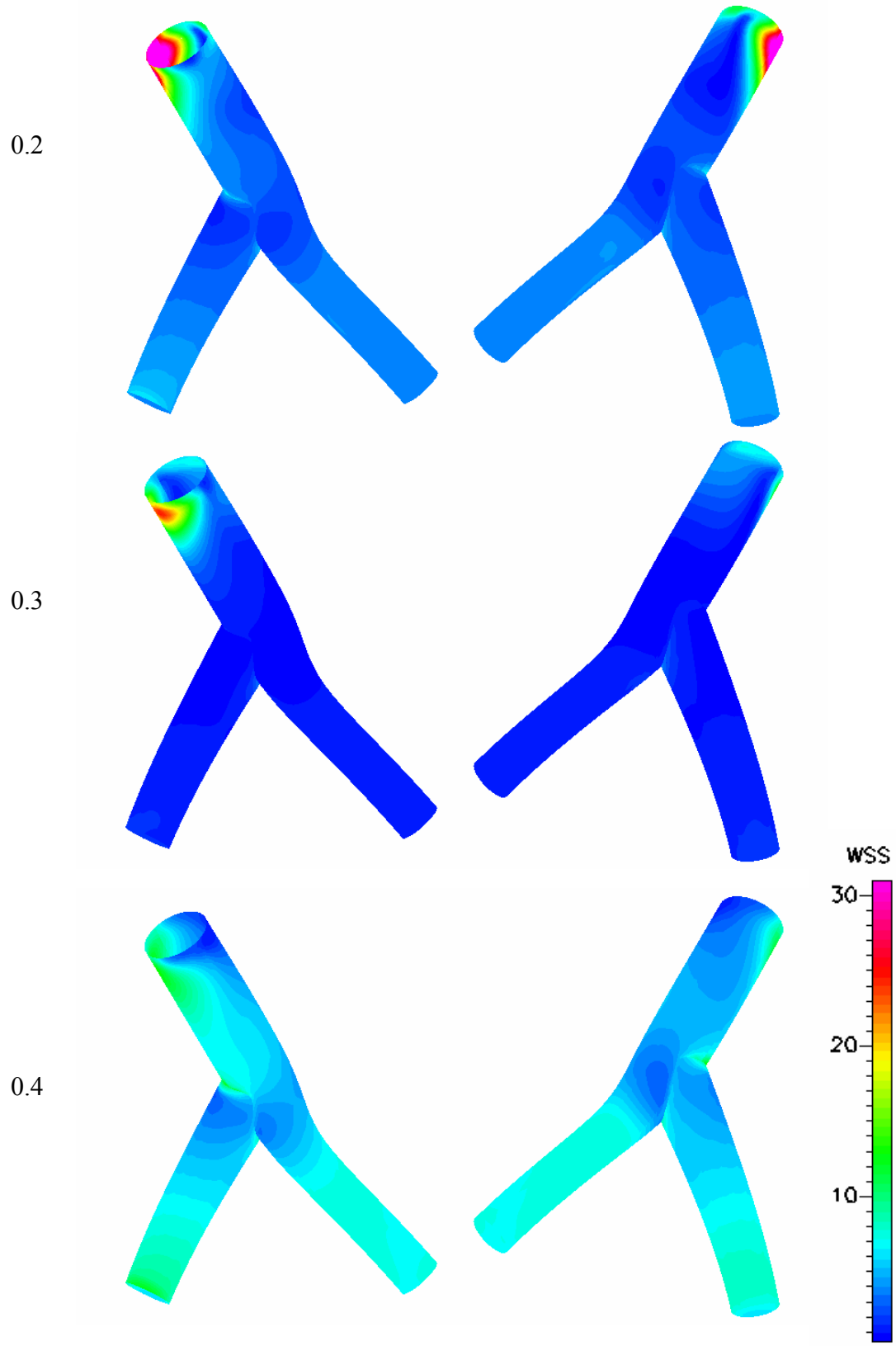

Figure 4.15: (continued)

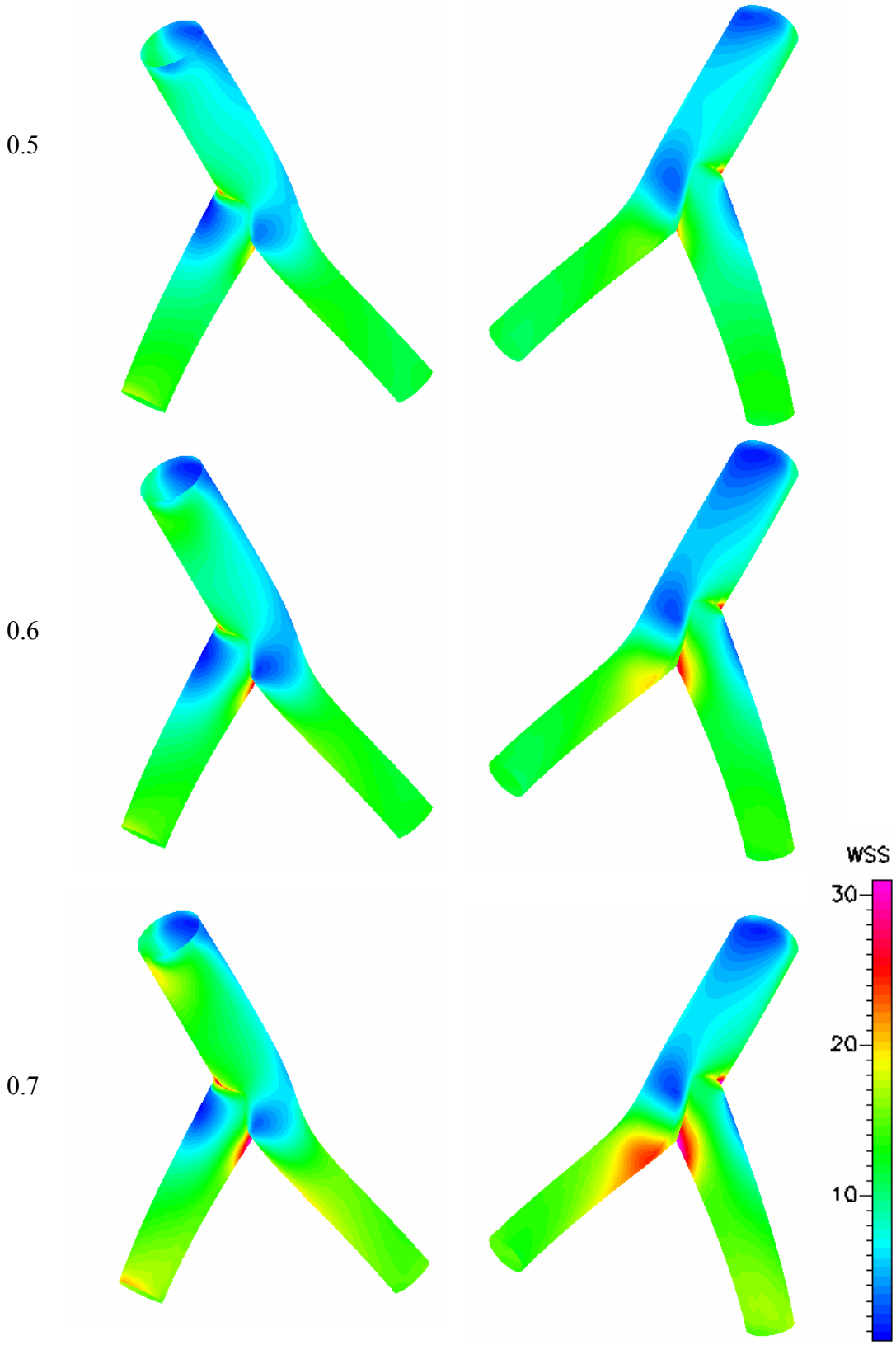

Figure 4.15: (continued)

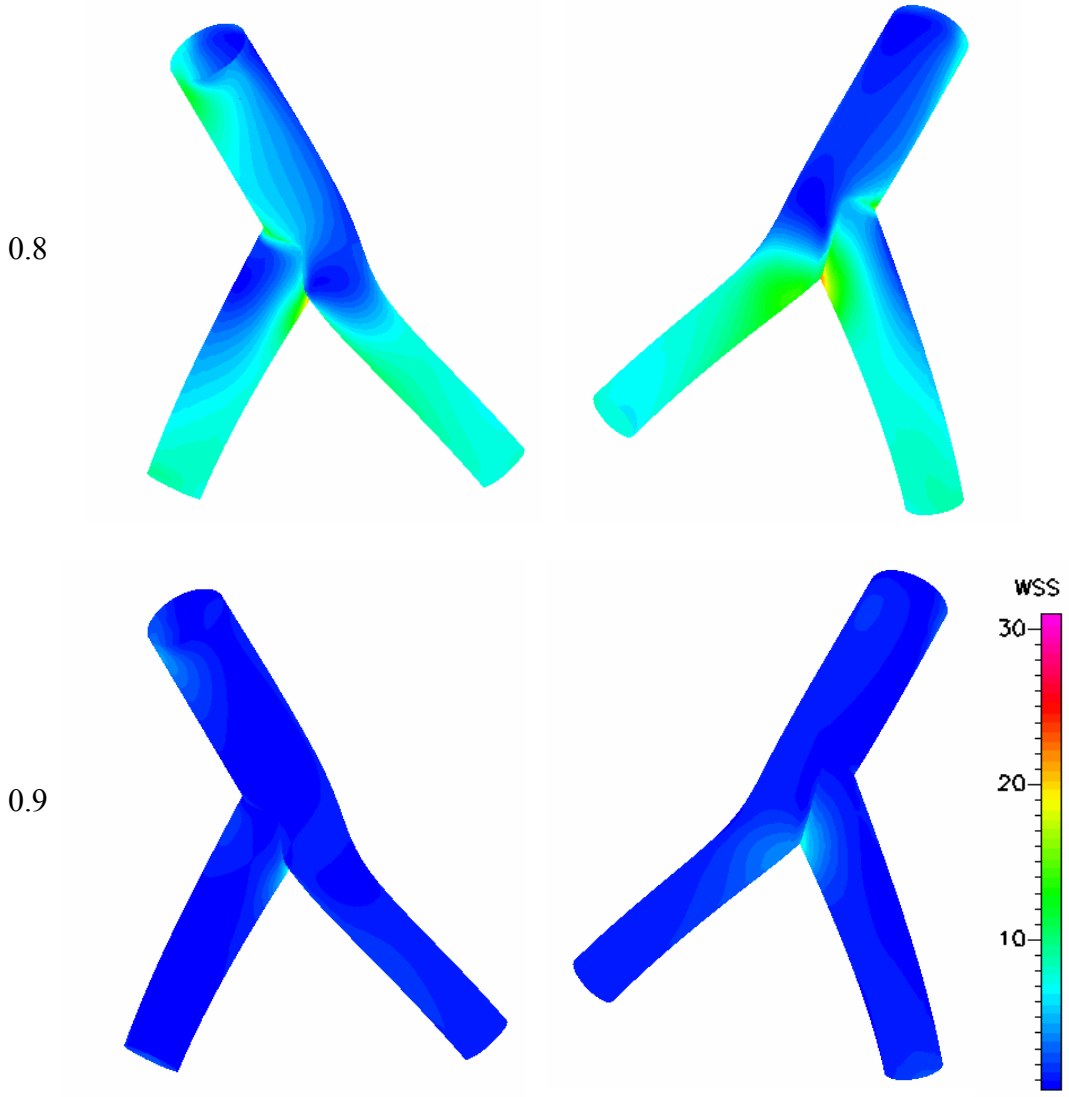

Figure 4.15: (continued)

favorite site for atherosclerosis as has been pointed out by clinical observations. For example, Svidland (1983) published the distribution of plaques in the left coronary artery from 41 autopsies, illustrated by contour lines connecting points with equal frequency of lesions (see Figure 2.8). The peak high frequency regions identified by Svidland are located on both outer sides of the bifurcation but more inclined to the myocardial side. This region corresponds to the first low WSS region in the CFD modeling.

The coincidence of the low WSS distribution and high frequency distribution of plaques in the coronary arteries supports the hypothesis that low and oscillating WSS contribute to atherosclerosis.

CHAPTER 5

CONCLUSIONS AND RECOMMENDATIONS

5.1 Methodology

Modeling the blood flow patterns in the ascending aorta was a procedure involving both CFD and MRI techniques. Some of the methods were adopted from other domains and some were developed as part of the study. The final modeling results successfully reproduced the complex right-hand helical flow patterns in the ascending aorta and were validated by clinical MR observations (Kilner et al., 1993) and PC-MRI scanning on the middle section (see Figure 4.5). This validation has given us confidence that the CFD/MRI combined method is a helpful platform and effective tool for exploring blood flow patterns in arteries.

Coronary arteries are one of the most attractive subjects for investigation. The CFD/MRI technique allowed us to predict specific flow patterns in the entrance segments of the right and left coronary arteries, and we used PC-MRI data to validate the existence of these predicted patterns, within the practical limits of resolution of MRI. Additionally, the comparison between WSS distributions produced by the CFD modeling and distributions of arterial disease reported in the clinical literature showed a good correspondence, which demonstrated that the methodology can be used to explore blood flow patterns in coronary arteries and to relate these to important clinical issues.

5.2 Helical Flow Patterns in the Aorta

The task of Specific Aim 2 in the study was to determine which factors contribute significant effects to the flow patterns observed *in vivo* in the ascending aorta. Previous studies placed emphasis on the geometric curvature, including twisted or non – planar curvature of the aorta (e.g. Kilner et al., 1993). These are indeed major factors because the overall geometry has great influence on details of the interior flow, and there have been a large number of fluid dynamic investigations of curved tube flows that demonstrate helical secondary patterns (e.g. Zabielski and Mestel, 1998). However, the aorta is not a simple coiled tube, and one would expect entry effects, pulsatility, details of inflow through the aortic valve, outflow through the arch vessels, and wall motion to be among factors that might also contribute to hemodynamic behavior in the aorta. Since flow fields are very specific to the particular geometry and boundary conditions imposed, we employed CFD/MRI techniques to model four healthy subjects. With such models, we could impose various assumptions in calculating the flow fields and then compare the results with independent PC-MRI velocity measurements taken within the computational domains. This comparison of velocity data sets then elucidated the relative importance of various factors.

Figure 4.7 illustrated the fact that the CFD modeling reproduced some of the key features of the flow in the ascending aorta. During the early phases of systole the high velocity jet emanating from the aortic valve was apparent and was located in the left posterior regions of the lumen. However, as systole continued, the PC-MRI measurements indicated that the zone of highest velocity migrated clockwise around the posterior side of the lumen, reaching the right anterior position at the completion of

systole. The rigid model results (Model 3) and those that included only radial motion due to compliance (Model 2) failed to reproduce this behavior. Including the observed translational movement of the aorta (Model 1), however, allowed the computations to predict *in vivo* behavior with good fidelity, not only with respect to the location of the high velocity jet but also the velocity magnitude. The presence of a large, axially elongated vortex during late systole and diastole is a feature that has received only limited attention; and as we subsequently demonstrated, this phenomenon has bearing on inlet effects for flow into the coronary arteries.

We conclude that curvature of the aorta, overall motion caused by the beating heart, expansion and contraction of the lumen during the cardiac cycle, and inflow created by blood ejection from the ventricle and interfered with by the aortic valve all contribute to the flow patterns in the ascending aorta. Significantly, however, we demonstrated that unless the aortic motion caused by the beating heart is included in the CFD simulations, important aspects of the flow patterns will not be obtained.

Figure 5.1 illustrates the interactions of the oscillating movement of the ascending aorta and the helical flow patterns in the vessel. In systole, the ascending aorta quickly moves along a right-hand rotation track (large black arrow in Figure 5.1) that can be seen in Figure 3.26 (b). This movement enhances the right-hand helical flow inside the lumen. In diastole, the ascending aorta slowly returns to its relaxed position (large blue arrow in Figure 5.1).

Figure 5.1: The oscillating movement of the ascending aorta causes the right-hand helical flow patterns in the vessel. In systole, the ascending aorta quickly moves along a right-hand rotation track (large black arrow). The movement enhances the right-hand helical flow inside the lumen. In diastole, the ascending aorta slowly returns (large blue arrow) to its relaxed position.

5.3 Entrance Flow Patterns in the Coronary Arteries

The possibility that aortic flow patterns may affect flow in the coronary arteries has been proposed by many clinical observers (e.g., Bogren et al., 1999). However, because of the resolution limitations of the *in vivo* measurements, the nature of these effects had not been previously determined. We applied the CFD/MRI methodology to simulate the entrance flow in models of the aorta that included the coronary arteries. The investigations revealed interesting specific entrance flow patterns in the initial segments of the right and left coronary arteries that are induced by the dynamic flow patterns in the aorta root.

Ideally, we would like to test the CFD predictions by carefully interrogating the velocity patterns in the coronary arteries with PC-MRI scanning *in vivo*, but resolution limits our ability to obtain these data. Within the achievable imaging resolution, however, the study does demonstrate that the asymmetrical entrance flow patterns predicted to occur in the right and left coronary arteries in systole and early diastole actually exist *in vivo* (see Figure 4.13 (a) and (b)). The computed flow patterns produce two different dynamic WSS distributions in the entrance segments of the right and left coronary artery. Figure 5.2 shows a sketch of the vortex structures that create a low and oscillating WSS region on the myocardial side in the right coronary entrance segment, and on the epicardial side for the left coronary entrance segment. Interestingly, these vortices rotate in opposite directions. Although these asymmetrical flow patterns occur only in later systole and early diastole, the low WSS (< 6 dynes per square centimeter) regions in the initial segments of the coronary arteries are predominantly on the myocardial side in the

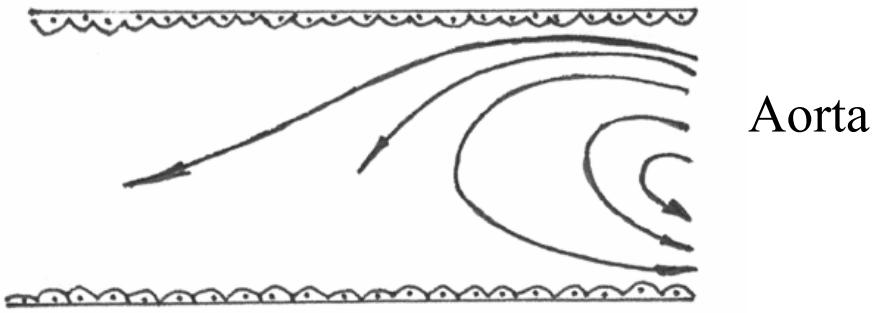

Figure 5.2 (a): Entrance blood flow patterns in the right coronary artery in systole and early diastole.

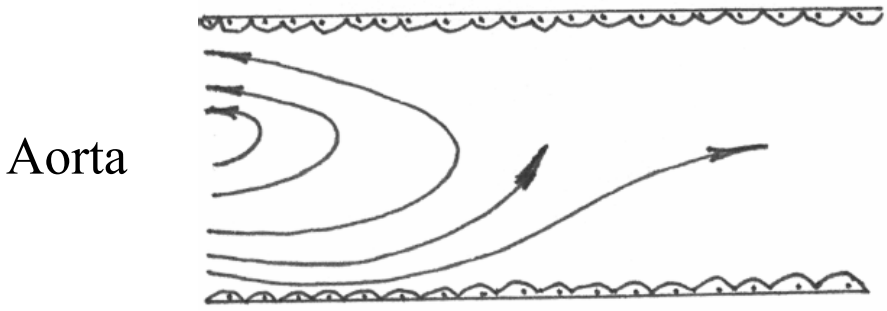

Figure 5.2 (b): Entrance blood flow patterns in the left coronary artery in systole and early diastole.

right coronary artery and the epicardial side in the left coronary artery (see Figure 4.14 and 4.15).

5.4 Relationship between Atherosclerosis and WSS in the Coronary Arteries

It is known that a low and oscillatory WSS region favors atherosclerotic plaque localization (Giddens et al. 1983). According to our modeling predictions, the entrance WSS distribution in the right coronary artery will make the myocardial side (the length is about 6 mm or 1.5 times the diameter of the coronary lumen) a preferential site for atherosclerosis. This conclusion corresponds to clinical observations, for example, Fox and Seed (1982) who found that the distribution of plaques is asymmetrical about the circumference of the coronary arteries, such that the atheroma are more concentrated on the myocardial side in the proximal segment of the right coronary artery. The distribution of intimal and medial thickening in the right coronary artery obtained from autopsies observed by Ojha, et al. (2001) (see Figure 2.6) also illustrated that the high frequency of intimal thickening is located on the myocardial side in the proximal RCA. After a few millimeters of length, the flow returns to symmetrical velocity patterns in the distal segments of the coronary arteries.

From Figure 4.15, we can find that the middle section of the LM experiences relatively higher WSS than either the entrance region or the bifurcation. This implies that there is lower probability of atherogenesis midway between the LM ostium and the bifurcation, provided the length of the LM is not unusually short. This suggestion corresponds to the observations by Velican, C. and Velican, D. (1984), in which they

found a “natural resistance” to atherosclerosis that was exhibited beyond about the first centimeter of the right and left coronary arteries by comparison to atherosclerotic involvement distally or near the ostia in these vessels (see Figure 2.7).

On the other hand, if the length of the LM is short, for example, less than 6 mm, the specific entrance flow patterns may reach into the bifurcation and the “natural resistance” segment may vanish. In this case, both low and oscillating WSS regions of the entrance section and the outer curvature sections of the bifurcation will be connected together. This would imply that a short LM coronary artery presents an unusually higher risk factor for atherogenesis. Lewis et al. (2001) noted that a short main left coronary artery was present in a great proportion of patients with complete left bundle-branch block, and Gazetopoulos et al (1987) further confirmed that a short LM may contribute to the promotion of atherosclerosis in the LAD by studying 43 selective coronary arteriography patients.

The WSS distribution in the bifurcation of the left coronary artery in the CFD model shows similar features as those found in the investigations of carotid bifurcations (Ku et al., 1985). Thus, one might expect the flow divider region of the coronary bifurcation to be spared of early atheroma, while the outer curvature sides of the bifurcation, which experience low WSS, would be likely to be regions of predilection for atherosclerosis. Because of curvature, the myocardial side of the bifurcation region of the left coronary artery also exhibits low and oscillating WSS. These areas, namely the lateral-myocardial regions of the bifurcation, would thus be predicted to have higher probability of atherogenesis; and this is in agreement with clinical observations of Svindland, 1983.

5.5 Recommendations and Future Research

The present study has demonstrated the ability of the CFD/MRI technique to model the flow field in the aorta and major branches of the coronary arteries in individual healthy subjects. Comparisons between the computed flow patterns and those obtained *in vivo* with PC-MRI have validated the reliability of the techniques. WSS distributions have been obtained from the computations, and comparison of these with data available in the literature on localization of atherosclerotic plaques in the coronary arteries is consistent with the low mean/oscillating shear stress hypothesis for the role of hemodynamics in atherogenesis.

Future work should consider securing improvements in imaging spatial resolution so that the geometry of the coronary arteries can be defined more precisely. One promising tool is CT scanning. The disadvantage is that CT scans cannot be performed simultaneously with MRI and PC-MRI, and knowledge of the velocity (flow) boundary conditions is essential. However, even separately obtained CT imaging on a subject could prove useful.

The tools developed can be employed to established a better understanding of hemodynamics in normal subjects, so that the variability among individuals can be better appreciated. However, perhaps the most promising avenue for future research is in the study of the etiology of vascular disease. One approach, currently underway, is to model the aorta/coronary artery flow fields in subjects awaiting heart transplants. In these cases, the actual tissue can be recovered following transplantation and used to relate hemodynamics with biological markers of atherosclerosis in an effort to elucidate mechanisms of plaque formation.

REFERENCES

1. Agrawal, Y., Tabot, L. and Gong, K. (1978). Laser-anemometer study of flow development in curved circular pipes, J. Fluid Mech., 85:497-518.

2. Aoki, S., K. Aoki, S. Ohsawa, H. Nakajima, H. Kumagai and T. Araki (1999). Dynamic MR imaging of the carotid wall, J. Magn. Reson. Imaging, 9:420-427.

3. Asakura, T. and Karino, T. (1990). Flow Pattern and Spatial Distribution of Atherosclerotic Lesions in Human Coronary Arteries, Circulation Research, 66 (4): 1045-1066.

4. Bao, X., C. Lu, and J. A. Frangos (1999). Temporal gradient in shear but not steady shear stress induces PDGF-A and MCP-1 expression in endothelial cells: role of NO, NF kappa B, and egr-1, Arterioscler Thromb Vasc. Biol., 19:996-1003.

5. Bogren, G. H. and Buonocore, H. M. (1999). 4D magnetic resonance velocity mapping of blood flow patterns in the aorta in young vs. elderly normal subjects, J. Magnetic Resonance Imaging, 10:861-869.

6. Berger, S. A., Talbot, L. and Yao, L. S. (1983). Flow in curved pipe, Ann. Rev. Fluid Mech., 15: 461-512.

7. Bierman, E. L. (1994). Atherosclerosis and other forms of artherosclerosis, Harrison's Principles of Internal Medicine. 13th ed. New York, NY: McGraw-Hill Book Co. pp. 1106-1116.

8. Bogren, H.G. and Buonocore, M.H. (1999). 4D Magnetic Resonance Velocity Mapping of Blood Flow Patterns in the Aorta in Young vs. Elderly Normal Subjects, Journal of Magnetic Resonance Image, 10:861-869.

9. Caro, C.G., Doorly, D.J., Tarnawski, M., Scott, K.T., Long, Q. and Dumoulin, C.L. (1994). Non-Planar Curvature and Branching of Arteries, J. Physiol., 475:60.

10. Caro, C.G., Doorly, D.J., Tarnawski, M., Scott, K.T., Long, Q. and Dumoulin, C.L., (1996). Non-Planar Curvature and Branching of Arteries and Non-Planar-Type of Flow, Proceedings of the Royal Society of London A. **452**, pp. 185-197.

11. Caro, C.G., J.M. Fitz-Gerald, and R.C. Schroter, (1971). Atherosclerosis and arterial wall shear: observations, correlation and proposal of a shear dependent mass transfer mechanism for atherogenesis, Proc. Roy. Soc. London B, 177:109.

12. Caro, C.G., J.M. Fitz-Gerald, and R.C. Schroter, (1971). Proposal of a shear dependent mass transfer mechanism for atherogenesis, Clin. Sci. 40:5P.

13. Centers for Disease Control and Prevention. (1999). National Center for Health Statistics and National Center for Chronic Disease Prevention and Health Promotion 1999.

14. CFD Research Corporation. CFD-ACE Flow Solver Vesion 6.0. 2001.

15. Chandran, K.B., M.J. Vonesh, A. Roy, S. Greenfield, B. Kane, R. Greene, and D.D. McPherson, (1996). Computation of vascular flow dynamics from intravascular ultrasound images. Med Eng Phys. 18:295-304.

16. Chang, J.L. and Tarbell, M.J. (1985). Numerical simulation of fully developed sinusoidal and pulsatile flow in curved tubes, J. Fluid Mech., 161:175-198.

17. Chopra, P., Sethi, U., Gupta, K.P. and Tandon, D.H., (1983). Coronary arterial stenosis: an autopsy study, Acta. cardiologica. Vol. XXXVIII. pp. 183-197.

18. Clark, C. and Schultz, D., (1973). Velocity distribution in aortic flow, Cardiovasc. Res. 7: 601-613.

19. Cornhill, F.J., herderick, E.E. and Stary, C.H., (1990). Topography of human aortic sudanophilic lesions. Monoger Atheroscler. 15:13-19.

20. Crottum, P., Svindland, A. and Walloe, L. (1983). Localization of atherosclerotic lesions in the bifurcation of the main left coronary artery, Atherosclerosis, 47:55-62.

21. Dean, W.R., (1928). The Streamline Motion of Fluid in a Curved Pipe, Philosophical Magazine, **5**:673-695.

22. DeBakey, M. E. Lawrie, G.M. Glaeser, D.S. Bogren, G.H., (1985). Patterns of atherosclerosis and their surgical significance, Annals of Surgery, 201:115-131.

23. Doby, T. and Lowman, R.M. (1961). Demonstration of blood currents with radiopaque streamers, Acta. Radio, 55:272-275.

24. Fahrig, R., A.J. Fox, S. Lownie, and D.W. Holdsworth. (1997). Use of a C-arm system to generate true three-dimensional computed rotational angiograms: preliminary in vitro and in vivo results, AJNR Am. J. Neuroradiol 18:1507-1514.

25. Farthing, S., and Peronneau, P., (1979). Flow in the thoracic aorta, Cardiovasc Res. 13:607-620.

26. Fayad Z.A., Worthly, S.G., Helft, G., et al. (2001). Magnetic Resonance Imaging of the Vasculature System, Hurst's The Heart, New York, NY: McGraw-Hill, pp. 609-627.

27. Fox, B., James K., Morgan, B. and Seed, A. (1982). Distribution of fatty and fibrous plaques in young human coronary arteries, Atherosclerosis, 41:337-347.

28. Fox, B. and Seed, A.W. (1981). Location of early atheroma in the human coronary arteries, J. Biomechanical Eng., 103:208-212.

29. Fox, R.W. and McDonald, A.T., (1978). Introduction of fluid mechanics, John Wiley & Sons, Inc.

30. Frazin, L.J., Lanza, G., Vonesh, M., Khasho, F., Spitzzeri, C., McGee, S., Mehlmann, D., Chandran, K.B., Talano, J. and McPherson, D., (1990). Functional Chiral Asymmetry in the Descending Thoracic Aorta, Circulation, **82:**1985-1994.

31. Fry, D.L. (1968). Acute vascular endothelial changes associated with increased blood velocity gradients, Circ Res. 22:165-197.

32. Fung, Y.C. (1997). Biomechanics: Circulation, Springer-Verlag, New York Inc. pp. 446-509.

33. Fung, Y.C. (1990). Biomechanics: Motion, Flow, Stress, and Growth, Springer-Verlag. New York Inc.

34. Gazetopoulos, N., Ioannidis, J.P., Marselos, A., kelekis, D., Lolas, C., Avgoustakis, D., and Tountas, C., (1976). Length of main left coronary artery in the relation to atherosclerosis of its branches, British Heart J. 38:180-185.

35. Gibson, C. M., L. Diaz, K. Kandarpa, F.M. Sacks, R.C. Pasternak, T. Sandor, C. Feldman, and P. H. Stone, (1993). Relation of vessel wall shear stress to atherosclerosis progression in human coronary arteries, Arterioscler Thromb*,* 13:310-315.

36. Giddens, D.P., Zarins, C.K., Glagov. S. Bharadraj, B.K. and Ku, D.N. (1983). Flow and atherogenesis in the human carotid bifurcation. Fluid Dynamics as a Localizing Factor for Atherosclerosis, edited by Schettler, G, Spinger-Verlag Press.

37. Hohnhauser, B. and Hommel, G. (2003). 3D pose estimation using coupled Snakes, J. WSCG, Vol. 12, No.1-3, ISSN 1213-6972.

38. Houston, J.G., Belch, J.F.F. and Dick, J.B.C. (2002). Loss of normal aortic and carotid spiral blood flow increases wall hemodynamic slvesses and is associated with carotid atheromatous disease, Circulation, 106 (19), abstract 87.

39. Hundley, W.G., Lange, R.A., Clarke, D.G., Meshack, M.B., Payne, J., Landau, C., McColl, R., Sayad, E.D., Willett, L.D., Willard, E.J., Hillis, D.L. and Peshock, M.R., (1996). Assessment of coronary arterial flow with flow reserve in human with magnetic resonance imaging, Circulation, 93:1502-1508.

40. Hyun, S., C. Kleinstreuer, and J.P. Archie, Jr., (2000). Hemodynamics analyses of arterial expansions with implications to thrombosis and restenosis, Med Eng Phys, 22:13-27.

41. Ilegbusi, O.J., Z. Hu, R. Nesto, S. Waxman, D. Cyganski, J. Kilian, P.H. Stone, and C.L. Feldman, (1999). Determination of Blood Flow and Endothelial Shear Stress in Human Coronary Artery *in vivo*. J. Invasive Cardiol, 11:667-674.

42. Inaba, T., and Murata, S., (1978). Pulsating laminar flow in a sinusoidally curved pipe, Bull JSME. 21:832-839.

43. Irisawa, H., Wilson, M.E., Rushmer, R.F. (1960). Left ventricle as a mixing chamber, Circ. Res., 8:183-187.

44. Kass, M., Witkin, A. and Terzopoulos, D. (1988). Snakes: Active Contour Models, International Journal of Computer Vision, pp. 321-331.

45. Keegan, J., Gatehouse, D.P., Mohiaddin, H.R., Yang, G.Z, and Firmin, N.D., (2004). Comparison of spiral and FLASH phase velocity mapping, with and without breath-holding, for the assessment of left and right coronary artery blood flow velocity, J. Magn. Reson. Imaging, 19:40-49.

46. Kilner, P.J., Yang, G.Z., Mohiaddin, R.H., Firmin, D.N. and Longmore D.B., (1993). Helical and Retrograde Secondary Flow Patterns in the Aortic Arch Studied by Three-Dimensional Magnetic Resonance Velocity Mapping, Circulation, **88:**2235-2247.

47. Kjaernes, M., Svindland, A., Walle, L. and Willoe, S.O., (1981). Location of early artheriosclerotic lesions in arterial bifurcation in humans, Acta. Path. Microbiol. Scans. Sect. A., 89:35-40.

48. Klipstein, R.H., Firmin, D.N., Underwood, S.R., Rees, R.S. and Longmore, D.B., (1987). Blood Flow Patterns in the Human Aorta Studied by Magnetic Resonance, British Heart Journal, **58**(4):316-323.

49. Komai, Y. and Tanishita, K., (1997). Fully developed intermittent flow in a curved tube, J. Fluid Mech., 347:263-287.

50. Krams, R., J.J. Wentzel, J.A. Oomen, R. Vinke, J.C. Schuurbiers, P.J. de Feyter, P. W. Serruys, and C.J. Slager, (1997), Evaluation of endothelial shear stress and 3D geometry as factors determining the development of atherosclerosis and remodeling

in human coronary arteries in vivo. Combining 3D reconstruction from angiography and IVUS (ANGUS) with computational fluid dynamics, Arterioscler Thromb Vasc. Biol., 17:2061-2065.

51. Ku, D.N., D.P. Giddens, C.K. Zarins, and S. Glagov, (1985). Pulsatile flow and atherosclerosis in the human carotid bifurcation. Positive correlation between plaque location and low oscillating shear stress, Arteriosclerosis, 5:293-302.

52. Ladak, H.M., J.B. Thomas, J.R. Mitchell, B.K. Rutt, and D.A. Steinman, (2001). A semiautomatic technique for measurement of arterial wall from black blood MRI, Med. Phys., 28:1098-1107.

53. Langenhove, V.G., Wentzel, J.J., Krams, R., Slager, J.C., Hamburger, N.J. and Serruys, W.P., (2000). Helical velocity patterns in a human coronary artery, Circulation, 102:e22-e24.

54. Lewis, C.M., Dagenais, G.R., Friesinger, G.C., and Ross, R.S., (1970). Coronary arteriographic appearances in patients with left bundle-branch block, Circulation, 41:299.

55. Lind, L., (2003). Circulating markers of inflammation and atherosclerosis, Atherosclerosis, 169:203-214.

56. Liu, H., (2000). Computation of the Vortical Flow in Human Aorta, ASME-BED Advances in Bioengineering, **48:**103-104.

57. Long, Q., X.Y. Xu, M.W. Collins, T.M. Griffith, and M. Bourne, (1998). The combination of magnetic resonance angiography and computational fluid dynamics: a critical review, Crit. Rev. Biomed. Eng., 26:227-274.

58. Lynch P.R, Bove A.A., (1969). Patterns of blood flow through the intact heart and its valves, In; LA Brewer III (ed). Prosthetic Heart Valves. Charles C Thomas, Springfield, DL.

59. Meairs, S., J. Rother, W. Neff, and M. Hennerici, (1995). New and future developments in cerebrovascular ultrasound, magnetic resonance angiography, and related techniques, J. Clin. Ultrasound 23:139-149.

60. Milner, J.S., J.A. Moore, B.K. Rutt, and D. A. (1998). Steinman. Hemodynamics of human carotid artery bifurcations: computational studies with models reconstructed from magnetic resonance imaging of normal subjects, J. Vasc. Surg., 28:143-156.

61. Moor, J., Steinman, D., Ethier, C., (1998). Computational blood flow modelling: Errors associated with reconstructing finite element models from magnetic resonance images, J. Biomechanics, 31:179-184.

62. Murata, S., Miyake, Y., and Inaba, T., (1976). Laminar flow in a curved pipe with varying curvature, J. Fluid Mech., 73:735-752.

63. Nagel, E., Bornstedt, A., Hug, J., Schnackenburg, B., Wellnhofer, E. and Fleck, E., (1999). Noninvasive determination of coronary blood flow velocity with magnetic resonance imaging: comparison of breath-hold and navigator techniques with intravascular ultrasound, Mag. Reson. Med. 41:544-549.

64. Nichols W.W., and O'Rourke M.F., (1998). McDonald's Blood Flow in Arteries, pp.51.

65. Ojha, M., Leask, L. R., Butany, J. and Johnston, W.K., (2001). Distribution of intimal and medial thickening in the human right coronary artery: a study of 17 RCAs, Atherosclerosis, 158:147-153.

66. Patankar, S.V. (1980). Numerical heat transfer and fluid flow, McGraw-Hill, New York.

67. PDAY Research Group, (1993). Natural history of aortic and coronary atherosclerotic lesions in youth, Atheriosclerosis and Thrombosis, 13:1291-1298.

68. Perktold, K., Peter, R. and Resch, M. (1989). Pulsatile non-Newtonian blood flow simulation through a bifurcation with an aneurysm, Biorheology, 26:1011-1030.

69. Piegel, A.L. and Tiller, W., (1997). The NURBS Book, Springer-Verlag, New York, 2nd edn.

70. Rushmore, W.L., and Taulbee, D.B., (1978). Numerical investigation of developing pipe flows of arbitrary curvature, Comp. and Fluid., 6:125-140.

71. Sakuma, H., Kawada, N., Takeda, K. and Higgins, C. B., (1999). MR measurement of coronary artery blood flow, J. Magn. Reson. Imaging, 10:728-733.

72. Schmermund A., Erbel R. (2001). Unstable coronary plaque and its relation to coronary calcium, Circulation, 104:1682-1687.

73. Seed, W., and Wood, N., (1971). Velocity patterns in the aorta, Cardiovasc Res., 5:319-330.

74. Segadal, L., and Matre, K., (1987). Blood Velocity Distribution in the Human Ascending Aorta, Circulation, **77:**90-100.

75. Stary, C.H., (1987). Macrophages, macrophage foam cells, and eccentric intimal thickening in the coronary arteries of young children, Atherosclerosis, 64:91-108.

76. Steffan. H., Brandstatter, W., Bachler, G. et al, (1989). Comparison of Newtonian and non-Newtonian blood flow in stenotic vessels using numerical simulation, Proc. Of #2 International Symposium on Biofluid Mechanics and Biorheology, pp.695-701.

77. Stein. P.D., Sabbah, H.N. and Anbe, D.T., (1979). Comparison of Disturbances of Flow in the Main Pulmonary Artery and Ascending Aorta of Man, Biorheology, 16:357-362.

78. Stonebridge, A.P., Hoskins, R.P., Allan, L.P. and Belch, F.J., (1996). Spiral laminar flow *in vivo*, Clinical Science, 91:17-21.

79. Suo, J., Oshinski, J. and Giddens, D., (2001). Effects of Inflow Conditions and Wall Motion on Flow in the Ascending Aorta, ASME 2001 Summer Bioengineering Conference, pp. 13-14.

80. Suo, J., Oshinski, J. and Giddens, D., (2002). Numerical simulation of Flow Pattern in the Entrance Regions of the Left and Right Coronary Arteries, Second Joint EMBS-BMES Conference 2002, pp. 248.

81. Suo, J., Oshinski, J. and Giddens, D., (2003). Effects of wall Motion and compliance on flow patterns in the ascending aorta, J. Biomech. Eng. 125:347-354.

82. Suo, J., Oshinski, J. and Giddens, D., (2003). Entrance flow patterns in the coronary arteries: a computational study, ASME 2003 Summer Bioengineering Conference, pp. 513.

83. Svindland, A., (1983). The localization of sudanophilic and fibrous plaques in the main left coronary bifurcation, Atherosclerosis, 48:139-145.

84. Svindland, P. G. A. and Walloe, L. (1983). Localization of atherosclerotic lesions in the bifurcation of the main left coronary artery, Atherosclerosis, 47:55-62.

85. Tasciyan, T.A., R. Banerjee, Y.I. Cho, and R. Kim, (1993). Two-dimensional pulsatile hemodynamic analysis in the magnetic resonance angiography interpretation of a stenosed carotid arterial bifurcation, Med. Phys. 20:1059-1070.

86. Thomas J.D., (1990). Flow in the descending aorta: A turn of the screw or sideways glance? Circ., 82:2263-2265.

87. Ting, D.T., (1999). Computational fluid dynamics modeling of blood flow in human root of aorta and left coronary artery, Ph. D. thesis, Johns Hopkins University.

88. Van Doormaal, J.P. and Raithby, G.D., (1984). Enhancements of the SIMPLE method for predicting incompressible fluid flows. Numerical Heat Transfer, 7:147-163.

89. Velican, C. and Velican, D., (1979). Incidence of atherosclerotic lesions in the coronary arteries of adolescents and young adults, Rev. Roum. Med. Med. Int., 17:468.

90. Velican, C. and Velican, D., (1979). Study of fibrous plaques occurring in the coronary arteries of children, Atherosclerosis, 33:201-212.

91. Velican, C. and Velican, D., (1980). Incidence, topography and light-microscopic feature of coronary atherosclerotic plaques in adults 26-35 years old, Atherosclerosis, 35:111-122.

92. Velican, C. and Velican, D., (1984). Natural resistance to atherosclerosis exhibited by the first centimeter of left and right coronary arteries, Atherosclerosis, 50:173-181.

93. Wang, K.C., R.W. Dutton, and C.A. Taylor, (1999). Improving geometric model construction for blood flow modeling, IEEE Eng. Med. Biol., 18:33-39.

94. Woltring, H., (1986). A Fortran package for generalized, cross-validatory spline smoothing and differentiation, Advances Engineering Software 8(2):104-107.

95. Yearwood, T.L. and Chandran, K.B., (1982). Physiological pulsatile flow experiments in model of the human aortic arch, J Biomechanics, 15:683-704.

96. Zabielski, L. and Mestel, A. J., (1998). Steady Flow in a Helically Symmetric pipe, Journal of Fluid Mechanics, **370:**297-320.

97. Zabielski, L. and mestel, J., (1998). Unsteady flow in a helically symmetric pipe, J. Fluid Mech., 370:321-345.

98. Zhao, S.Z., X.Y. Xu, A.D. Hughes, S.A. Thom, A.V. Stanton, B. Ariff, and Q. Long, (2000). Blood flow and vessel mechanics in a physiologically realistic model of a human carotid arterial bifurcation, J.Biomech., 33:975-984.

VITA

Jin Suo was born in Taiyuan, Shanxi Province, China on December 26, 1950. He attended Taiyuan University of Technology in February, 1978 and graduated with the Bachelor of Engineering in January, 1982. He then attended Beijing University of Aeronautics and Astronautics and received the degree of Master of Engineering in Automation Science in October, 1984. He had a position as associate professor in Taiyuan University of Technology before he came to the USA in October, 1997.